ROBUST GENERATOR SYSTEM USING PM ASSISTED SYNCHRONOUS

RELUCTANCE GENERATOR WITH CURRENT-FED DRIVE

A Dissertation

by

JEIHOON BAEK

Submitted to the Office of Graduate Studies of
Texas A&M University
in partial fulfillment of the requirements for the degree of

DOCTOR OF PHILOSOPHY

December 2009

Major Subject: Electrical Engineering

ROBUST GENERATOR SYSTEM USING PM ASSISTED SYNCHRONOUS

RELUCTANCE GENERATOR WITH CURRENT-FED DRIVE

A Dissertation

by

JEIHOON BAEK

Submitted to the Office of Graduate Studies of
Texas A&M University
in partial fulfillment of the requirements for the degree of

DOCTOR OF PHILOSOPHY

Approved by:

Chair of Committee,   Hamid A. Toliyat
Committee Members,   Shankar P. Bhattacharyya
                    Prasad Enjeti
                    Won-Jong Kim
Head of Department,   Costas N. Georghiades

December 2009

Major Subject: Electrical Engineering

ABSTRACT

Robust Generator System Using PM Assisted Synchronous Reluctance Generator

with Current-fed Drive.

(December 2009)

Jeihoon Baek, B.S.; M.S., Hongik University;

M.S., University of Wisconsin-Madison

Chair of Advisory Committee: Dr. Hamid A. Toliyat

The growth of embedded generation and portable electrical installations has led to an increased demand for low cost, flexible and reliable generator systems for military and commercial applications. An interior permanent magnet (IPM) machine has high power density due to its reluctance torque and magnetic torque components so it can produce a large constant power-speed range. However, an IPM machine needs demagnetizing current at high-speed during the flux-weakening region and thus develops an inverter shutdown problem in an uncontrolled generator mode operation. In order to overcome the disadvantages of the IPM machine, the permanent magnet assisted synchronous reluctance generator (PMa-SynRG) can be a good solution for low cost, high efficiency reliable generator systems. A PMa-SynRG can produce a high efficiency drive by utilizing the proper amount of magnet and reluctance torque. This work proposes a PMa-SynRG with two flux barriers and permanent magnets embedded in the second layer of the rotor. A neodymium magnet (NdFeB) was used as permanent

magnets in the rotor to prevent demagnetization. Finding the minimum amount of magnet is one of the goals of the optimization process.

The objectives of this work are to build an optimal design for the 3kW generator and an advanced power electronics converter for the PMa-SynRG drive system. In order to find the optimized 3kW machine, a Lumped Parameter Model (LPM) was used to achieve fast computation, and Differential Evolution Strategy (DES) was used to embed the LPM in an efficient numerical optimization routine to identify optimum designs. Finite Element Analysis (FEA) was used for test performance of optimum designs. On the basis of differences between LPM and FEA, model predictions were used to fine tune the LPM model. For new optimum design converges, numerical optimizations and iterations were performed to produce LPM and FEA predictions.

For the drive system, the thyristor based, current-fed drive is much simpler and has lower power losses compared to the pulse width modulation (PWM) drive. Eliminating the requirement for self-controlled switches is a distinct advantage for lower cost. Another feature of the developed current-fed drive is its inherent capability to provide generating action by making the PMa-SynRG operates as a generator, rectifying the phase voltages by means of the three-phase rectifier and feeding the power into the load. These features make the current-fed drive a good candidate for driving any type of synchronous generators including the proposed PMa-SynRG.

DEDICATION

To my parents

ACKNOWLEDGEMENTS

TABLE OF CONTENTS

LIST OF FIGURES

LIST OF TABLES

CHAPTER I

INTRODUCTION

1.1. Overview

This dissertation investigates a robust and low cost generator system using a Permanent Magnet assisted Synchronous Reluctance Generator (PMa-SynRG) and control system using a current-fed drive with a direct power control (DPC) algorithm.

Chapter I reviews the introduction of the PMa-SynRG and thyristor based current fed drive. The objective of the proposed research is described and the specific objectives are discussed.

Chapter II provides formulations of equivalent circuit modeling of PMa-SynRG based on the Lumped Parameter Model (LPM); the generator operating capability includes loss calculation.

Chapter III introduces machine design parameters in order to satisfy generator specifications and the optimal design process. The Differential Evolution Strategy (DES) and the iteration method by Finite Element Analysis (FEA) were developed for maximizing efficiency and minimizing machine cost. In this study, two different winding configurations were compared to achieve a wide constant power speed range (CPSR) and high efficiency. Test performance of optimum designs using FEA and the differences between LPM and FEA model predictions were used to fine tune the LPM model.

_____

This dissertation follows the style of *IEEE Transactions on Industry Applications*.

Chapter IV discusses the machine fabrication process and characteristics of the 3kW PMa-SynRG. To verify the design parameters, experimental and simulation results are compared.

Chapter V introduces the new control topology by current fed drive for the 3kW generator system. The proposed drive topology of the current-fed drive system has advantages such as a low switching loss, robust and low cost. The various advantages and disadvantages of the proposed current-fed drive and the voltage-fed pulse width modulation drive are summarized.

Chapter VI suggests a voltage based direct power control (V-DPC) strategy for the PMa-SynRG system because it has a lower sampling frequency. V-DPC has simple and noise-resistant power estimation algorithm which makes it easy to implement in a Digital Signal Processor (DSP). Other advantages of V-DPC are good dynamic response and no current regulation loop.

Chapter VII summarizes the key observations from all chapters and discusses potential future directions.

1.2.   Permanent Magnet Assisted Synchronous Generator

Electric generators can be classified by principles. The classification by principle includes commercial and military types together with new configurations still in the laboratory stages. By principle, there are three main types of electric generators: (a) synchronous generators (b) induction generators and (c) parametric with magnetic anisotropy and permanent magnets.

Synchronous generators generally have a stator made of silicon steel laminations with a multiphase winding and a rotor. It is usually the rotor design that leads to a variety of synchronous generator configuration. Those that are DC excited require a power electronics excitation control, while those with permanent magnets (PMs) or variable reluctance rotors have to use full power electronics in the stator to operate at variable speeds. However, electrically excited synchronous generators maybe provided with power electronics converters in the stator when they work in stand alone applications or in power grids with DC high voltage capable transmission lines.

For powers in the MW/unit range and less, induction generators were used specially for wind power applications. They are: (a) single-phase cage induction generator, (b) dual stator windings with different number of poles and cage rotor, (c) doubly-fed or wound field rotor. Pulse-width modulation (PWM) converters are connected to the stator for the single-phase stator winding and also to the auxiliary stator winding for the dual stator windings configurations. Because the PWM converter supplies the auxiliary winding its rating is notably lower than that of the full power of the main winding and it is proportional to the speed variation range.

Parametric generators rely on the variable reluctance principle, but may also use PMs to enhance the power and volume and to reduce generator losses. There are a number of configurations that suit this category such as the switched reluctance generator, the transverse flux PM generator, and the flux reversal generator. In general, the principle on which they are based relies on co-energy variation due to magnetic

anisotropy (with or without PMs in the rotor or on the stator), in the absence of a pure traveling field with constant speed like synchronous or induction generators.

The requirement for the development of inexpensive, flexible and reliable generator systems has expanded in the last few years, due to growth in the use of portable electrical installations. The prime mover based on the needed power level may vary form high speed gas turbine equipment to low speed wind turbines or to internal combustion engines.

It is accepted that power electronic conversion to match the generator output to the load requirement is going to be essential and with a wide range of potential input shaft speeds no existing generator topology is going to be appropriate for all applications. The need has arisen specially for military applications for the development of a simple, rugged generator system which can produce power effectively across the range of shaft speeds. The generator should produce a flexible yet controllable electrical output for potential utilization with many variations in load.

Current and proposed generators include systems based mainly on DC machine, synchronous and AC induction machine technologies as well as reluctance machines. While extracting more energy from the prime mover, most proposed variable-speed systems suffer a cost disadvantage due to the required power electronic converter. This cost penalty may eventually render the additional energy capture meaningless. Thus, reducing the cost of the power electronic hardware is essential for variable-speed generating systems to achieve viable and competitive $/kWh ratios.

Synchronous generators are characterized by a uniformly slotted stator laminated core that hold a multiphase alternating current winding and a DC excited or PM excited or variable saliency rotor. The two traveling fields of the stator and rotor at relative standstill interact to produce a smooth torque. The shaft speed is rigidly tied to stator frequency, because the rotor produced magnetic field is DC, typically hetropolar in synchronous generators. These generators are built with both salient and non salient poles rotors. For lower speed synchronous generators with a large number of poles, the rotors are made of salient rotor poles provided with concentrated DC excitation coils. However, for higher speed applications such as in turbogenerators round rotors are used. The rotor pole shoes maybe made of laminations, in order to reduce additional rotor losses, but the rotor pole bodies and core are made of mild magnetic solid steel.

A wide constant power-speed range (CPSR), high efficiency and high reliability are required in auxiliary generator systems for commercial and military applications. An interior permanent magnet (IPM) machine derives high power density from magnetic torque and reluctance torque components and can provide a large constant power speed operation [1]-[4]. However, IPM needs demagnetizing current in the flux-weakening region and it also has an inverter shutdown problem under the uncontrolled generator mode of operation [5]-[6]. In order to overcome the disadvantages of IPM machines, the Permanent Magnet assisted Synchronous Reluctance Machine (PMa-SynRM) is a good candidate due its low cost, high efficiency and reliability [7].

Adding the proper quantity of permanent magnets into the synchronous reluctance generator (SynRG) rotor core is another way to improve the operating

performance of this machine. In this case, the motor is similar to an IPM machine. However, the amount of permanent magnets used and the permanent magnet flux-linkages are smaller with respect to the conventional IPM. Thus, the proposed generator can be called a Permanent Magnet assisted Synchronous Reluctance Generator (PMa-SynRG). The PMa-SynRG has a multilayer flux barrier and permanent magnet rotor synchronous machine. The rotor core is built of conventional transverse laminations with stamped multiple flux barriers per pole filled with permanent magnet layers. The high magnetic saliency created by the multiple flux barriers in the rotor make reluctance torque predominant at low speeds when higher torque is required [8]-[10].

In this research, the PMa-SynRG was developed with two flux barriers and permanent magnets embedded in the second layer of the rotor. NdFeB permanent magnets were selected to prevent unwanted demagnetization of the magnets. One of the goals of the optimization process was to find a minimum amount of magnet to be used in the rotor. The rotor structure of IPM and PMa-SynRG is shown in Fig. 1. In the IPM machine, permanent magnets were placed in the d-axis. Otherwise, it is considered a q-axis in the PMa-SynRG. In the proposed generator, the high magnetic saliency created by the multiple flux barriers in the rotor make reluctance torque dominant at low speeds when higher torque is required. In order to achieve a wide constant-power and a high power-factor operation in synchronous reluctance machine drives, a large saliency ratio is required. However, achieving such a design using lumped models of a motor is very difficult.

(a) IPM Machine,   (b) PMa-SynRM
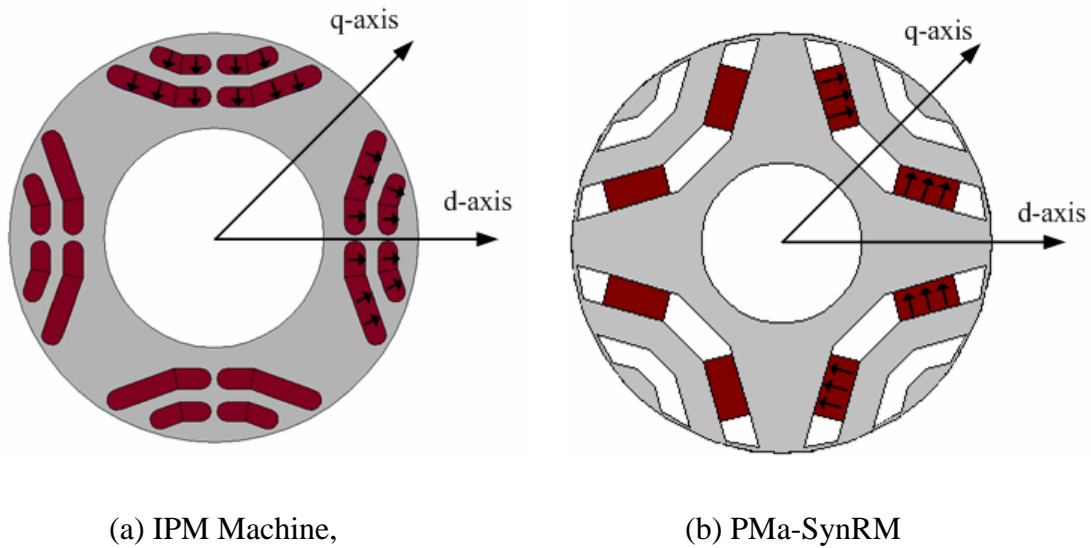
Fig. 1   d q-axis model for IPM and PMa-SynRM.

A large saliency ratio can be achieved by both axially and transversally laminated rotor structures. An axially laminated rotor can present a high-anisotropy and provide a very high unsaturated saliency ratio. However, from the mechanical stress point of view, this rotor has some drawbacks with respect to the transversally laminated one. The effective saliency ratio of transversally laminated rotors can be enhanced by proper placement, proper shape and the proper number of flux barriers [11]. To optimize the motor design, a reasonably good magnetic design can be obtained without using numerical techniques. However, the finite-element method must be used to consider the nonlinear magnetic behaviors of the materials which play a key role whenever overload performance prediction is essential.

One of the main objectives of this study was to optimize the design of PMa-SynRG by performing a set of finite element analyses on a transversally laminated

synchronous reluctance machine. In this procedure, different rotor parameters and their relative effects on the motor performance in terms of output torque and saliency ratio were studied. Moreover, improvement of generator performance due to the permanent magnets placed in the rotor core was investigated by studying their effect on developed torque and the d- and q-axes inductances [12]. The dimension of permanent magnets used in the motor was limited by the cost and flux barrier shapes.

In this study, the size of the generators for output power was determined to be 3kW. Also, the number of poles, stator slots, armature and field windings turns, stator and rotor outer diameters, stator and rotor inner diameters, machine length, and the rotor geometry were specified [13]. Special attention was given to the power density for portable applications and also proper use of permanent magnets on the rotor. The proper dimension of permanent magnets can increase the power density. However, it is crucial to use the permanent magnet properly and at the right location on the rotor for good overall efficiency over a wide speed range. It is important to mention that the so-called permanent magnet brushless DC motor/generator suffer from a low efficiency over a wide speed range although efficiency at a particular speed might be high [14]-[15]. However, the proposed PMa-SynRG, because of its rotor structure that resembles a synchronous reluctance machine, has high efficiency over a wide speed range.

1.3.   Thyristor Based Current-fed Drive

Current and proposed generators include systems based mainly on DC machine, synchronous and ac induction machine technologies as well as reluctance machines.

While extracting more energy from the prime mover, most proposed variable-speed systems suffer a cost disadvantage due to the required power electronic converter. This cost penalty may eventually render the additional energy capture meaningless. Thus, reducing the cost of the power electronic hardware is essential for variable-speed generating systems to achieve viable and competitive $/kWh ratios.

The thyristor based, current-fed drives are traditionally used in very high power applications such as pump and compressor drives, gas-turbine start-ups, and fan drives [16]. A typical schematic of such a drive is shown in Fig. 2.
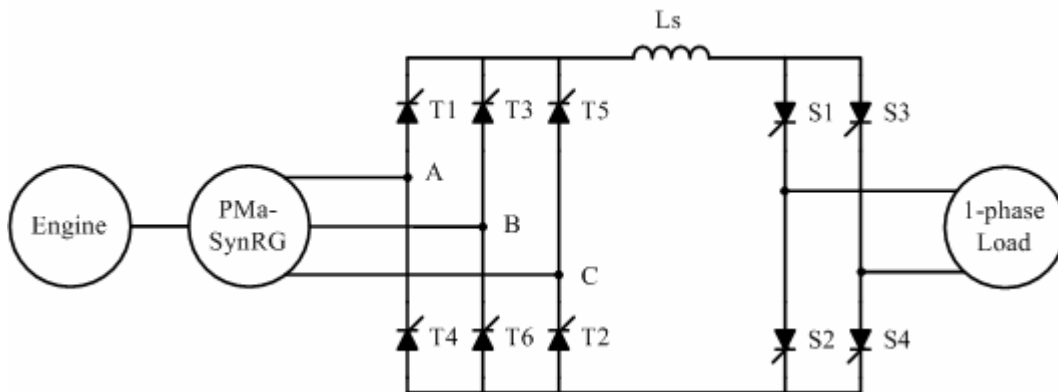
Fig. 2 Current-fed thyristor-based load commutated inverter.

The current-fed drive uses a three-phase controlled rectifier at the input and a current source inverter at the output with a large DC link inductor [17]-[18]. The conventional voltage-fed drive uses a large DC link capacitor to provide a steady DC link voltage. The DC link capacitor supplies the circulating current and hence the input supply current is of a pulsating nature and has a lot of high frequency components,

leading to poor displacement factor and distortion factor. Therefore, the overall power factor of the system is very poor [19]. On the other hand, the current-fed drive eliminates the need for such an expensive capacitor by replacing it with a DC link inductor. The current source topology at the input stage of the proposed drive insures that the machine currents are always within the normal limits of operation even under short circuit conditions. This eliminates the need for any current sensor and short circuit protection circuit. The only function of the inverter in the proposed topology is to distribute the DC link current through the appropriate phase, while the input controlled rectifier controls the amplitude of the current. This leads to a very simple inverter without any hard switching and hence no switching losses [20]-[21]. More advantages of the current-fed drives are:

1. Whenever regenerative braking is required, the output three-phase converter acts as a rectifier while the input single-phase converter acts in an inversion mode. During this mode of operation, rotational energy trapped in motor shaft inertia is transferred back to the input supply. The amount of energy transferred is controlled by changing the delay angle of the input rectifier. This feature is very desirable for some home appliance drives such as washing machines and handheld tools. Otherwise, this regenerated energy is dumped into a resistive element, reducing system efficiency and increasing cost as the power rating of the resistor used needs to be very high.

2. No external commutation circuits are used. Even during the start up when back-EMF is small, the commutation is achieved by controlling the input rectifier.

This makes the proposed converter topology less expensive, more compact to design and more reliable.

3. Usually specially designed electrolytic capacitors with very low series inductance are used to increase life expectancy. In the case of the VSI drive, the capacitor supplies the circulating current and hence the input supply current is of a pulsating nature, leading to a very poor power factor and large frequency current harmonics. The proposed drive, on the other hand, eliminates the need for such an expensive capacitor by replacing it with a DC link inductor.

4. The current source topology at the input stage of the proposed drive insures that the motor currents are always within the normal limits of operation even under short circuit conditions. This eliminates the need for any current sensor and a short circuit protection circuit.

5. Thyristors, on the other hand, make the proposed drive more reliable. The built-in current protection, lack of any commutation circuits and replacement of the DC link capacitor with a highly reliable inductor further extend the reliability of the proposed drive.

6. All the switches used in the input rectifier and the output three-phase inverter are line commutated. The input alternating current is responsible for commutation of the rectifier thyristors while the leading motor phase current commutates the inverter thyristors. The lower switching frequencies lead to very low switching losses as compared to a conventional PWM drive. Thermal losses are low,

increasing system efficiency and reducing overall system cost as the heat sink requirement is low.

7.   A high power factor is a much desired feature for appliance drives where the input current is limited to 15 A at a household outlet. A higher power factor means better utilization of the available current for the same voltage. The proposed system offers a high power factor as compared to a conventional drive, especially at higher loads.

However, current-fed drives have disadvantages such as:

1.   The only controlled circuit in the proposed drive system is the input rectifier. The firing angle of the input rectifier can only be changed as fast as twice the frequency of input voltage. The dynamic response of the proposed drive is slow, making it unsuitable for servo applications.

2.   Although the DC link inductor is more reliable than the electrolytic capacitor and less expensive, it can be bigger both in volume and weight.

3.   Various self-starting schemes can be used to start the motor but the commutation process can fail at lower speeds. Therefore, the proposed system has a limited low frequency operation capability.

Table 1 summarizes the various advantages and disadvantages of the proposed current-fed drive and the voltage-fed back-to-back PWM drive [22]-[24].

Table 1   Advantages and disadvantages of inverters.

	Current-fed Drive	Voltage-fed back-to-back PWM Drive
Advantages	Four-quadrant operation No external commutation circuit No DC link capacitor Built-in current protection High reliability Low switching loss High input power factor	Four-quadrant operation Fast system response Compact system volume, weight Line voltage sag compensation Programmable line power factor
Disadvantages	Slow system response Big system volume and weight Limited at low frequency	Low reliability High switching loss Low input power factor

1.4.   Research Objectives

The purpose of this research is to develop a PMa-SynRG and drive system for portable power applications. In order to design a robust, simple and low cost PMa-SynRG, the optimal design process is suggested using Lumped Parameter Model (LPM), Differential Evolution Strategy (DES) and Finite Element Analysis (FEA). Moreover, this high power density and rugged generator drive will be supplied by a thyristor-based converter for added reliability and cost effectiveness. Therefore, the purpose of this research is two-fold.

The first task is to develop the optimal design process for a low cost and high efficiency 3kW PMa-SynRG. The LPM program provides a fast means for analyzing electromagnetic characteristics and the DES is applied to find the most promising design. The iteration method between the optimized design from the DES and FEA is suggested to find the low cogging torque and low torque ripple.

The second task is to show the experimental performance by using a thyristor based, current-fed drive for portable generator applications. The thyristor based, current-fed drive is much simpler and has lower losses compared to voltage-fed pulse width modulation (PWM) drives. Eliminating the requirement for self-controlled switches is a distinct advantage for lower cost.

Another feature of the developed current-fed drive is direct power control to provide generator power control action by the three-phase rectifier control angle. Generator power can be controlled by the maximum power per voltage function block while the input power command is decided by means of measuring the DC link voltage. These features make the current-fed drive using direct power control a good candidate for driving any type of synchronous generators including the proposed PMa-SynRG.

Another area of concern is to protect the PMa-SynRG from a short circuit fault. An induction machine is self protected and the brush DC motor can always be demagnetized. However, in the case of permanent magnet machines, the high inrush current from the short circuit may permanently demagnetize the machine and may even cause a fire. Therefore, it is necessary to take sufficient measures to prevent this mode of operation. In the proposed generator system, a novel current source converter is used where the current is inherently regulated by the DC link inductor. Therefore, the proposed drive is inherently protected against a short circuit. If the converter terminals are shorted the current through the machine phases will be at the most the rated current.

CHAPTER II

LUMPED PARAMETER MODEL FOR A PERMANENT MAGNET ASSISTED

SYNCHRONOUS RELUCTANCE GENERATOR

2.1. Lumped Parameter Model of PMa-SynRG

This research presents an analytical model using equivalent magnetic circuits for the PMa-SynRG. The lumped parameter model (LPM) is developed from machine geometry, stator winding and machine operating specifications. In the LPM, magnetic saturation of rotor bridges is incorporated into the model and provides an effective means of predicting machine performance for a given machine geometry [25]. The LPM is not as accurate as finite element analysis but the equivalent magnetic circuits provide a fast means to analyze the electromagnetic characteristics of PMa-SynRG. The main goal is to develop an initial and optimum design. The LPM with an efficient numerical optimization routine is used to identify optimum designs. The linear LPM and the nonlinear LPM are programmed using MATLAB so all the machine parameters are calculated very quickly. The design of stator core dimensions and stator winding parameters are well established and the stator of PMa-SynRG is the same as other types of machines. The rotor structure of PMa-SynRG has significant electromagnetic saliency because of cavities in the rotor and it can be modeled using a d, q-reference frame. In this section, simple linear LPM analysis is developed for q-axis magnetizing inductance and PM flux linkage. Otherwise, nonlinear LPM analysis is applied to the d-axis inductance. Fig. 3 depicts the flow chart of the LPM analysis.
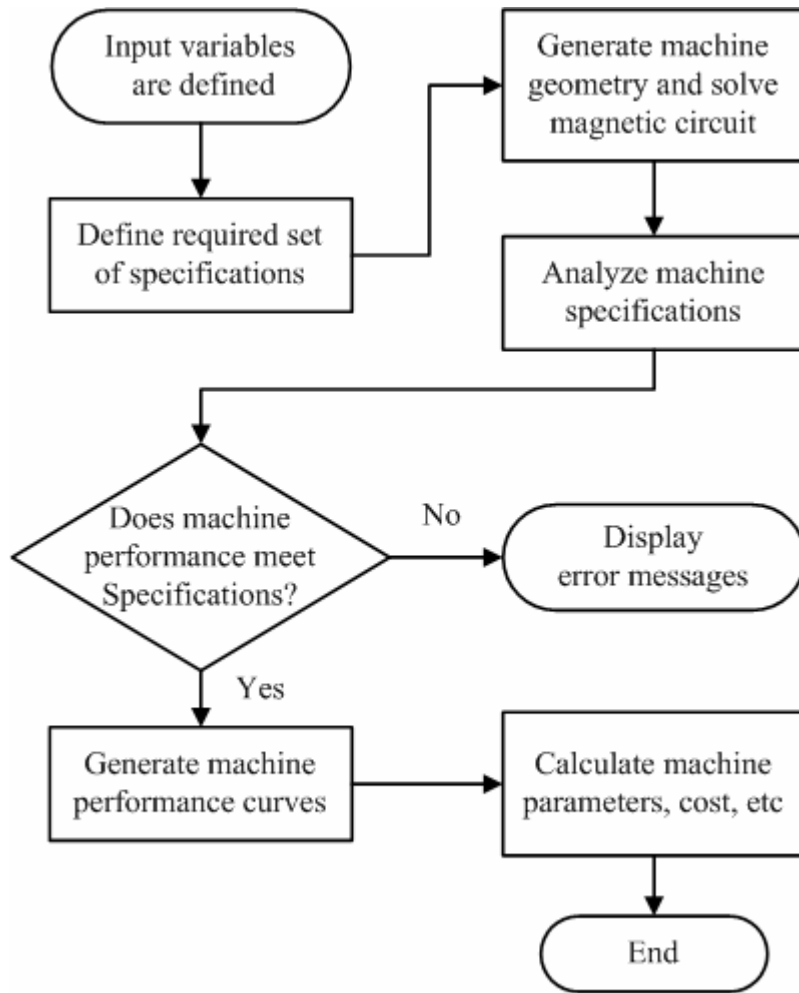
Fig. 3 Lumped Parameter Model analysis flow-chart.

2.1.1. Linear LPM for q-axis Inductances

For the q-axis magnetizing inductance calculation, the round rotor synchronous inductance L_s is replaced by q-axis and d-axis synchronous inductances, L_q and L_d. The q-axis synchronous inductance can be separated into magnetizing and leakage inductance as

$$L_q = L_{qm} + L_l \tag{2.1}$$

The stator winding produces flux leakages and harmonics of magneto motive force (MMF) wave. The slot leakage, end-turn leakage and zig-zag leakage are components of flux leakage; zig-zag leakage inductance is developed when the stator winding is not concentrated in a single slot. Another leakage inductance component of harmonics of the MMF is belt inductance and the fifth and seventh harmonics are dominant as leakage inductance. Therefore, total leakage L_l is

$$L_l = L_{slot} + L_{end} + L_{zig} + L_{zag} + L_{5belt} + L_{7belt} \tag{2.2}$$

Fig. 4 shows the magnetic circuit for the PMa-SynRG with two layers. In the figure, the angle α is defined as the angular distance of the rotor surface between the magnet flux-path. Therefore, $\Delta\alpha_k$ is defined as (k: number of layer)

$$\Delta\alpha_k = \alpha_k + \alpha_{k-1} \tag{2.3}$$
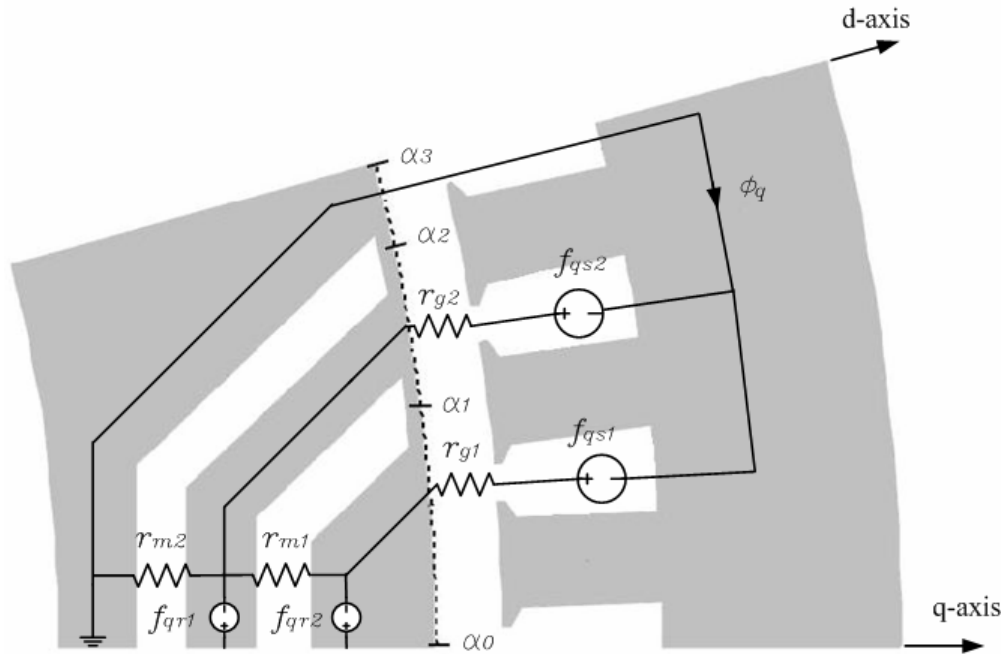
Fig. 4   Equivalent q-axis inductance circuit.

Per unit reluctances for air-gap and cavities can be calculated by the cross-sectional areas and average length. The stator MMF source for the k_{th} segment is expressed by applying Fourier analysis.

$$f_{qsk} = \frac{(\cos(\alpha_{k-1}) - \cos(\alpha_k))}{\Delta \alpha_k} \tag{2.4}$$

The per unit reluctances for the k_{th} rotor cavity and airgap segment are

$$r_{mk} = \frac{2d_{mk} A_s}{g A_{mk}} \qquad r_{gk} = \frac{\Delta \alpha_s}{\Delta \alpha_k} \tag{2.5}$$

where g is airgap, A_s and A_{mk} are cross-sectional area for the stator tooth pitch, magnet. The rotor surface MMF potential for k_{th} layer is

$$f_{qrk} = [(1/r)_{kj}]^{-1} [f_{qsj} / r_{gj}]_{j=1 \, to \, k} \tag{2.6}$$

with the elements of the per unit reluctance given by

$$(1/r)_{kj} = \begin{cases} -\dfrac{1}{r_{mk-1}} & j = k-1 \\[2mm] \dfrac{1}{r_{gk}} + \dfrac{1}{r_{mk-1}} + \dfrac{1}{r_{mk}} & j = k \\[2mm] -\dfrac{1}{r_{mk}} & j = k+1 \end{cases} \tag{2.7}$$

The q-axis magnetizing inductance L_{qm} is a combination of the through component L_{qt} and circulating component L_{qc}.

$$L_{qm} = L_{qt} + L_{qc} \tag{2.8}$$

L_{qt} and L_{qc} can be estimated by magnetic circuit analysis based on fully-saturated bridges and fixed magnet remanence in the rotor and constant magnetic potentials in the stator core. The q-axis through and circulating inductance components are calculated using the following ratios:

$$\frac{L_{qt}}{L_{dm}} = \frac{4}{\pi} \sum_k f_{qsk}(f_{qsk} - f_{qrk}) \cdot \Delta\alpha_k \tag{2.9}$$

$$\frac{L_{qc}}{L_{dm}} = 1 - \frac{4}{\pi} \sum_k \Delta\alpha_k f_{qsk}^2 \tag{2.10}$$

Finally, d-axis magnetizing inductance can be calculated as

$$\begin{aligned} L_{qm} &= \left(\frac{L_{qt}}{L_{dm}} - \frac{L_{qc}}{L_{dm}} \right) \cdot L_{dm} \\ &= \left(1 - \frac{4}{\pi} \sum_k f_{qsk} \cdot f_{qrk} \cdot \Delta\alpha_k \right) \cdot L_{dm} \end{aligned} \tag{2.11}$$

2.1.2. Linear LPM for q-axis PM Flux Linkage

The PM flux linkage can be calculated using a linear magnetic circuit analysis similar to the q-axis inductance calculation. Figs. 5 and 6 depict the cross-section of PMa-SynRG and the magnetic circuit when the permanent magnet is placed in the first and second layers.
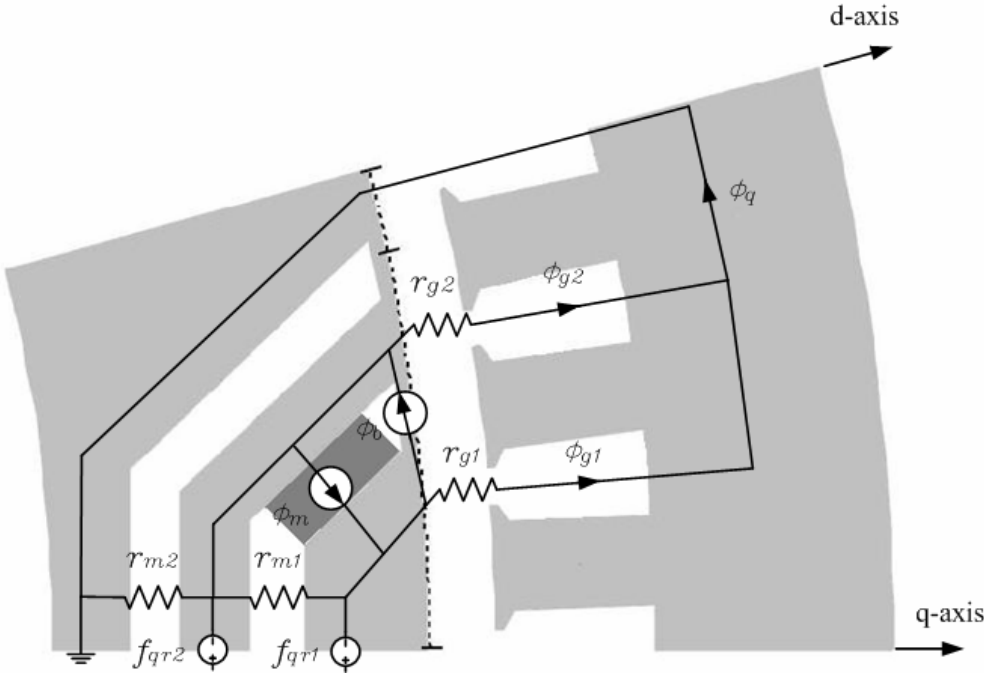
Fig. 5   Equivalent q-axis circuit with the first layer PM.
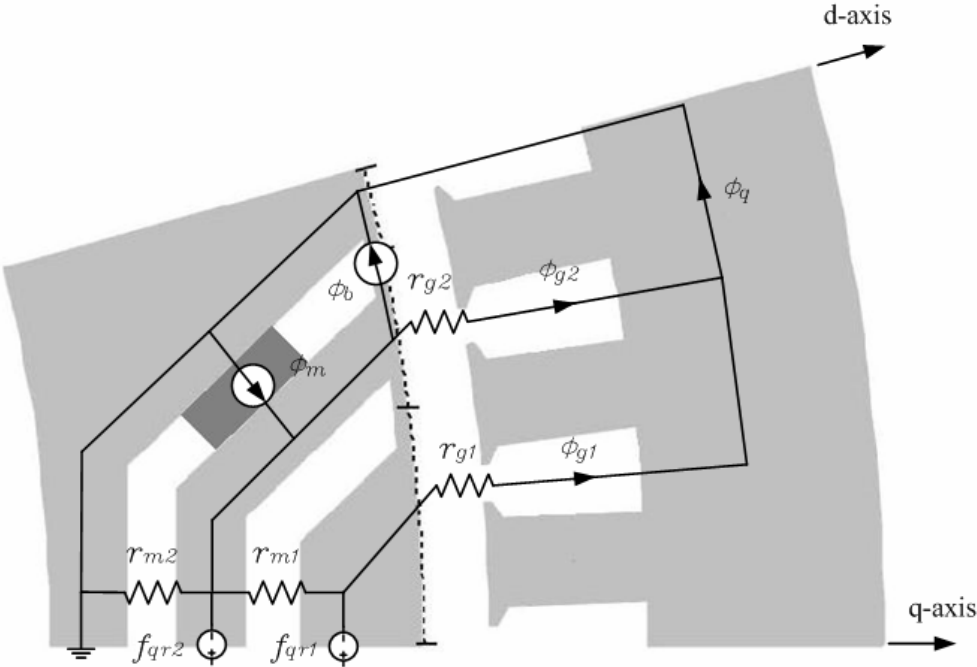
Fig. 6   Equivalent q-axis circuit with the second layer PM.

Permanent magnets are located in the first layer; the PM flux is oriented along the q-axis and the per-unit PM flux source added in the first layer instead of the stator MMF source. Otherwise, the estimated saturation flux source is in the opposite direction to the magnetic circuit. In the same way, the PM flux and the saturation flux sources are located in the second layer when the PM is in the second layer. With the same assumptions of q-axis inductance calculation, the flux density can be calculated as

$$B_{gk} = \frac{1}{A_s}[(1/r)_{kj}]^{-1}\left[\frac{B_r A_{mj}}{2} - B_s A_{bj}\right]_{j=1\,to\,k} \tag{2.12}$$

In this equation, B_{g1} is zero when permanent magnets are located in the first layer and B_{g2} is zero in the second layer. From the winding parameters and flux density calculations, the PM flux linkage can be calculated as

$$\lambda_{PM} = \frac{\sqrt{2}Rl B_{gk} N_a k_a}{p} \tag{2.13}$$

2.1.3. Nonlinear LPM for d-axis Inductances

In the linear LPM, the q-axis is modeled with constant saturation because cavity layers make a flux barrier and prevent saturation along the q-axis core. Otherwise, at the d-axis excitation, the rotor core is saturated by the concentrated flux flowing along the narrow area where sections are separated by the cavity layers. The nonlinear LPM for the saturable d-axis reluctances is based on the core material characteristics. In the nonlinear LPM, the saturable core magnetic characteristic is modeled by curve fit to the

M19 B-H data. The permeability of the core can be found at a particular point from the B-H curve as

$$\mu = \frac{B}{H} \tag{2.14}$$

The nonlinear LPM for the d-axis presents an accurate calculation for the d-axis inductance. The nonlinear equivalent circuit for the d-axis is shown in Fig. 7. The saturable reluctance for each cross-section of stator and rotor core can be calculated by average length, area and flux density (k = number of segments) [26].

$$r_k = \frac{l_k}{\mu B_k A_k} \tag{2.15}$$
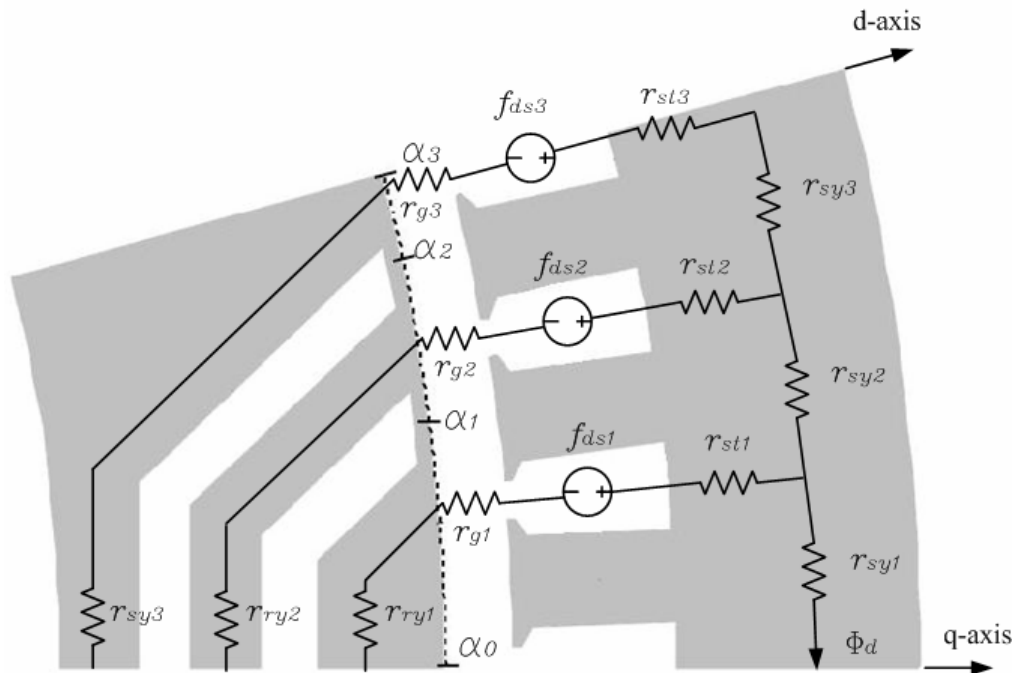
Fig. 7   Nonlinear d-axis equivalent magnetic circuit.

In this circuit, the reluctance of the stator core is separated into the teeth and the back iron because the magnetic flux flows through the teeth to the back iron. Otherwise, the air-gap reluctance of the k_{th} area is

$$r_{gk} = \frac{g}{\mu_0(\alpha_k - \alpha_{k-1})rl} \tag{2.16}$$

The stator MMF source for the k_{th} segment is [27]

$$f_{dsk} = \frac{1}{\alpha_k - \alpha_{k-1}} \int_{\alpha_{k-1}}^{\alpha_k} (f_{ds} \sin \alpha) d\alpha \tag{2.17}$$

From the given excitation, the saturable d-axis flux linkage and inductance are

$$\lambda_{ds} = N_a k_{a1} \Phi_d \tag{2.18}$$

$$L_{dm} = \lambda_{ds} / I_d \tag{2.19}$$

The total d-axis inductance is

$$L_d = L_{dm} + L_l \tag{2.20}$$

Finally, by the q-axis and d-axis inductance calculations, the saliency ratio of the PMa-SynRG is defined as

$$S_r = L_d / L_q \tag{2.21}$$

2.2. Equivalent Circuit Modeling of PMa-SynRG

In this section, the electrical performance characteristics of a PM assisted synchronous machine are analyzed in the d q synchronously rotating reference frame [28]. The most powerful means of analyzing PM synchronous machine uses current, voltage

and back-EMF phasors in a synchronously rotating reference frame locked to the rotor.

Fig. 8 shows d q-frame equivalent circuit for the equivalent circuit.

(a) d-axis equivalent circuit   (b) q-axis equivalent circuit
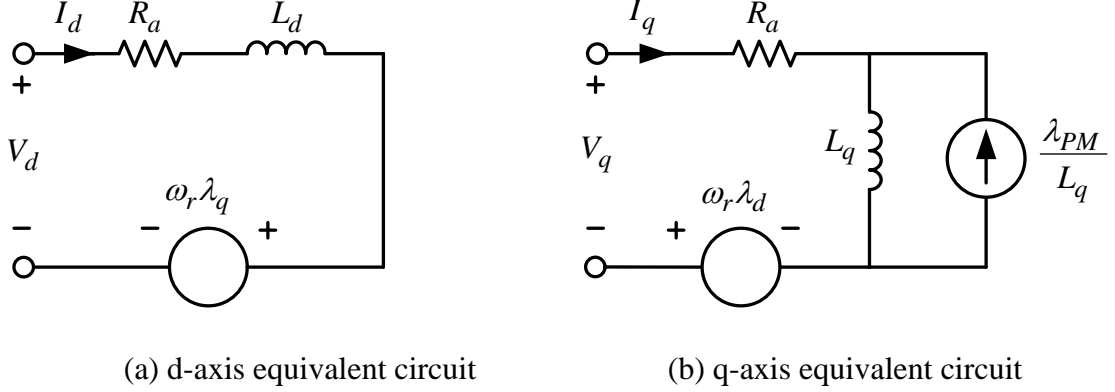
Fig. 8   PMa-SynRG d q-frame equivalent circuit.

The d- and q-axis flux linkages are

$$\lambda_d = L_d \cdot I_d \qquad \lambda_q = L_q \cdot I_q - \lambda_{PM} \qquad (2.22)$$

and terminal voltage equations are,

$$V_d = R_a I_d + L_d \frac{dI_d}{dt} + \omega_r (L_q I_q - \lambda_{PM}) \qquad (2.23)$$

$$V_q = R_a I_q + L_q \frac{dI_q}{dt} - \omega_r L_d I_d \qquad (2.24)$$

and the back-EMF is

$$E_a = p\omega_r \lambda_{PM} \qquad (2.25)$$

where p is the number of pole pairs, ω_r is the rotor angular frequency in electrical

radians per second and λ_{PM} is the permanent magnet flux linkage.

2.2.1. The Steady State d and q-axis Equations

In Fig. 9, the q-axis is aligned with the PM flux linkage phasor $\vec{\lambda}_{PM}$ so that the d-axis is aligned with the back-EMF phasor $\vec{E}$. The torque angle δ is defined from V_a to E_a and the power factor angle ϕ is defined from I_a to V_a [29]-[30].

(a) Phasor diagram for motoring   (b) Phasor diagram for generating
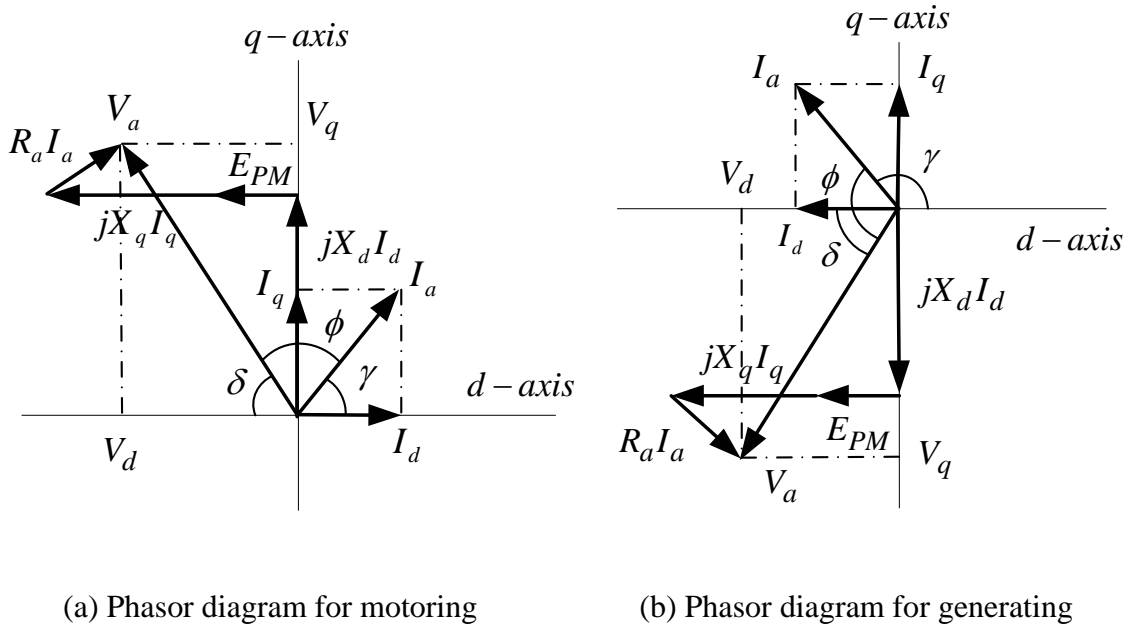
Fig. 9 Phasor diagrams during motoring and generating.

In the phasor diagram operation, the AC terminal voltage is

$$\vec{V}_a = R_a \vec{I}_a + jX_d \vec{I}_d + jX_q \vec{I}_q + \vec{E}_a \tag{2.26}$$

The current control angle,

$$\gamma = \tan^{-1}\left(\frac{I_q}{I_d}\right) \tag{2.27}$$

and the stator current vectors can be represented as,

$$I_d = I_a \cos \gamma \qquad\qquad I_q = I_a \sin \gamma \qquad\qquad (2.28)$$

The steady state d- and q-axis reference terminal voltage components are

$$V_d = -\omega_r(L_q \cdot I_q - \lambda_{PM}) \qquad V_q = \omega_r(L_d \cdot I_d) \qquad (2.29)$$

The general form of the electromagnetic torque in the d q-frame is given by

$$
\begin{aligned}
T_e &= \frac{3}{2}\frac{p}{2}(\lambda_d \cdot I_q - \lambda_q \cdot I_d) \\
&= \frac{3}{2}\frac{p}{2}\left(\lambda_{PM} \cdot I_d + (L_d - L_q) \cdot I_d I_q\right)
\end{aligned}
\qquad (2.30)
$$

In the torque equation, the first component is magnetic torque and the second component is reluctance torque.

2.2.2. Machine Losses Calculations

For the electrical loss calculation in the design of PMa-SynRG, three machine losses are considered: armature losses, core losses and slot harmonic losses. However, mechanical losses such as windage and friction are ignored in this research. The armature losses are given as

$$P_a = 3I_a{}^2 R_a \qquad (2.31)$$

where I_a is the RMS phase current and R_a is the phase resistance. The phase resistance is calculated from the winding configurations and stator dimensions as

$$R_a = \frac{l_a}{\sigma_a A_a} \qquad (2.32)$$

where l_a is the total machine length include end turns, A_a is the conductor cross-sectional area and σ_a is conductivity of the winding.

The core loss has hysteresis and eddy-current loss component [31]. The eddy current core loss of stator teeth and yoke are defined as

$$P_{et} = \frac{12}{\pi} q k_e \omega_s^{\,2} B_t^{\,2} \tag{2.33}$$

$$P_{ey} = \frac{1}{\alpha} \frac{8}{\pi^2} k_e \omega_s^{\,2} B_b^{\,2} \tag{2.34}$$

and hysteresis core loss of stator teeth and yoke are

$$P_{ht} = k_h \omega_s^{\,2} B_t^{\,n} \tag{2.35}$$

$$P_{hy} = k_h \omega_s^{\,2} B_b^{\,n} \tag{2.36}$$

Therefore, the total core loss is

$$P_c = (P_{et} + P_{ht}) \cdot V_t + (P_{ey} + P_{hy}) \cdot V_y \tag{2.37}$$

where V_t is the total volume of teeth and V_y is the total volume of yoke.

Finally, the slot harmonic loss is considered here because the air-gap flux harmonics produced by the stator open slot result in rotor surface eddy currents. A slot harmonic loss model includes the rotor lamination effect such as

$$\delta_i = \sqrt{\frac{1}{\pi f_i \sigma \mu}} \tag{2.38}$$

$$\lambda_i = \frac{d}{\delta_i} \tag{2.39}$$

where f_i is the slot harmonic frequency, σ is the core surface conductivity and d is the lamination thickness. Therefore, the slot harmonic loss can be express as

$$F_{sk} = \frac{3}{\lambda_i} \cdot \frac{\sinh(\lambda_i) - \sin(\lambda_i)}{\cosh(\lambda_i) - \cos(\lambda_i)} \tag{2.40}$$

$$P_h = \frac{\sigma \pi^2 d^2}{6} \cdot f_i^2 B_h^2 F_{sk} \tag{2.41}$$

where B_h is the slot harmonic flux density.

2.2.3. Generator Operating Capability

For the generating operation, P_{elec} is negative and the power balance model is

$$P_{elec} = P_{shaft} + P_a + P_c + P_h \tag{2.42}$$

where P_{shaft} is the power transferred from the shaft. The mechanical converted power P_{mech} is defined as

$$P_{mech} = T_e \omega \tag{2.43}$$

and the electric power is

$$P_{elec} = 3V_a I_a \cos\phi \tag{2.44}$$

where V_a is the RMS phase voltage and $\cos\phi$ is the power factor. In the generating operation, the generator efficiency is

$$\eta_g = \frac{P_{elec}}{P_{shaft}} = 1 - \frac{P_a + P_c + P_h}{P_{shaft}} \tag{2.45}$$

For generating, P_c and P_h are not negligible when the generator operates at high speed. The generator power capability at a constant speed is an iterative solution because there is no closed-form solution such as maximizing output torque to simultaneously minimize the efficiency of the motoring operation [32]-[33]. Therefore, the generating operation requires searching current space for maximizing the rear power and minimizung the required torque input.

CHAPTER III

OPTIMAL DESIGN PROCESS USING DIFFERENTIAL EVOLUTION

STRATEGY AND FINITE ELEMENT ANALYSIS

3.1. Optimal Design Using LPM and Differential Evolution Strategy

This section summarizes the development of the machine design process based on the LPM with Differential Evolution Strategy (DES). Fig. 10 describes the basic optimization flow-chart. In the flowchart, the LPM provides a fast means for analyzing the electromagnetic characteristics of the PMa-SynRG. It is not as accurate as finite element analysis, but much faster. LPM provides an effective means for predicting machine performance for a given machine geometry.
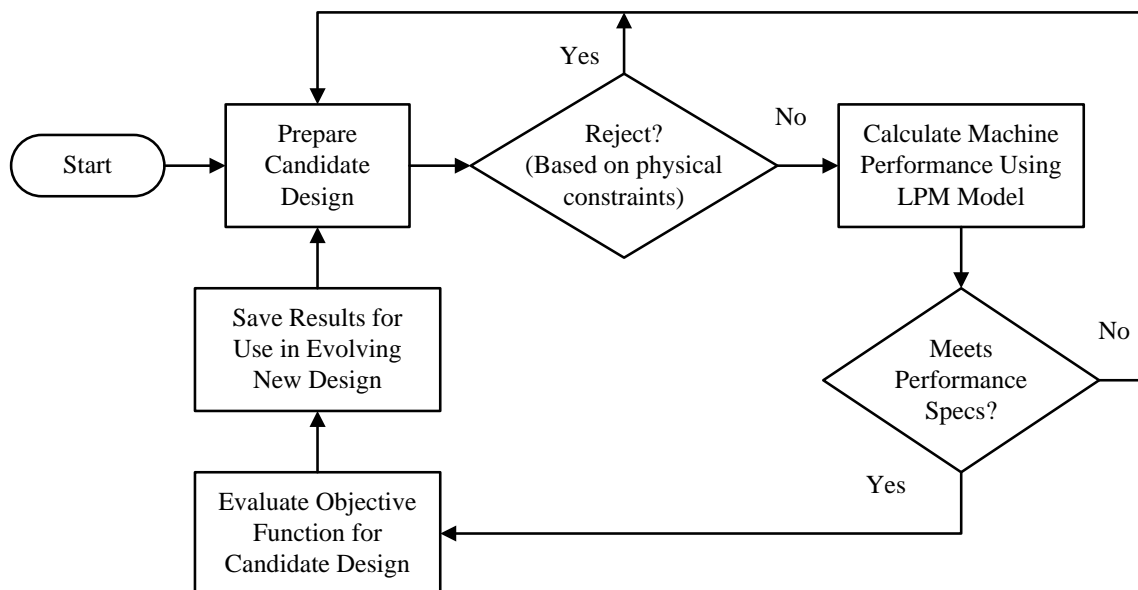
Fig. 10 Basic optimization flow-chart.

Each candidate design will be evaluated at specified generator operating points with reasonable geometry limits. The LPM will be used to determine whether the candidate design can deliver the required performance within variable limits. The adopted approach uses a lumped parameter magnetic circuit model representing the electromagnetic behavior of the machine with equivalent circuits. The LPM is created by approximately partitioning the geometry and excitation under a specific set of assumptions. A differential evolution genetic algorithm is used to explore the multi-dimensional variable design space in order to identify the most promising designs to meet performance criteria that include efficiency, power factor and cost [34]. Required power and optimal control angle must be found for the specific operating point. Each candidate design that meets all requirements for delivering sufficient required power, etc., is then evaluated for "goodness" using an objective function. An objective function can be configured using a variety of quantitative evaluation criteria such as PM flux linkage, efficiency, or power factor. Weighting coefficients can be added to adjust the importance of multiple criteria in the penalty function. For this design exercise, predicted generator cost and stator current were used as the basis for the penalty function. A differential evolution program was used to explore large multi-dimensional design space to find the best design [35].

The optimization program will be configured to find the design that minimizes machine materials cost while also keeping the efficiency and power factor as high as possible. Also, the weighting coefficients (k_1, k_2) can be added to adjust the importance of multiple criteria in the penalty function [36]. For the first generation, predicted

generator cost and stator current were used as the basis for the objective function, expressed as

$$Objective\ \ Function = \sqrt{k_1 \cdot I_a{}^2 + k_2 \cdot cost(gen)^2} \qquad (3.1)$$

3.1.1. Generator Specifications

Table 2 provides a summary of the stated specifications for electrical limits, key machine dimensions and machine materials.

Table 2   Specified machine parameters.

Parameters	Specifications
Speed [rpm]	3,600
Maximum Output Power [W]	3,000 max
Stator Outer Diameter [mm]	190 max
Active Length Including Housing [mm]	127 max
Maximum Stack Length [mm]	70 max
Maximum Rotor Inner Diameter [mm]	25.4 max
Air-gap [mm]	0.7 min
Maximum Current Density [A/mm^2]	15
Stator winding insulation	Class H $(180\,^\circ C)$
Peak Mechanical Stress of Rotor [MPa]	470
Core Lamination Material	M19
Permanent Magnet Material	Sintered NdFeB

The lamination steel material specified for the stator and the rotor core is M19, reflecting a desire to minimize machine cost. The sintered NdFeB magnet material selected for this machine has a residual flux density B_r value of 1.3T. However, the magnet properties were adjusted for an operating temperature in the vicinity of 130 $^\circ C$

when developing the machine design; the stator winding temperature was assumed to be

180 $^\circ C$ when calculating machine losses and efficiency.

3.1.2. Machine Design Parameters

The stator tooth and slot geometric parameters are shown in Fig. 11. The tooth pitch is decided by the slots/pole/phase and it is used to decide the series turns per phase with stator geometric parameters. The stator winding can determine the distributed or concentrated winding and will be performed in the optimal design process.
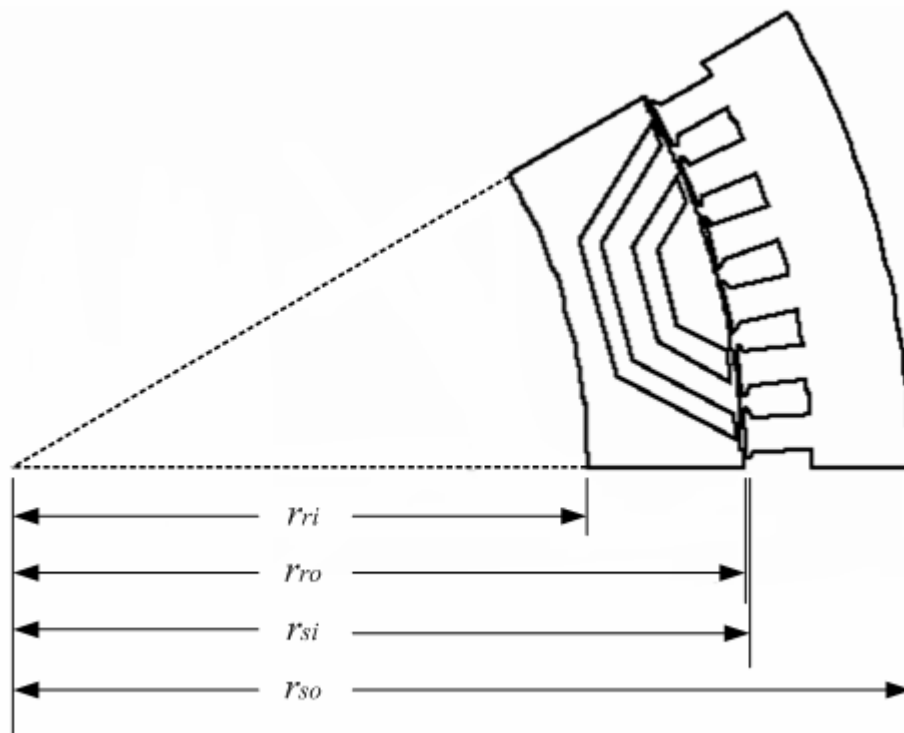
Fig. 11   Stator one slot pitch design parameters.

$r_{ri},\ r_{ro}$: inner and outer diameter of the rotor core

$r_{si},\ r_{so}$: inner and outer diameter of the stator core

In the optimal design of PMa-SynRG, the outer stator diameter is fixed. The inner rotor diameter and the outer rotor diameter depend on the ratio considering the outer diameter of the shaft. The pole pitch is decided by the number of poles.

Table 3 summarizes the design parameters for the optimal design process in LPM and DES. The first variable to the fifth variable are the design parameters for the stator. The stator stack length and the winding numbers per slot per phase decide machine output characteristics. The back iron depth, slot height and width are design parameters in LPM for the slot fill factor and torque pulsation by the stator shape design,. These five variables are optimized in DES by the iteration between the minimum and maximum values.

Table 3   Design parameters for optimal design process.

Design parameter in LPM	Minimum for DES	Maximum for DES	Converged by DES
Axial stack length [mm]	50	80	65
Num of winding per slot per phase	5	40	24
Stator back iron depth [mm]	5	20	8.34
Ratio of slot height to slot width	0.5	2.5	2.1044
Ratio of slot to slot + tooth width	0.4	0.6	0.4402
rri/rro	0.5	0.8	0.659
(dm1+dm2)/(rro-rri)	0.2	0.5	0.3772
dm1/(dm1+dm2)	0.3	0.5	0.4651
dr1/(dr1+dr2+dr3)	0.15	0.4	0.3958
dr2/(dr1+dr2+dr3)	0.2	0.4	0.3094
Span ratio of the second layer	0.6	0.9	0.7388

The shape of rotor cavities depends on many geometric parameters. Fig. 12 shows the cross-section of the rotor and design variables of the cavity and the width of rotor core.
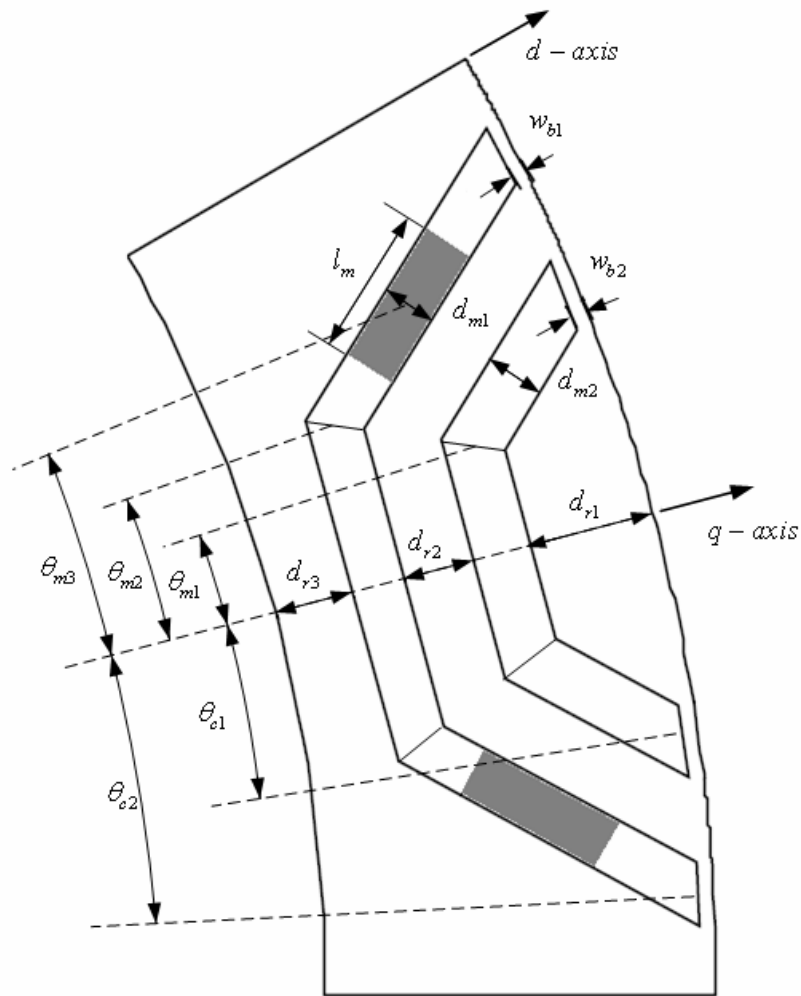
Fig. 12   Rotor design parameters.

$d_{m1,}\ d_{m2}$: thickness of the first and second layer in the rotor

l_m : permanent magnet length

$d_{r1,}\ d_{r2,}\ d_{r3}$: thickness of the first, second and third bridge in the rotor

The bridge thickness w_b and width of the cavity d_m should consider for the saturation effects. The generator output characteristics are affected by the shape of the cavity and are determined by the angular spans and radius of the center point.

In order to minimize the rotor core and permanent magnets volume using the objective function, six variables for the rotor core are used in the LPM. The inner diameter of the rotor core is decided by the ratio of the outer diameter to the inner diameter rri/rro. The permanent magnet thickness and the bridge thickness are decided by the ratio between the two variables of magnet thickness and the three variables of bridge thickness. Finally, the span ratio of the second layer is optimized by the DES to minimize torque pulsation and cogging torque.

In the optimal design process, two different types of rotor structure are evaluated. The first type of rotor structure shows that permanent magnets are inserted in the first layer and the other is in the second layer. For the high efficiency and power factor, the first type of design is worse than the second type because it uses only a small portion of the magnetic torque. Therefore, the first type needs more current and creates a bigger power loss. In order to minimize the phase current and the amount of permanent magnet, the optimization process will be performed based on the second type of design.

3.1.3. Stator Winding Configurations

The adoption of concentrated windings for the PMa-SynRG makes it possible to significantly reduce the volume of copper used in the coil end windings compared to conventional distributed windings. In addition, the shorter end windings provide opportunities to reduce the winding copper losses, improving machine efficiency when compared to its counterpart with distributed windings [37]. The concentrated winding structure provides opportunities for simplifying the manufacturing process for the stator,

including minimizing the number of stator coils. Key parameters associated with the two

windings are summarized in Table 4.

Table 4   Key Parameters for distributed and concentrated windings.

Parameter	slot/pole/phase	number of slots	number of poles	slots short pitched
Distributed	1	12	4	1
Concentrated	0.5	12	8	0

Fig. 13 shows examples of a 4-pole PMa-SynRG with distributed windings on the left and an 8-pole PMa-SynRG with concentrated windings on the right. In this particular comparison, the distributed winding has 1 slots/pole/phase, while the concentrated winding has a slot/pole/phase value of 0.5. The span of the stator coils is 150 electrical degrees for the distributed winding (i.e., 1 slot short-pitched) and 120 electrical degrees for the concentrated winding configuration [38].
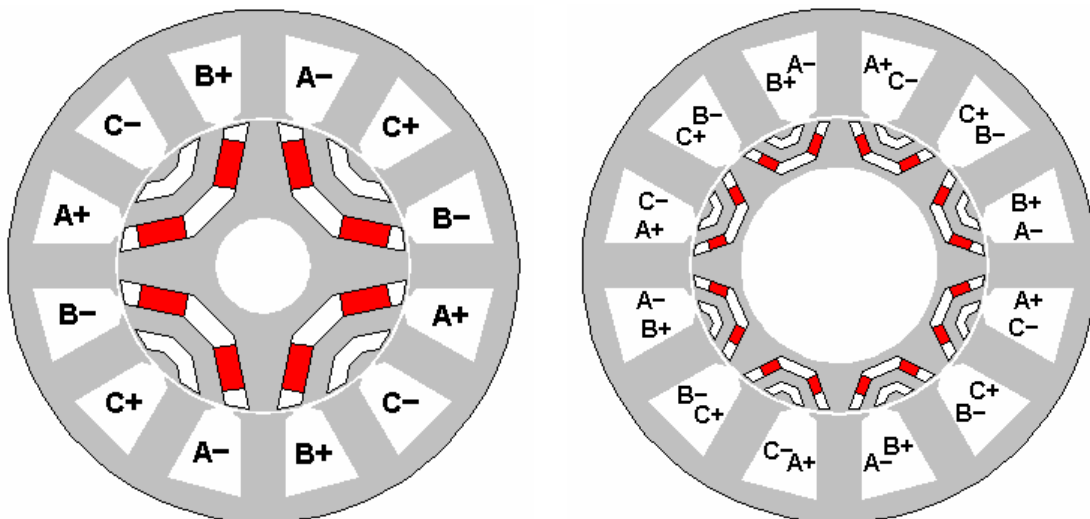
Fig. 13   PMa-SynRG with distributed and concentrated windings.

The combinations of slots and poles that allow the realization of a balanced winding can be determined by the number of slots-per-pole-phase, S_{pp}, defined as

$$S_{pp} = \frac{S}{2p \cdot m} \tag{3.2}$$

where S is the number of stator slots, p is the number of pole pairs and m is the number of phases. Three-phase machines with concentrated windings have S_{pp} values less than or equal to 0.5 [39]. The magnet flux linkage of concentrated and distributed winding can be calculated using the winding function technique summarized in the following equations.

$$\lambda_{a\_con} = r_g l_{eff} \cdot \frac{4}{p} K_{w1} N_1 B_{max} \tag{3.3}$$

$$\lambda_{a\_dis} = r_g l_{eff} \cdot 2 N_2 B_{max} \tag{3.4}$$

where λ_a is the magnet flux linkage of phase A [in Wb], r_g is the airgap radius [in m] and l_{eff} is active length of the machine [in m]. K_{w1} is the fundamental component winding factor that has a value of 0.866 for $S_{pp} = 0.5$ [40].

From equation (3.3) and (3.4), the relationship between the number of turns per coil needed in the two different windings to insure equality of the total magnet flux linkage can be determined to be

$$N_1 = 2.31 \cdot N_2 \tag{3.5}$$

The d-axis inductance values for the two different windings can be calculated as follows:

$$L_{d\_con} = L_{self} + L_{mutual} = \frac{\mu_0 r_g l_{eff} N_1^2}{g} \cdot \frac{\pi}{3} \tag{3.6}$$

$$L_{d\_dis} = L_{self} + L_{mutual} = \frac{\mu_0 r_g l_{eff} N_2{}^2}{g} \cdot \frac{2\pi}{3} \tag{3.7}$$

The ratio of the d-axis inductances for the two different windings under the constraint of the same magnet flux linkage can be evaluated by the combining equation (3.6) and (3.7)

$$\frac{L_{d\_con}}{L_{d\_dis}} = \frac{N_1{}^2}{2N_2{}^2} = 2.67 \tag{3.8}$$

This result shows that the value of L_d for the concentrated-winding machine is higher than for the corresponding L_d value for the distributed-winding machine. This higher value of L_d with concentrated windings makes it easier to reduce the value of the characteristic current to meet the conditions for optimal flux weakening in comparison to the distributed-winding machine [41].

3.1.4. Optimized Design Results by the DES

In this section, design parameters and optimized results by DES are compared for each stator winding configuration. By the optimal design process, the number of stator slots per pole for the distributed winding converged from 72/12 to 12/4. Fig. 14 depicts the initial and optimized machine dimensions.

The rated phase current decreases from 29.89A to 15.17A and reduces the total loss of the machine. Using the objective function in the DES, the phase current is minimized to maximize the machine efficiency and the total magnet mass is minimized to reduce machine cost. In the results, the optimized design parameters show much better performance than the initial design.
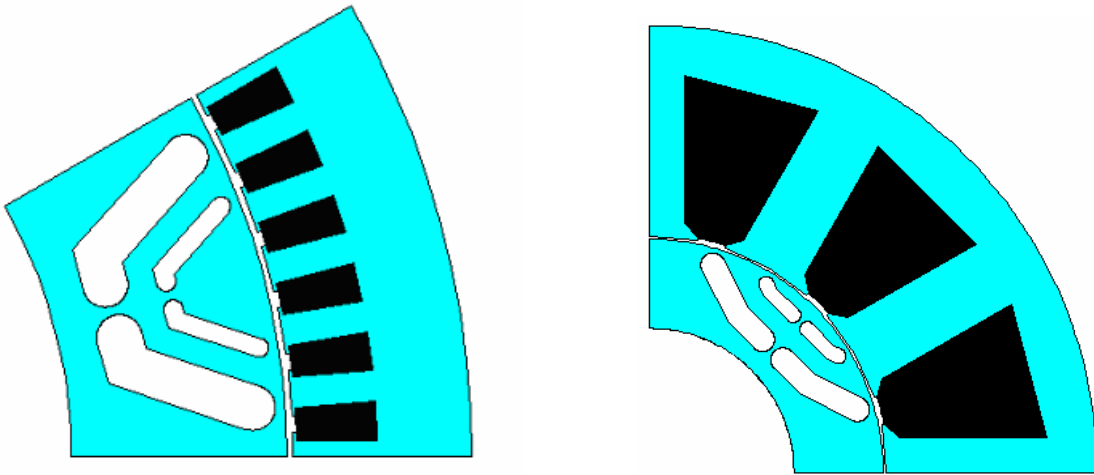
Fig. 14   Initial and optimized design with distributed windings.

The initial and optimized designs with concentrated machine are shown in Fig. 15 and the number of stator slots per poles are 6/4 and 12/8 each.
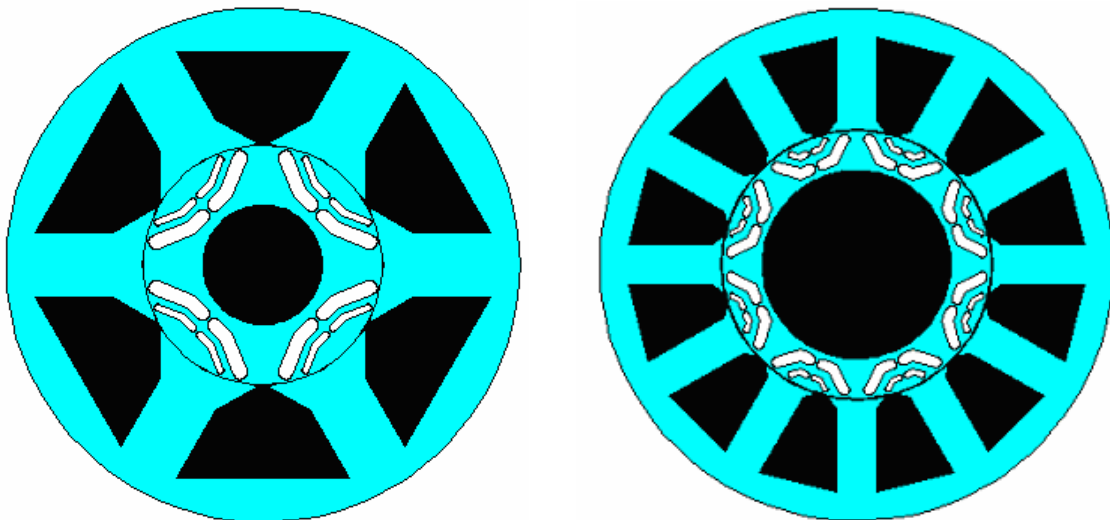
Fig. 15   Initial and optimized design with concentrated windings.

The stator current of the first generation optimized design is improved from 23.6A to 18.5A and it is effective in reducing the price of the switching devices. As the stator current decreases, the total loss of the first generation optimized design is reduced even though the number of series turns of the stator is increased. Moreover, the important design parameter in generator design is power factor which is improved from 0.77 to 0.98 by optimizing the current angle. Table 5 summarizes the optimized machine parameters for each winding configuration using the optimal design process after 10,000 iterations.

Table 5   Optimized machine parameters for distributed and concentrated windings.

Stator Winding	Distributed		Concentrated	
Design	Initial	Optimized	Initial	Optimized
Number of Slots/poles	72/12	12/4	6/4	12/8
SPP	2	1	0.5	0.5
Series Turns per Slot	24	100	60	88
Rated Stator Current [Arms]	28.89	15.17	23.6	18.5
Axial Length [mm]	70	75	70	75
PM flux linkage [mWrms]	14.9	83.77	30	55
Total Magnet Mass [Kg]	1.3	0.887	0.535	0.595
Total Loss [W]	180.1	105.92	106.7	96.6
Efficiency [%]	94.2	96.3	96.6	96.8
Power Factor	0.99	1	0.77	0.98

Using differential evolution strategy, the stator current of each design converged at 15A and the armature loss of concentrated winding machine is reduced to 43%. Moreover, the active length of the machine and the total magnet mass are decreased to 17% and 40%, respectively. Therefore, the concentrated winding machine is optimized with lower cost and better output characteristics than the conventional distributed winding machine.

3.2 Optimal Design Process Using Iteration between LPM and Finite Element Analysis

Two-dimensional finite element analysis software is used for a fundamental accuracy check of the LPMs that are developed and applied to the candidate machine. Test performance of optimum designs using FEA and the differences between LPM and FEA model predictions fine tune the LPM model. The numerical optimization and iteration were relaunched until LPM and FEA predictions for new optimum design converged [42]-[43]. Fig. 16 shows the flow chart of the optimal design process using LPM and FEA.
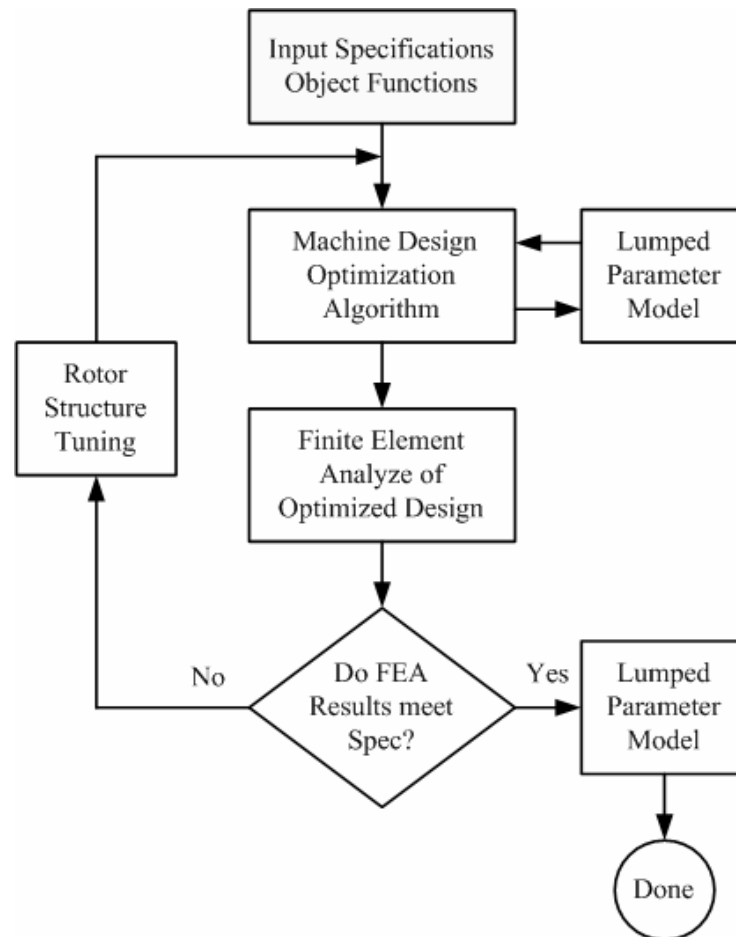
Fig. 16   Flow-chart of iteration between the optimized LPM and FEA.

The output torque is obtained using direct computation of force on the stator from the Lorenz force on the conductors and magnet's torque calculation derived from virtual work on the rotor. Test performance of the optimum designs is conducted using FEA and the difference between LPM and FEA model predictions to fine tune the LPM. The numerical optimization and iteration were relaunched until LPM and FEA predictions for new optimum design converged [44]-[45]. Convergence typically requires two or three iterations.

3.2.1. Final Optimized Model by the FEA

Based on the optimized model using LPM and DES, the final optimized model is designed through several iterations and fine tuning between LPM and FEA. In the final optimized model, the rated power increased to 3,300W in order to provide a 10% margin for the actual machine operation performance. Also, the unity power factor and the maximum efficiency with the minimum amount of permanent magnet are the objective functions during the optimization process. With these conditions, the center bridges are removed and machine output performance is improved. Fig. 17 shows the cross section of the final optimized model. In the d q-current plane, the operation point can be found by the intersection between the voltage limit ellipse and constant power hyperbola in the generating quadrant. From the operating point, the d, q-axis currents and current angle are decided for the control of the generator.
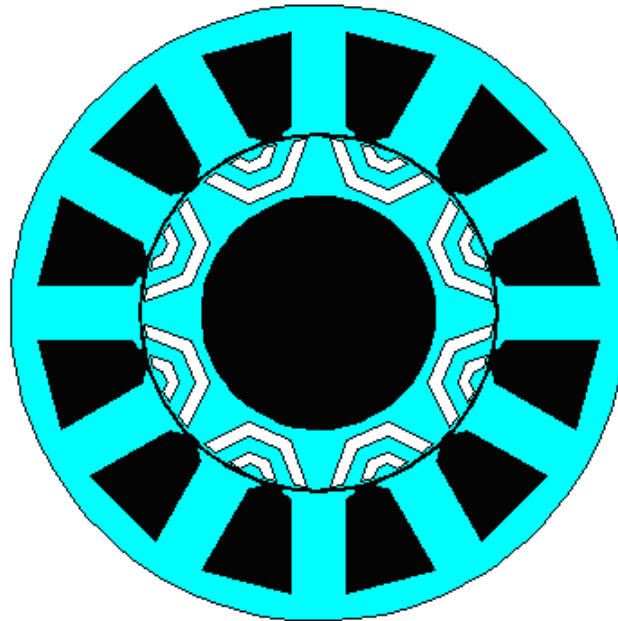
Fig. 17   Cross section of the final optimized model.

For analysis of the optimized model and comparison between the optimized model by DES and the final optimized models, the two-dimensional FEA is used. The LPM model is limited to analyze the cogging torque and output torque ripple. Therefore, FEA needs to analyze the distributions of the output characteristics in a transient condition. Fig. 18 shows the distribution of flux line and Fig. 19 describes the distribution of flux density to show saturation. When the distribution of the flux density is compared to the optimized model by DES, the final optimized model has a smaller saturation area and the level of flux density at the bridges is lower. Also, leakage flux lines in the first layer are reduced by increasing the thickness of the first layer. Therefore, the machine performance of the final optimized model is much better than the optimized model by DES in terms of leakage and saturation effects.
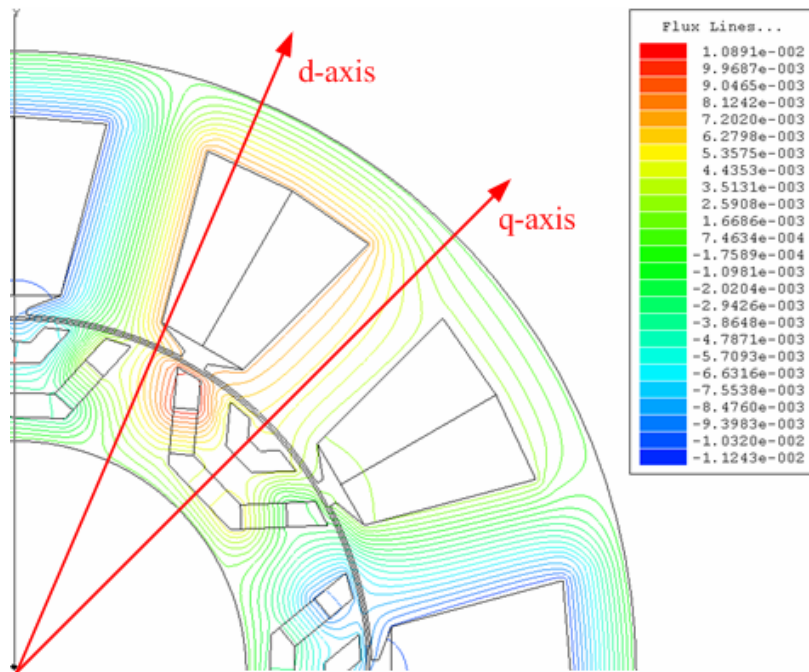
Fig. 18   Flux lines distribution from FEA.
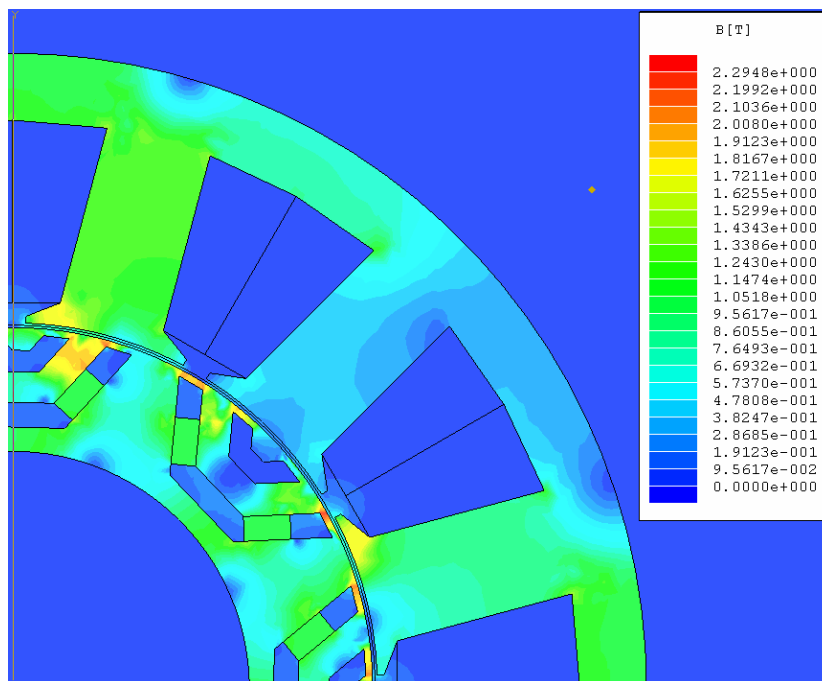
Fig. 19   Flux density distribution from FEA.

3.2.2.   Comparisons between the Optimized Model by DES and Final Optimized Model

In this chapter, comparisons between the optimized model by DES and final optimized models are performed based on the LPM and FEA. The final optimized model is optimized by fine tuning between LPM and FEA and Table 6 to summarize the machine parameters and output performances. The final optimized model is designed based on the same stator winding and the number of slots per pole. The rated current is converged to 15A and it decreased 19% compared to the optimized model by DES. Also, the active length of machine and total magnet mass decreased to 17% and 11% respectively. Moreover, the machine efficiency and power factor improved. Therefore, the optimized model is satisfied machine performance and has a better output performance than the optimized model by DES.

Table 6   Design results of the optimized model by DES and final optimized model.

Design parameter in LPM	Optimized by DES	After Iteration by FEA
Stator winding	Concentrated	Concentrated
Number of Slots/poles	12/8	12/8
Series turns per phase	88	96
Rated current [Arms]	18.5	15.15
Stator OD [mm]	190	190
Axial length [mm]	75	62
PM flux linkage [mWbrms]	55	56.62
Total Magnet mass [Kg]	0.595	0.535
Armature loss [W]	74.3	60.27
Efficiency [%]	96.8	97.3
Power factor	0.98	1

Figs. 20 and 21 compare the back-EMF and PM flux linkage between the optimized model by DES and the final optimized designs. As we can see, even though the axial length and the magnet mass are decreased, back-EMF and PM flux linkage of the final optimized model are very close to the optimized model by DES.
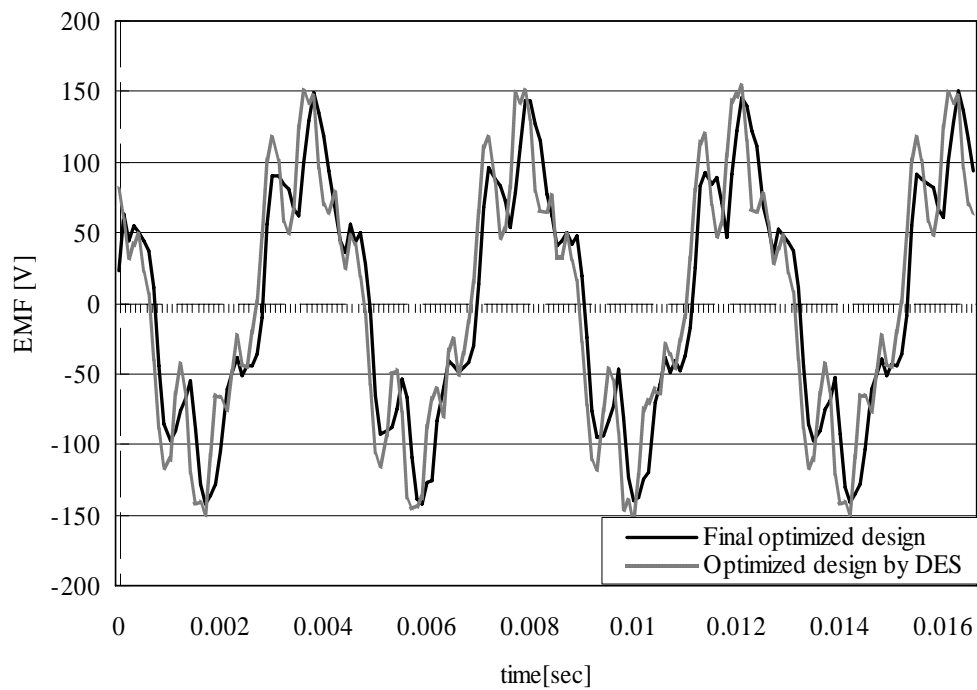
Fig. 20   Back-EMF of optimized design by DES and final optimized design.
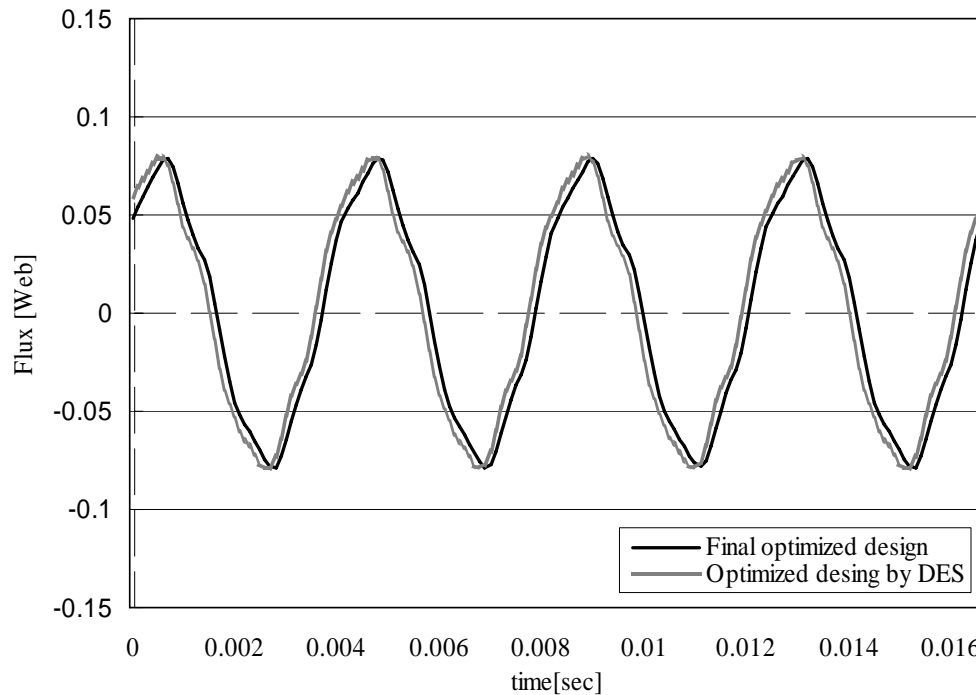
Fig. 21   PM flux linkage of optimized design by DES and final optimized design.

The cogging torque and output torque ripple are simulated to analyze machine output performance and shown in Figs. 22, 23. The cogging torque of the final optimized model is 0.5 Nm and it performed better than the optimized model by DES with 1.5 Nm cogging torque. The average output torque is reduced from 11.4 Nm to 8.7 Nm for the 3.3 kW output power by fine tuning between LPM and FEA which makes it possible to decrease the rated current and increase machine efficiency. However, the output torque ripple is somewhat higher than the optimized model by DES because in the LPM, the DES optimization process focuses on machine cost and output performance. The output torque ripple will be handled by the direct output power control in the generating mode.
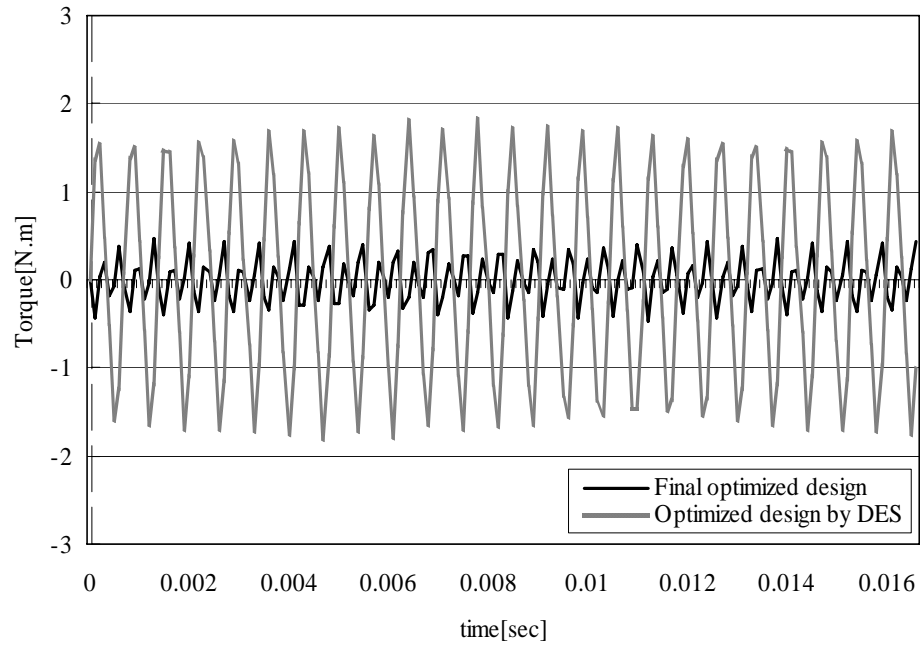
Fig. 22   Cogging torque of optimized design by DES and final optimized design.
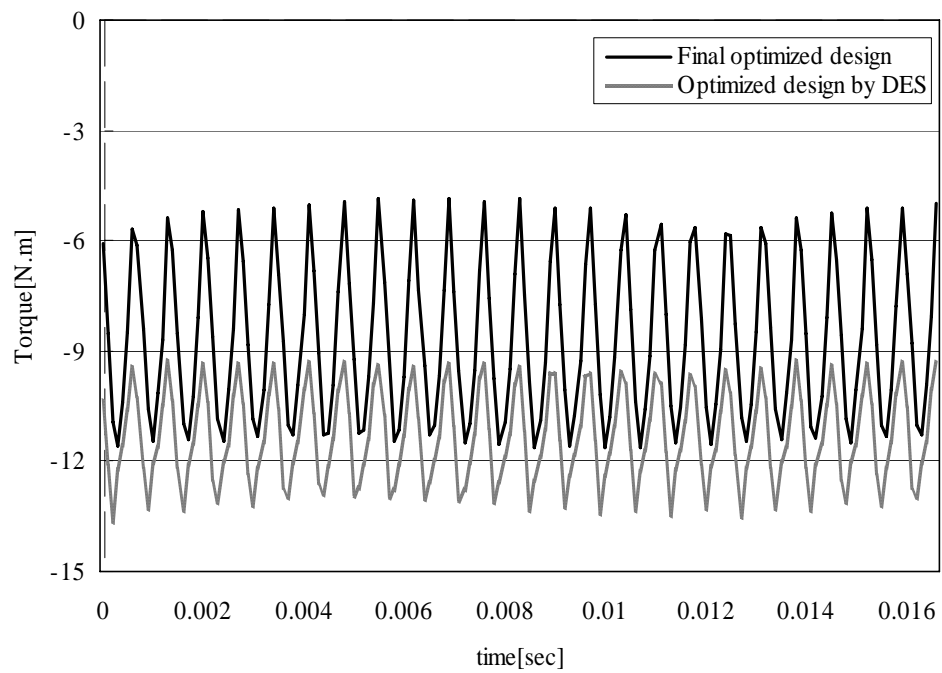
Fig. 23   Output torque of optimized design by DES and final optimized design.

3.2.3. Comparisons between Optimized Design Results with the Distributed and

Concentrated Winding Machines

Finite element analysis is performed in order to verify the optimized design from LPM and DES. Using FEA, the back-EMF and the PM flux linkage are compared to results obtained from LPM. Also, the output torque ripple and the cogging torque can be analyzed. Figs. 24, 25 depict the Back-EMF and the PM flux linkage for comparisons between distributed and concentrated winding configurations. To compare the cogging torque and the output torque ripple, FEA is performed and results are shown in Figs. 26, 27.
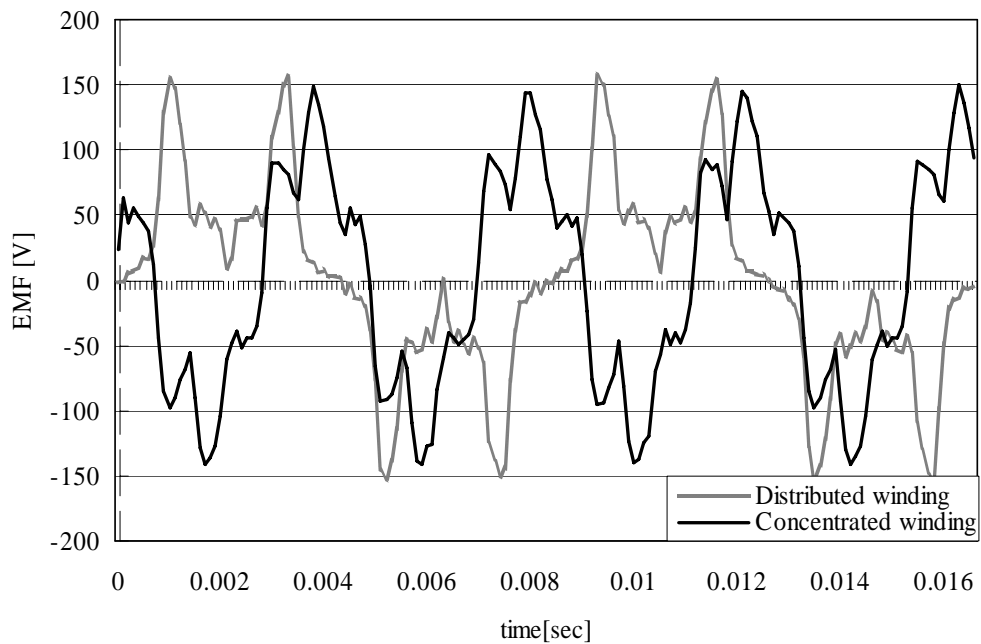
Fig. 24   Back-EMF of distributed and concentrated winding machines.
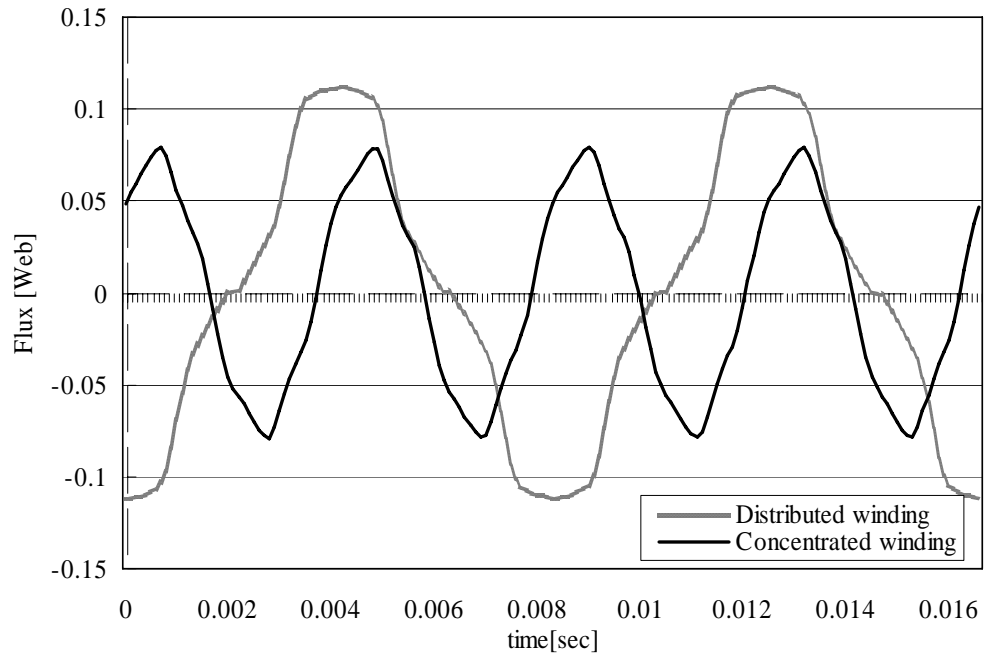
Fig. 25   PM flux linkage of distributed and concentrated winding machines.
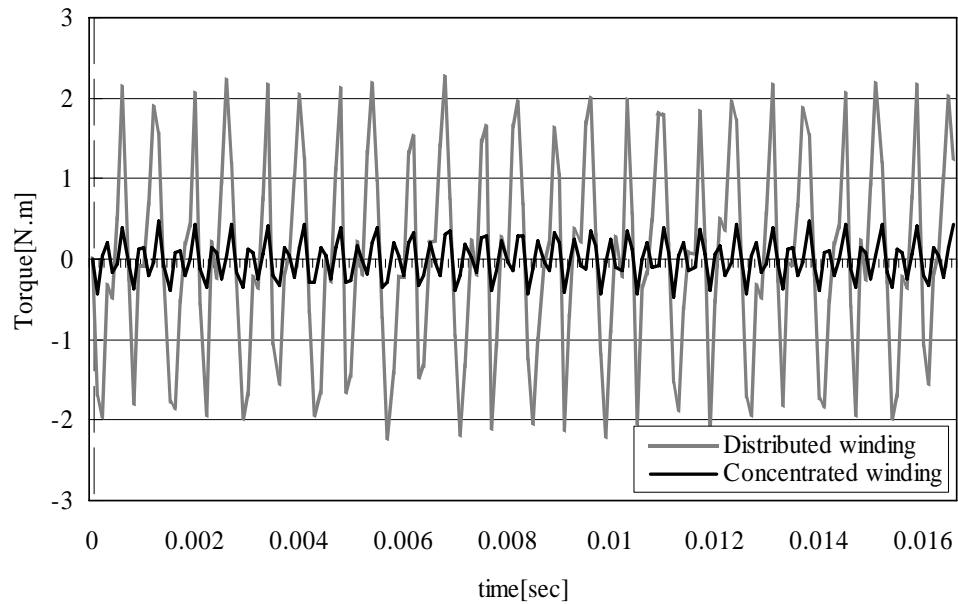
Fig. 26   Cogging torque of distributed and concentrated winding machines.
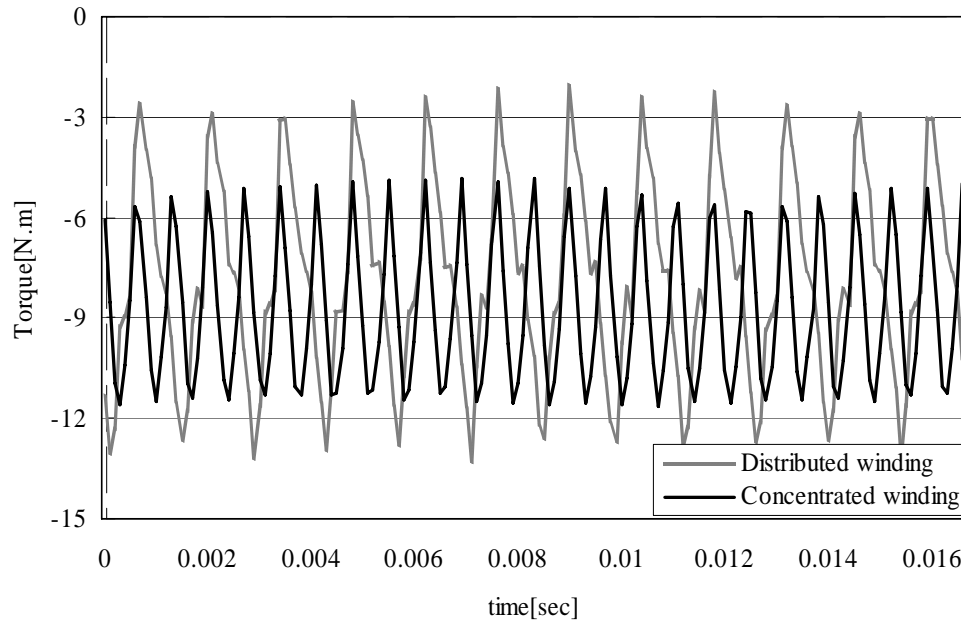
Fig. 27   Output torque of distributed and concentrated winding machines.

From the FEA results, the cogging torque is reduced from 2N.m to 0.5N.m in the concentrated winding machine. Moreover, output torque ripple is decreased from 68.8% to 33.5%. Therefore, the final optimized model with concentrated winding has better output performance and low torque ripple.

Figs. 28 and 29 show the back-EMF waveforms from FEA and its fundamental component. From the FEA result, the back-EMF is not pure sinusoidal. Therefore, it needs to be transformed to a fundamental value using the Fourier transform. Through FFT analysis, the peak value of the fundamental component is 116 V and the rms value of back-EMF can be calculated as 82 Vrms. In the final optimized model using Lumped Parameter Model (LPM), the back-EMF design result is 85.38 Vrms. Therefore, the back-

EMF results from LPM and FEA are very close and the error between FEA and LPM is 4%.
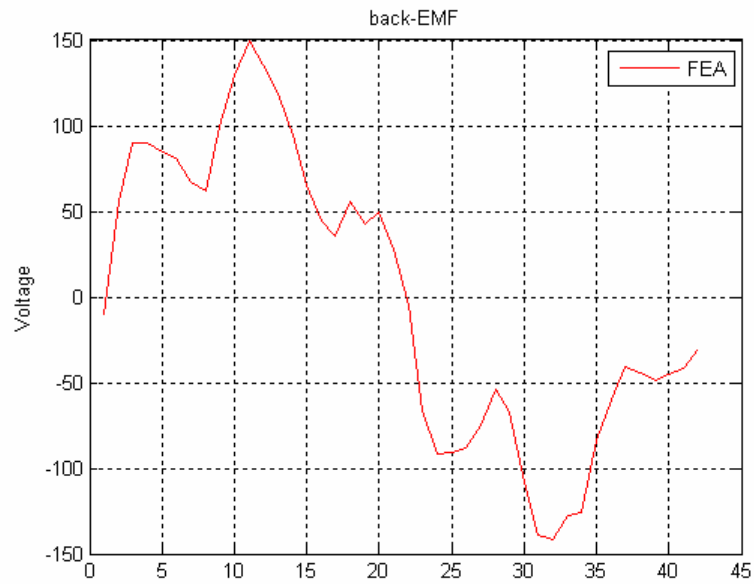
Fig. 28   Back-EMF result from FEA.
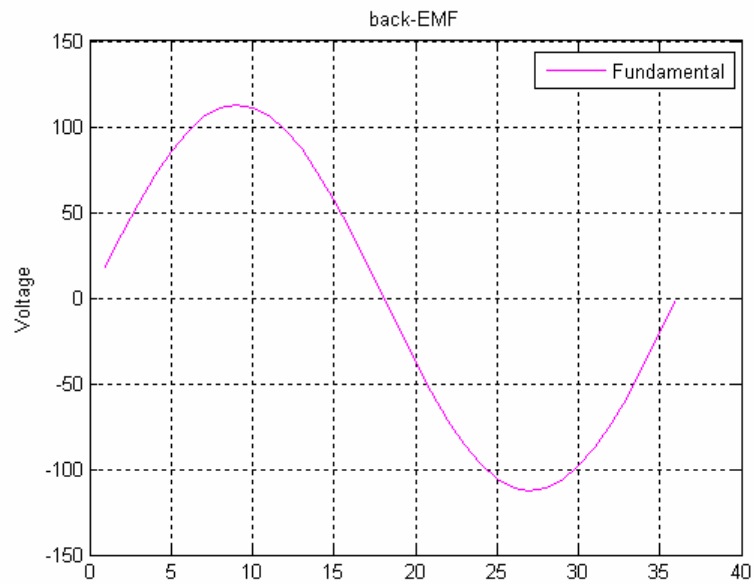
Fig. 29   Fundamental component of back-EMF.

From the transient FEA simulation, the PM flux-linkage can be obtained; Fig. 30 shows the result. The peak value of the PM flux-linkage fundamental component is 0.076Wb from FFT as shown in Fig. 31. Therefore, the rms value of the PM flux- linkage can be calculated as 0.0538Wbrms from FEA while the PM flux-linkage result from the LPM is 0.0566Wbrms. From these results, the PM flux-linkage results from LPM and FEA are very close and the error between FEA and LPM is 5%.
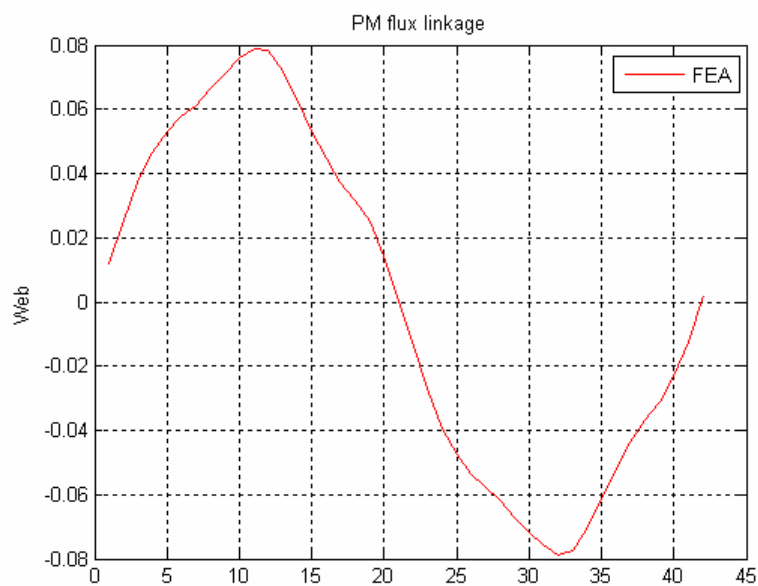
Fig. 30   PM flux-linkage result from FEA.
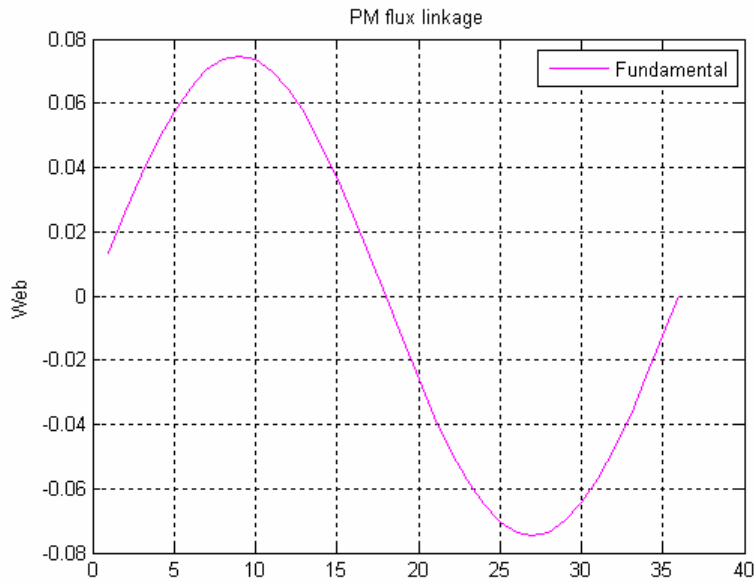
Fig. 31   Fundamental component of PM flux-linkage.

This chapter summarizes the comparisons between the final optimized model of LPM and FEA. The final optimized model is fine tuned between LPM and FEA after several iterations. Finite element analysis is performed to verify the optimized design from LPM and DES. Using FEA, the output power, the back-EMF and the PM flux linkage are compared to results obtained from LPM.

In the final design by LPM, the rated power is set to 3,300W to consider a 10% margin for the actual machine operation performance. From FEA, the simulation result of average output power is 3,287W; the same rated current is 15.15A with LPM. In terms of back-EMF, the rms value from FEA is 82Vrms and the LPM design result is 85.38Vrms. Also, the rms value of PM flux- linkage is 0.0538Wbrms from FEA; the result from the

LPM is 0.0566Wbrms. In the final optimized design, errors between FEA and LPM are less than 5%. Therefore, the final optimized model is good enough to finalize fabrication.

CHAPTER IV

FABRICATED 3KW PMA-SYNRG AND MACHINE CHARACTERISTICS

4.1. Machine Fabrication Process

Fig. 32 shows the machine fabrication process for the 3kW PMa-SynRG. The stator core needs the winding process and the rotor needs to be assembled with cover and shaft.
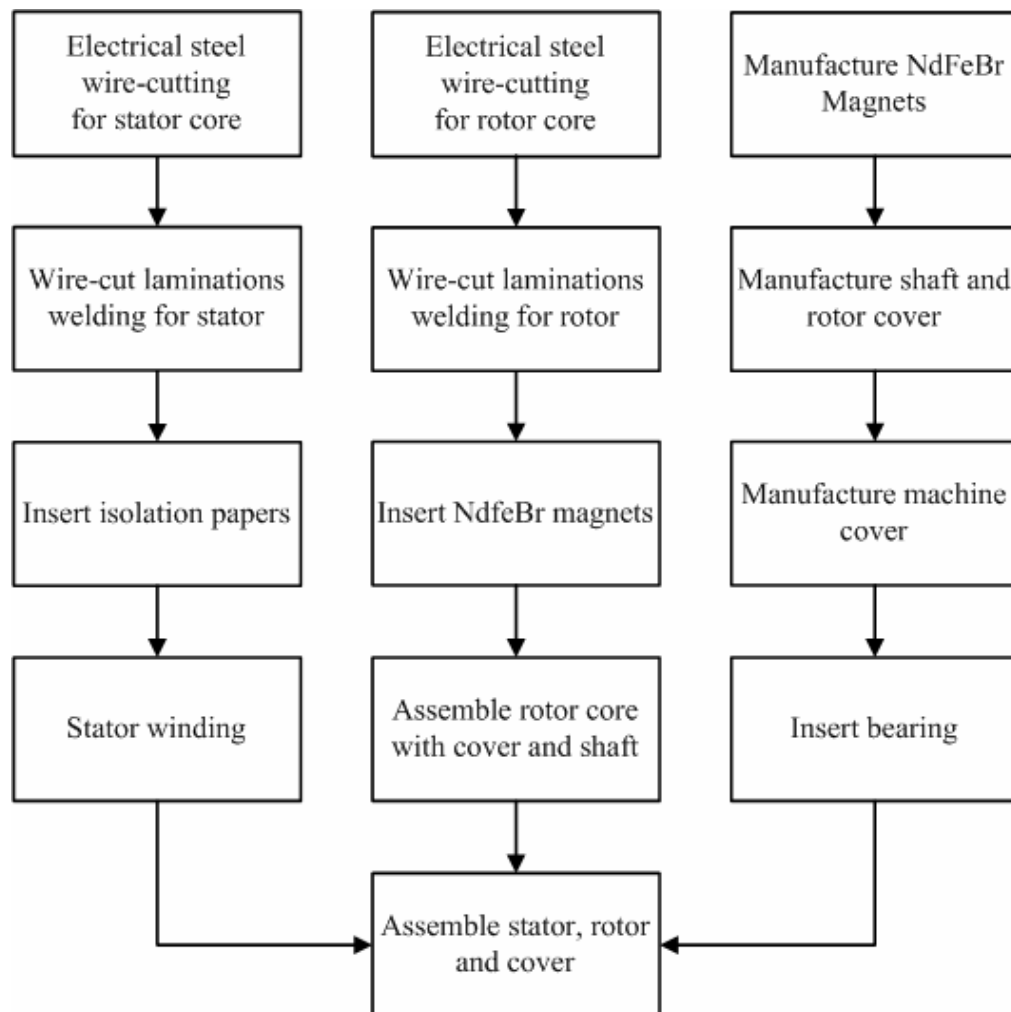
Fig. 32   Block diagram of machine fabrication process.

4.1.1. Stator Core and Winding

Table 7 summarizes characteristics of the stator core and Fig. 33 depicts the stacked lamination. The thickness of each lamination is 0.35mm and the total stack length is 65mm. Therefore, 185 laminations are stacked and six points at the edge of core are notched for welding. In order to isolate the coil and stator core, all stator slots are covered by isolation papers.

Table 7 Stator core characteristics.

Grade	Thickness [mm]	Density [g/cm2]	Core loss [w/kg]	Lamination [%]
35PN440	0.35	7.7	4.4	95

Fig. 33 Stacked lamination stator core.

Concentrated stator winding was selected for the 3kW PMa-SynRG. Figs. 34 and 35 picture the produced stator core and winding. The number of turns per each stator slot is 24 and the total number of turns per each phase is 96. The estimated phase resistance was 0.175ohm in the LPM and the measured value was 0.2ohm. Therefore, the actual machine has 10% greater resistance because the volume of the end-turn is bigger than expected. The slot fill factor of the stator winding set 40% in the design process to consider the winding by hand.

Fig. 34   Side-view of the stator winding configuration.
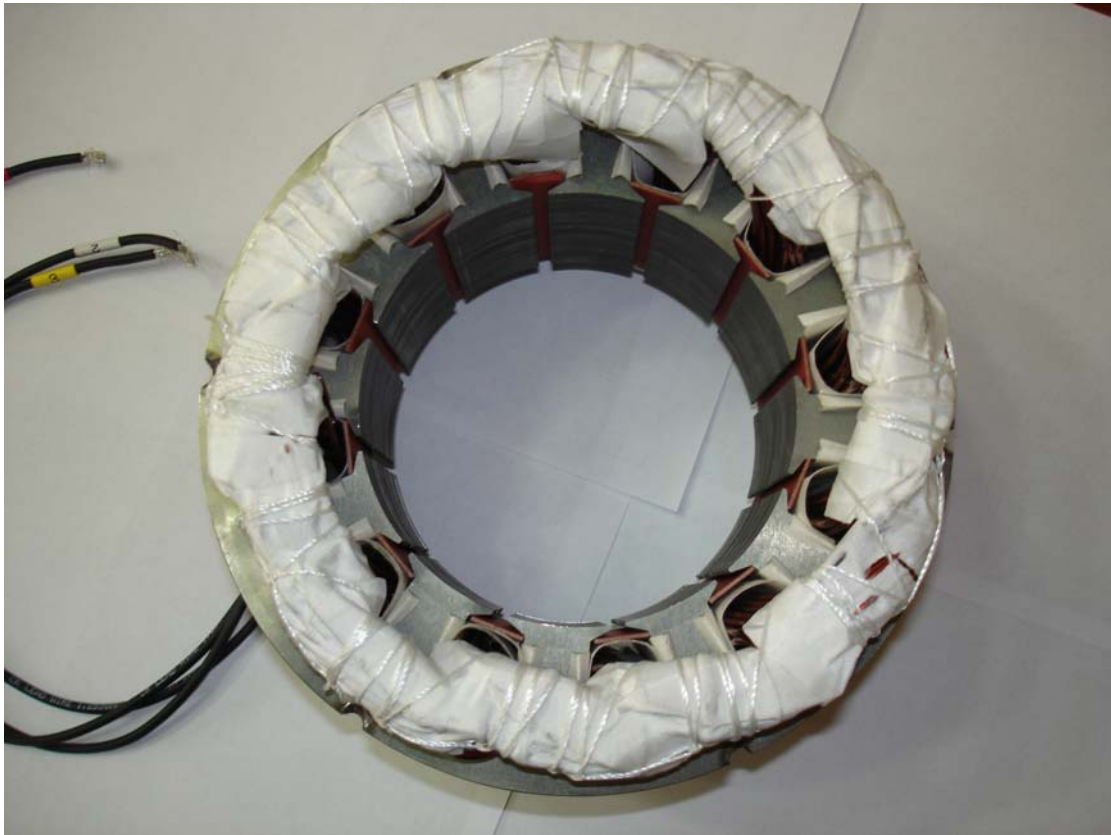
Fig. 35   Top-view of the stator winding configuration.

4.1.2. Rotor Core and Permanent Magnets

The total stack length of the rotor core is 65mm and NdFeB permanent magnets are embedded in the second layer of the rotor bridge. In order to prevent magnets escaping at high speed, a hub will be inserted between the rotor core and the shaft will be fixed by two square shaped keys. Table 8 summarize characteristics of NdFeB.

Table 8 Characteristics of NdFeB permanent magnet.

Grade	Remanence Br [T]	Maximum energy BHmax [MGoe]	Recoil permeability	Thermal Characteristic
N42SH	1.27 ~ 1.32	39 ~ 43	1.05	~ 150 degree
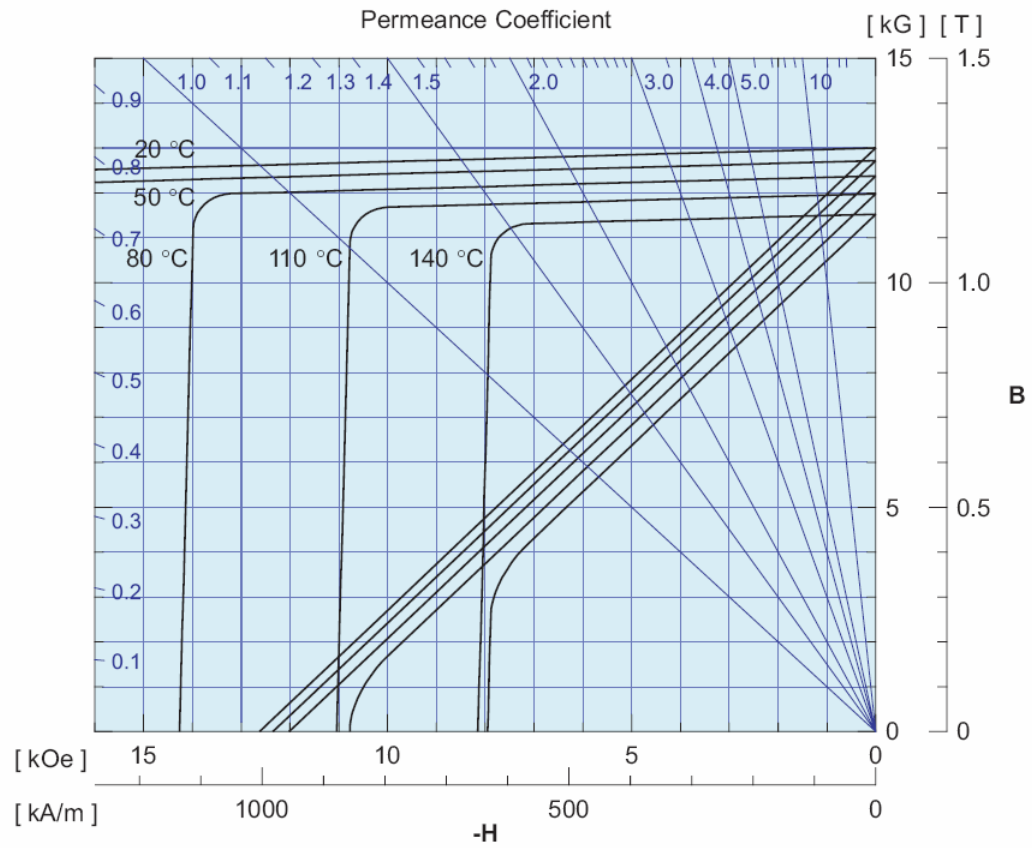
Fig. 36   B-H curve of NdFeB permanent magnet.

Fig. 37   NdFeB permanent magnets.

Figs. 36, 37 depict B-H curve and feature of NdFeB. NdFeB permanent magnets are inserted in the second layer of the rotor core and they are fixed by notches at the end of corners. The stacked lamination rotor core and inserted PMs are shown in Fig. 38.

Fig. 38   Stacked lamination rotor core and inserted PMs.

4.2.   Experimental Results

Fig. 39 shows the 3kW PMa-SynRG test bed. A 7.5hp three phase induction motor is controlled by the Allen-Bradley 1336 plus adjustable frequency AC drive for 3,600rpm constant speed and works as a prime mover. The fabricated 3kW PMa-SynRG is connected to the induction motor directly by a coupling.
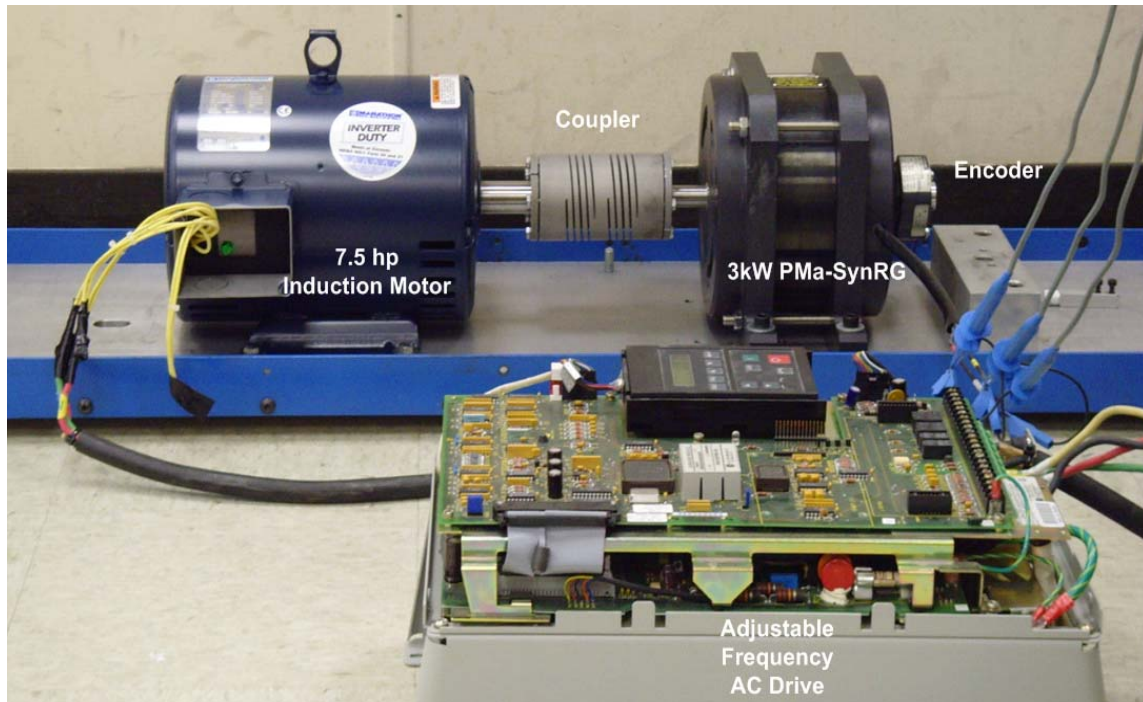
Fig. 39   Fabricated 3kW PMa-SynRG test bed.

The rotating frequency of the induction motor is 60Hz for 3,600rpm and the PMa-SynRG is 240Hz because the induction motor has two rotor poles and the PMa-SynRG has eight rotor poles. In order to detect the mechanical rotating position, an encoder installed on the PMa-SynRG shaft is being used. The fabricated test bed for the 3kW PMa-SynRG is shown in Fig. 39. The adjustable frequency AC drive is programmed to keep the constant speed (3,600rpm) of the three phase induction motor. The 3kW PMa-SynRG is working as a generator; the phase conductors are connected to the three phase rectifier and voltage sensors.

4.2.1. Comparisons for Back-EMF

Fig. 40 shows experimental waveforms of the line-to-line back-EMF. When the induction motor runs at 3,600 rpm, the peak value of the line-to-line back-EMF between phase A and B is around 150V. Each rotor pole has a uniform peak value indicating that each permanent magnet has equal remanent flux density Br.
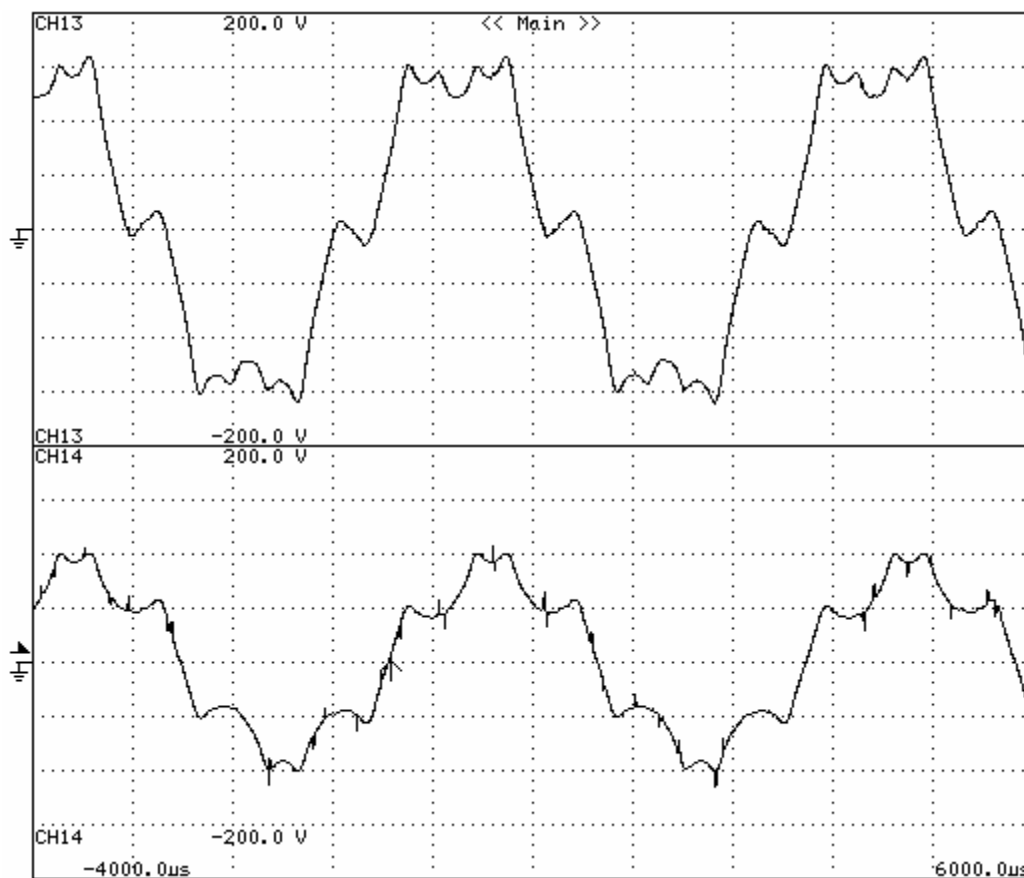
Fig. 40   Waveforms of line-to-line and line-to-neutral back-EMF.

From top to bottom : (a) line-to-line back-EMF(50V/div) (b) line-to-neutral back-EMF(50V/div)

Figs. 41 and 42 describe the back-EMF waveform from the experiment and calculated fundamental component. The shape of the waveforms is different because of the saturation effect in the experiment. The peak value of the fundamental component of the experimental result is higher than the FEA simulation result.
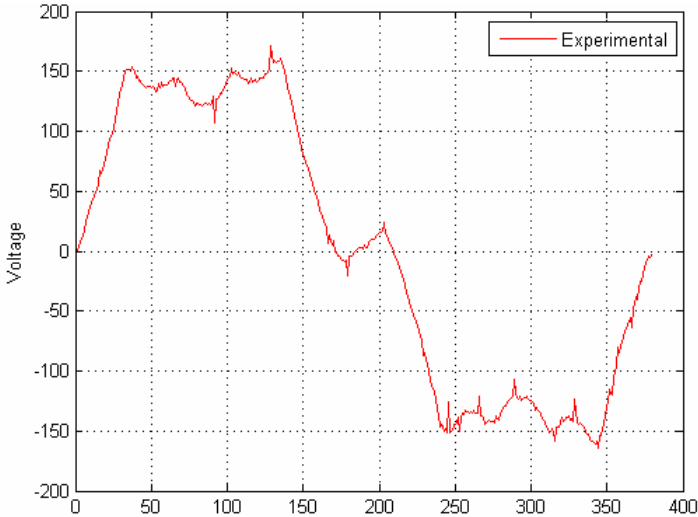
Fig. 41   Waveform of the line-to-line back-EMF from the experiment.
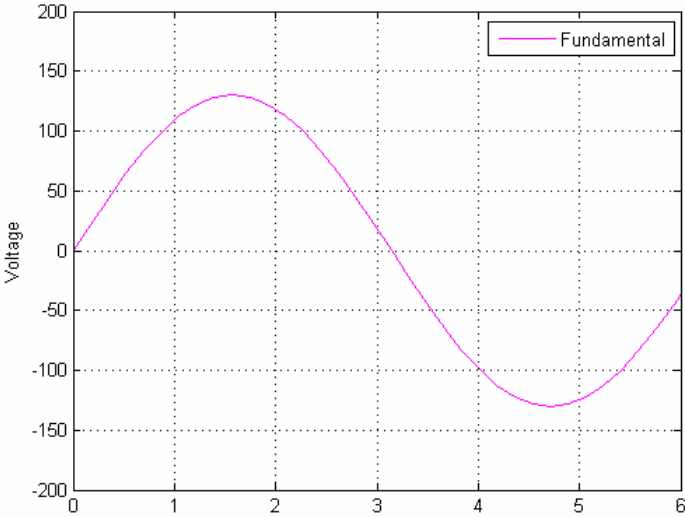
Fig. 42   Fundamental component of the line-to-line back-EMF from the experiment.

Table 9 summarizes the back-EMF design results from the LPM, FEA and experiments. The rms value of the experimental result is 91.8V which is 10V higher than the FEA result. The smaller ripple waveform of the back-EMF in the experiment can produce bigger rms and reduce the size of the DC link inductance to rectify pure DC current and voltage.

Table 9   Comparisons of the back-EMF from the experiment.

	LPM	FEA	Experimental	Error
back-EMF [Vrms]	85.4	82	91.8	10 %

4.2.2.   Comparisons for d q-axis Inductances

Figs. 43 and 44 show comparisons between experimental results and estimations for d q-axis inductances. The measured d-axis inductance by the experiment is close to the LPM and FEA predictions. At lower currents, the inductance measurements are off from the LPM predictions because of the uncertainty associated with the low value of currents and voltages. However at higher currents, the measurement plots follow the LPM predictions closely. The FEA prediction plots have a similar trend with experimental result. However, while being lower than the experimental result at overall currents. The d-axis inductance measurements by experiment are very close to the LPM predictions at higher currents. The FEA predictions are close the measurements and seem to be higher at higher currents. From these results, agreement between measured and predicted value for d q-axis inductances are reasonably good.
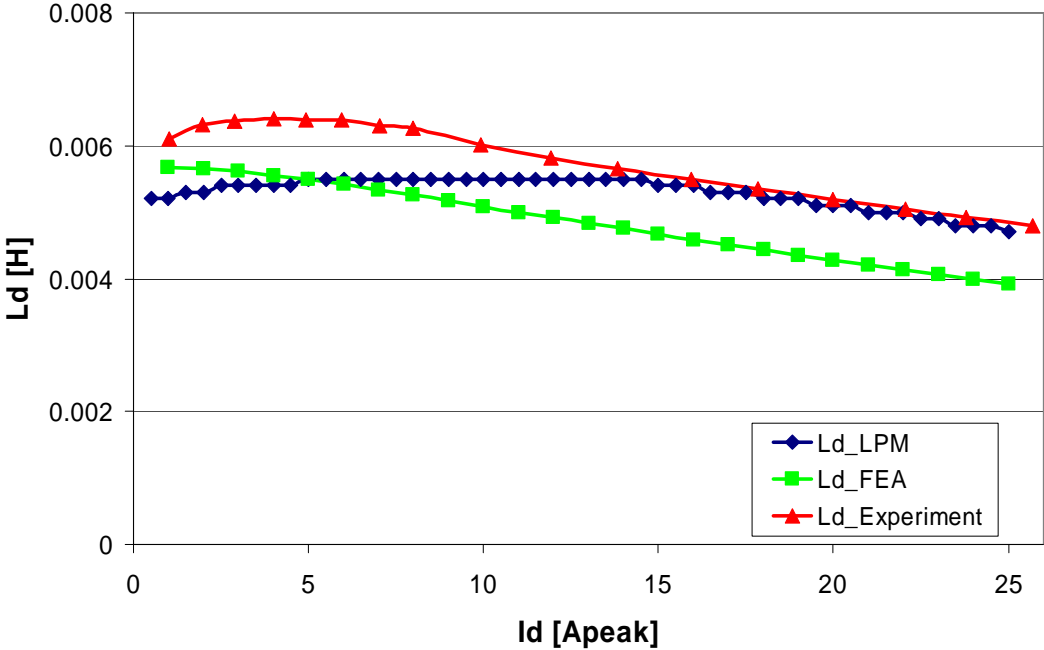
Fig. 43   Measured d-axis inductance characteristics, compared with LPM and FEA.
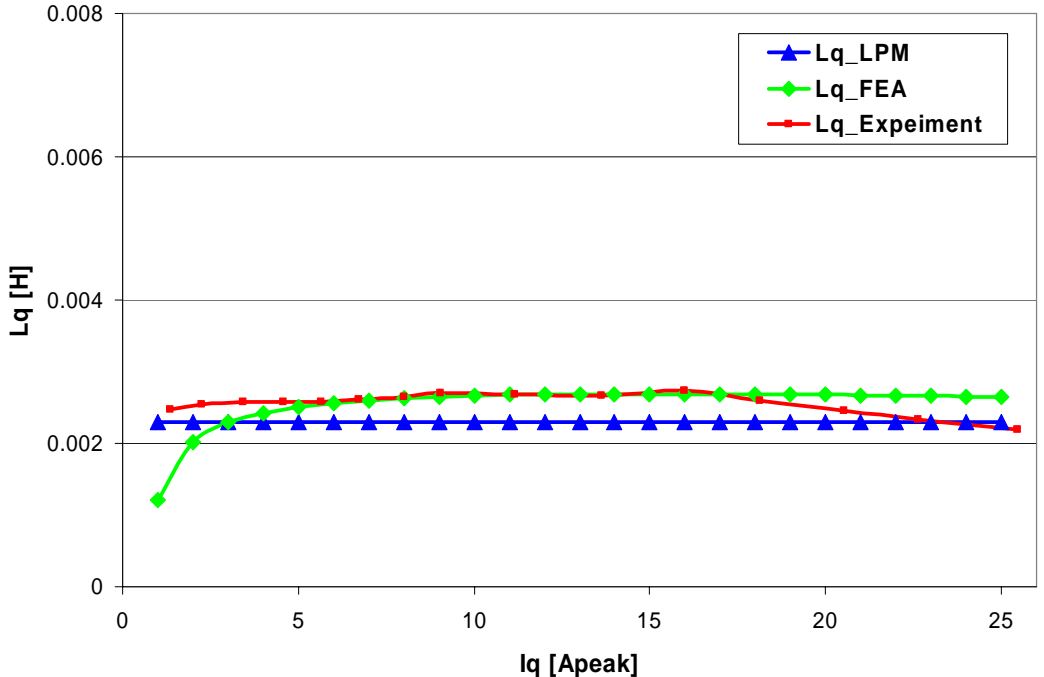
Fig. 44   Measured q-axis inductance characteristics, compared with LPM and FEA.

CHAPTER V

CURRENT-FED DRIVE FOR THE GENERATOR SYSTEM

5.1. Current-Fed Drive for the 3kW PMa-SynRG

This section discusses the basic operation of the proposed low loss PMa-SynRG drive system. The proposed drive topology of a low loss current-fed drive system is shown in Fig. 45. Three-phase input power is produced by the 3kW PMa-SynRG with the engine working as a prime mover. There is a three-phase controlled rectifier at the input and a current source inverter at the output with a large DC link inductor. The output inverter distributes the DC link current to single-phase load. In order to simplify the analysis, all the stray elements are neglected. The machine is assumed ideal and all the saturation effects are neglected.
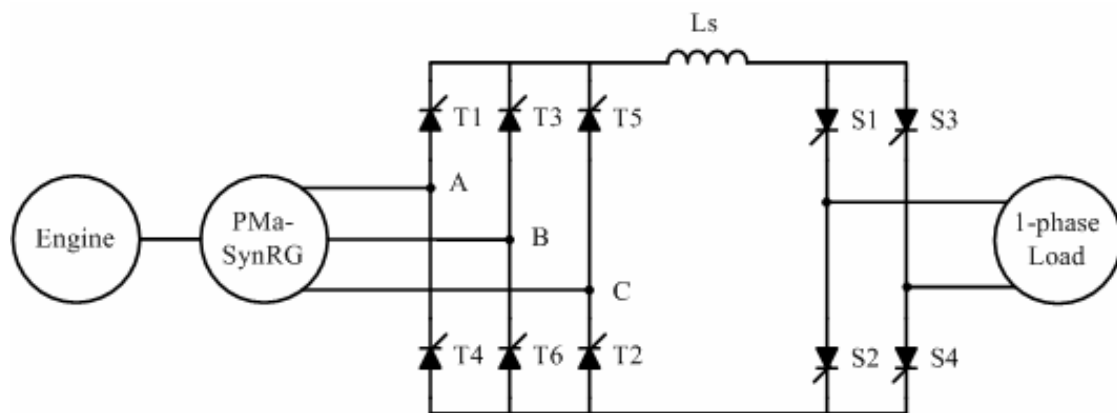
Fig. 45   The proposed thyristor-based current-fed drive.

5.2. Thyristor Based Three-Phase Controlled Rectifier

The input stage is made up of a three-phase line commutated controlled rectifier. The triggering signals for the input rectifier thyristors are synchronized with the line-to-line input voltage Vac. A software timer generates an adjustable delay from the rising and falling edges of the zero crossing detector (ZCD) output to control the output voltage of the controlled rectifier. The DC link current is changed by changing the delay angle of the input rectifier. This DC link inductor acts as a filter to smooth out the ripple in the output of the rectifier. The DC link inductor, along with the controlled rectifier, forms a variable current source. The delay angle of the controlled rectifier can be varied as fast as twice the frequency of the input supply. This means that with a 60 Hz input one could control the rectifier output only as fast as 8.33 milliseconds [46]-[47].

In case the alpha is zero, the switching sequence of the three-phase rectifier starts at Vac zero. For the starting point of the switching sequence, a zero crossing point of the phase AC line-to-line voltage is detected. From the zero crossing point, thyristor T1 is conducted during $60\degree$. In Fig. 46, phase voltages of the PMa-SynRG and the switching sequence of the three-phase rectifier appear when the rectifier control angle alpha is zero.

The output voltage of the input rectifier is a cosine function of the delay angle. The effective output voltage of the input rectifier is positive for the delay angle below 90 degrees. Fig. 47 shows the output voltage waveforms of the controlled rectifier for various values of the delay angle. In Fig. 47, the switching sequence is delayed from $\omega t = 0$ point to the alpha angle and the DC link voltage decreases from the alpha zero case.
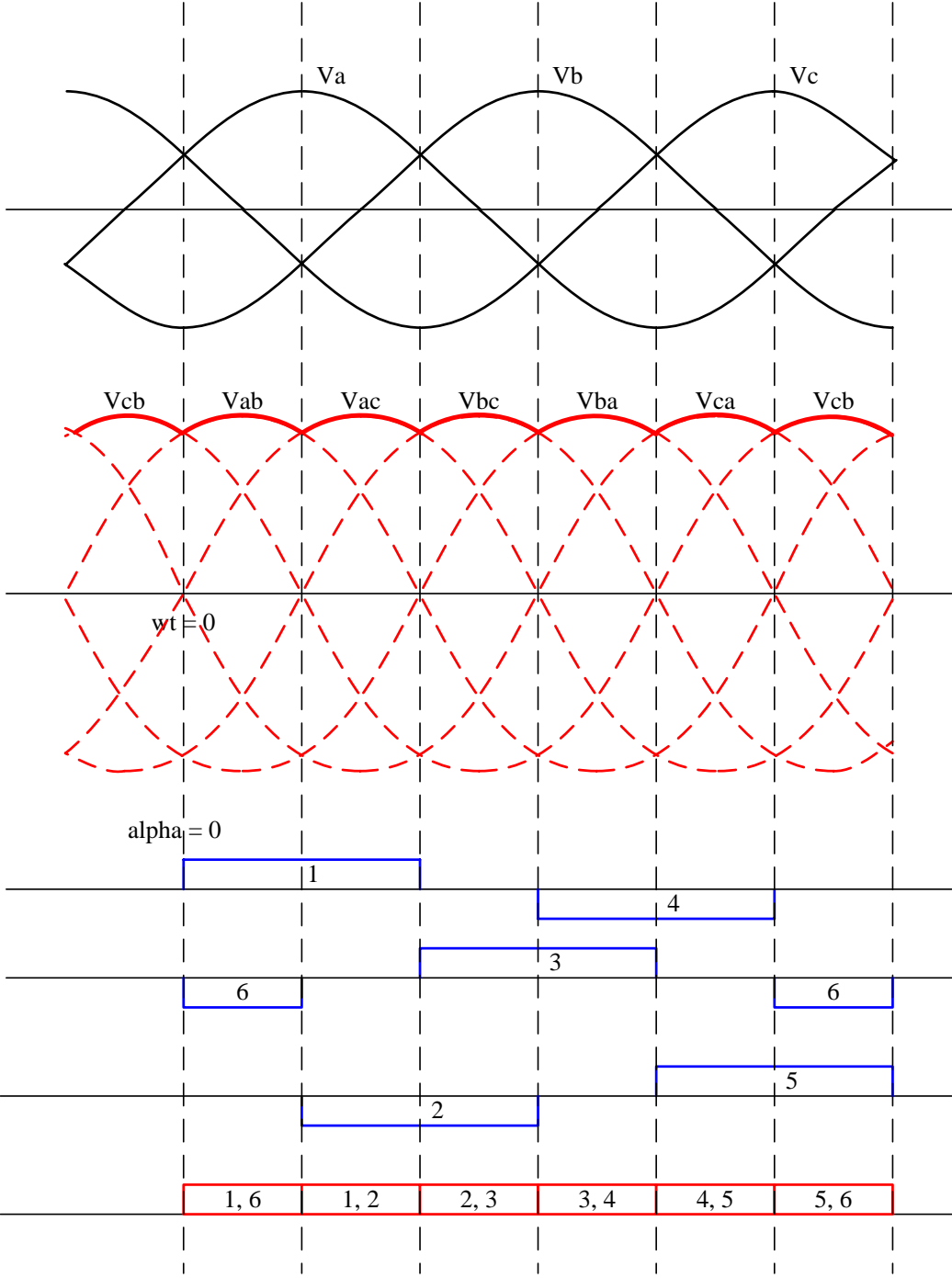
Fig. 46   Switching sequence for the three-phase rectifier at alpha zero case.
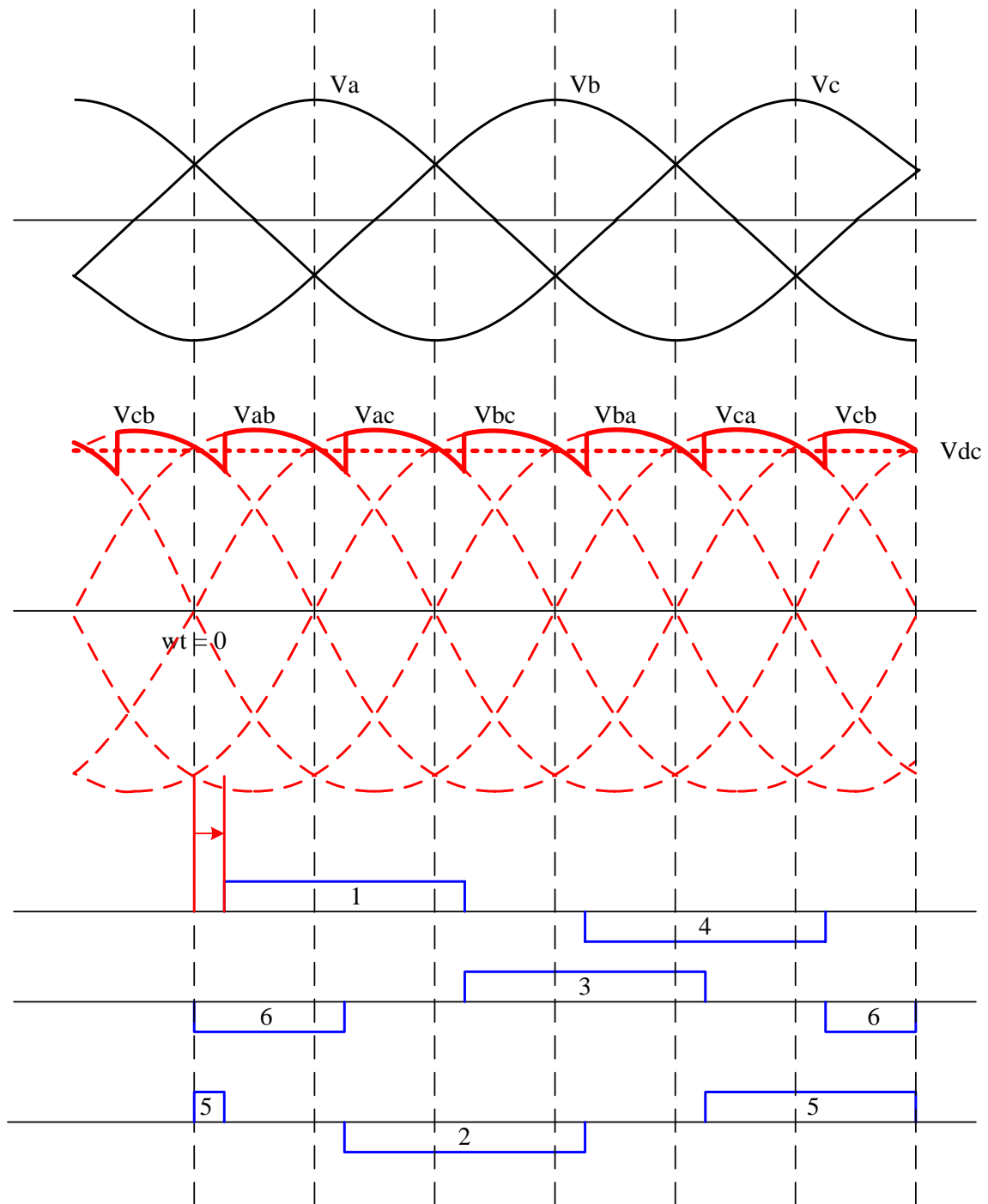
Fig. 47   Switching sequence for the three-phase rectifier with alpha control.

5.3. Thyristor Based Single-Phase Controlled Inverter

At zero delay angle, the input current of the rectifier is an ideal square wave and in phase with the input voltage. Under these conditions, the displacement factor is unity and the power factor is equal to the distortion factor of the system. A square wave current waveform in phase with the voltage results in a unity power factor

5.3.1. Load Commutated Inverter

A typical schematic of current-fed load commutated inverter (LCI) for the motoring mode is shown in Fig. 48. The LCI drive uses a single-phase controlled rectifier at the input and a current source inverter at the output with a large DC link inductor. The output converter distributes the DC link current to three-phases of the load. The back-EMF generated by the load is used for natural commutation of the inverter thyristors; line commutation is used to commutate the input rectifier thyristors.
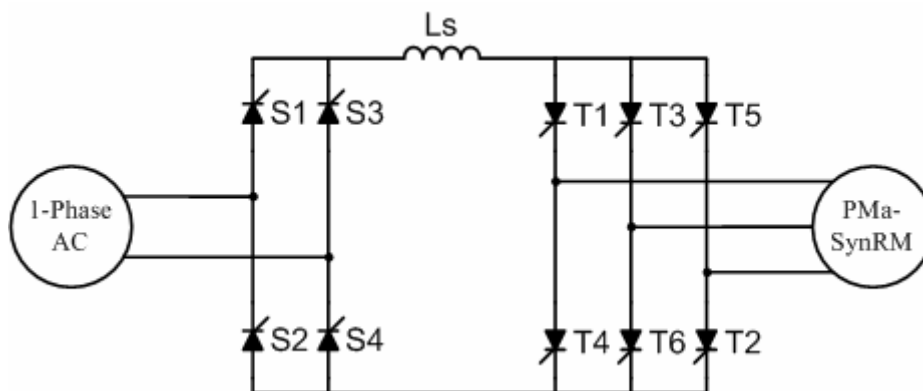
Fig. 48   Load commutated inverter topology.

For the successful commutation of the thyristor, it is necessary for the motor phase current to lead the corresponding phase back-EMF. The leading angle is a function of various system parameters such as switching time of thyristor, load and DC link inductance [48]-[49].

5.3.2. Forced Commutated Inverter by the Auto-Sequential Circuit

A current-fed inverter requires forced commutation if the load back-EMF is not sufficient for load commutation. The load commutation of an inverter with PMa-SynRM load depends on the back-EMF. Therefore, the machine should not operate below a critical speed. Typically, the load commutation does not work satisfactorily below 5% of base speed. Also, for the synchronous reluctance machine, the inverter needs some type of forced commutation because this type of machine has very limited back-EMF at low speeds [50].

Fig. 49 depicts a three-phase bridge inverter with an auto-sequential method of forced commutation. The PMa-SynRM model is approximately represented by a per-phase equivalent circuit consisting of a sinusoidal back-EMF in series with an inductance L. At the stalled condition of the machine, the back-EMF is zero and the motor becomes an inductive load. Thyristors T1-T6 are the principal switching devices of the inverter where each of them conducts in sequence, ideally for $2\pi/3$, to establish the usual six-stepped current waveforms in the machine. The series diodes and delta-connected capacitor banks, which are connected to each of the upper and lower groups of thyristors, constitute the forced commutation elements. The capacitors store a charge

with the correct polarity for commutation while the series diodes tend to isolate them from the load [51].
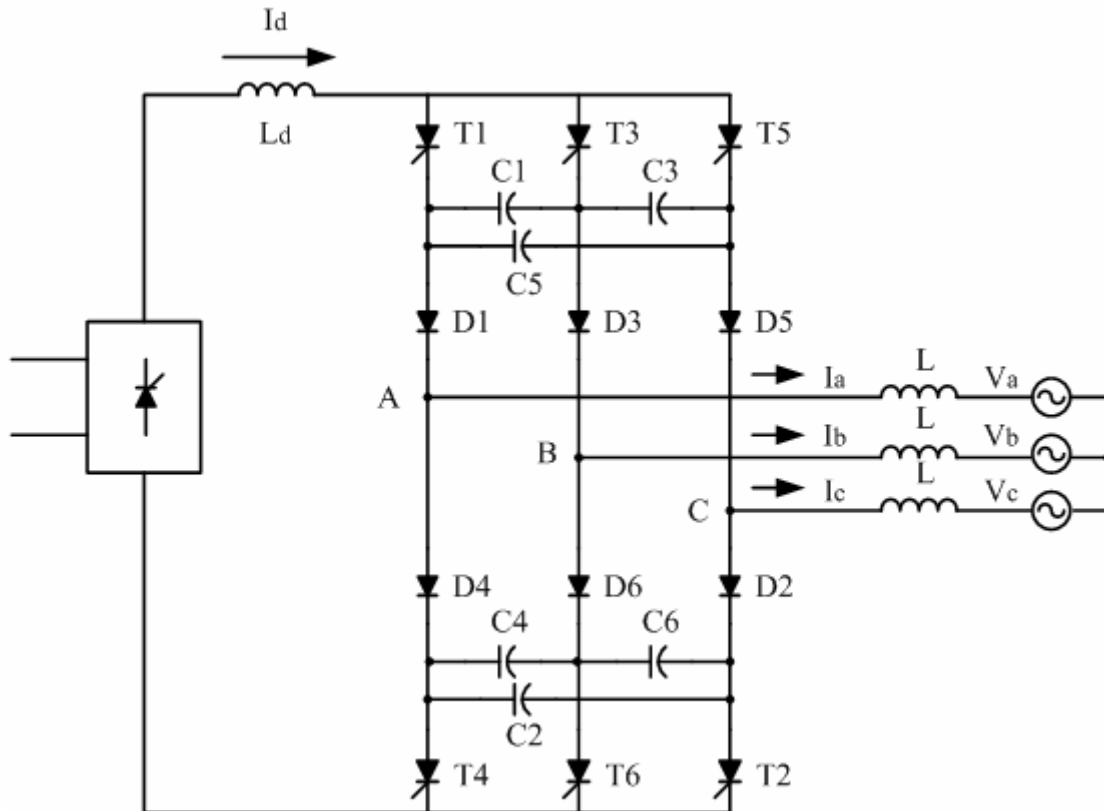
Fig. 49   Auto-sequential current-fed inverter (ASCI) with three-phase load.

Fig. 50 shows the overall system for the single phase inverter and three-phase force commutated converter using an auto-sequential circuit. This system is used if the machine back-EMF is not large enough for load commutation or the machine is stalled. In this simulation, 100uF capacitor banks are used to store an electric charge for commutation. Fig. 51 describes simulation results of the DC link current and voltage by ASCI circuit.
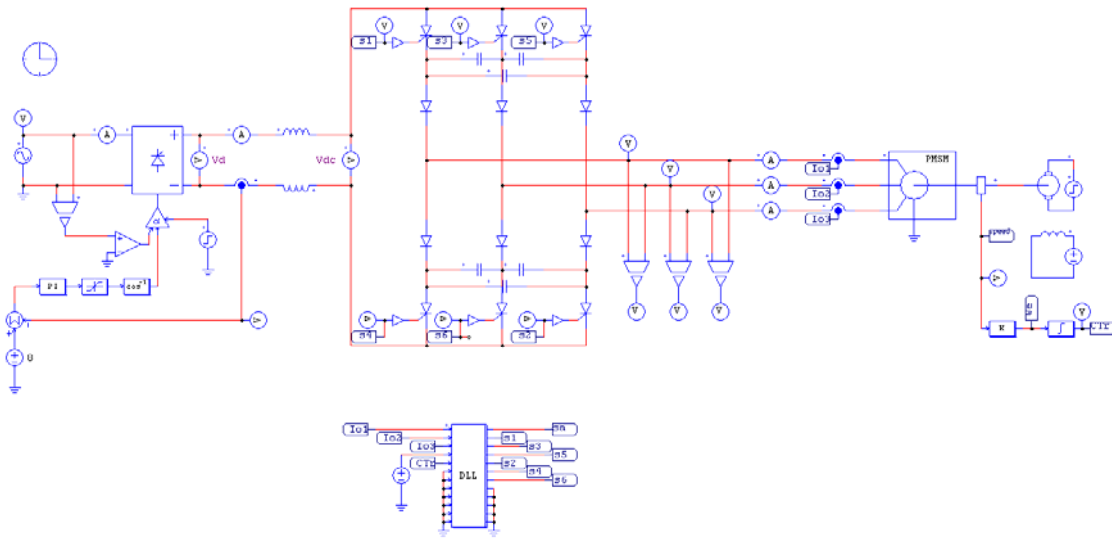
Fig. 50   Schematic of force commutated inverter system.
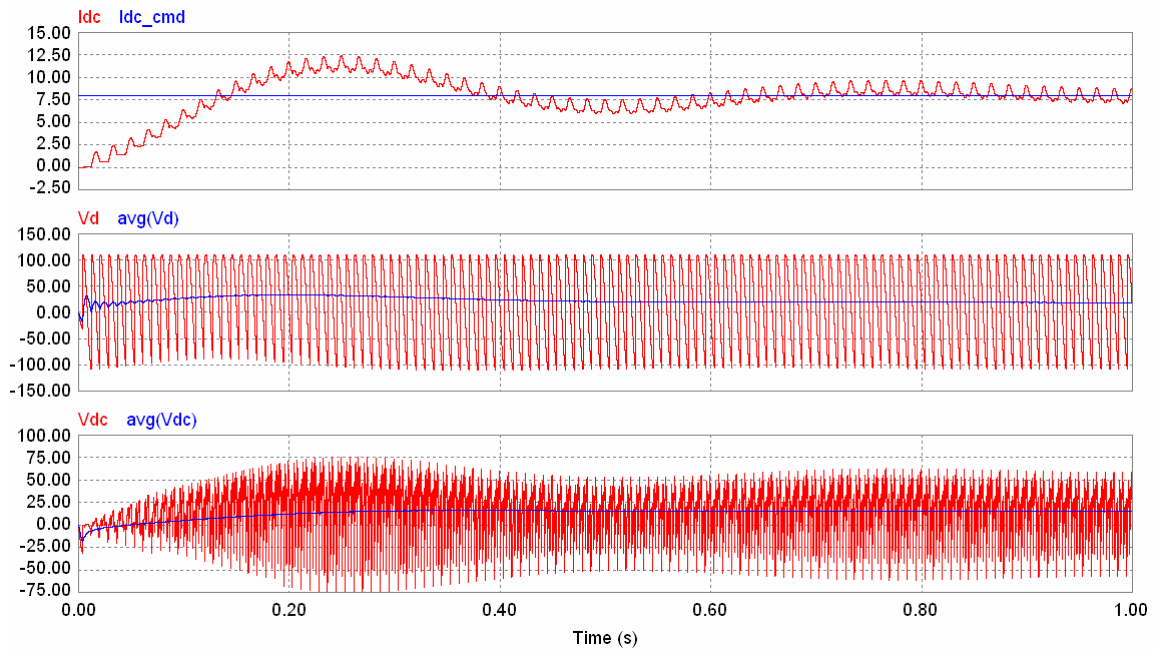
Fig. 51   Waveforms of the DC link current and voltages.

From top to bottom : (a) DC link current, DC link current command (b) DC link voltage

before the inductance, average value (c) DC link voltage after inductor
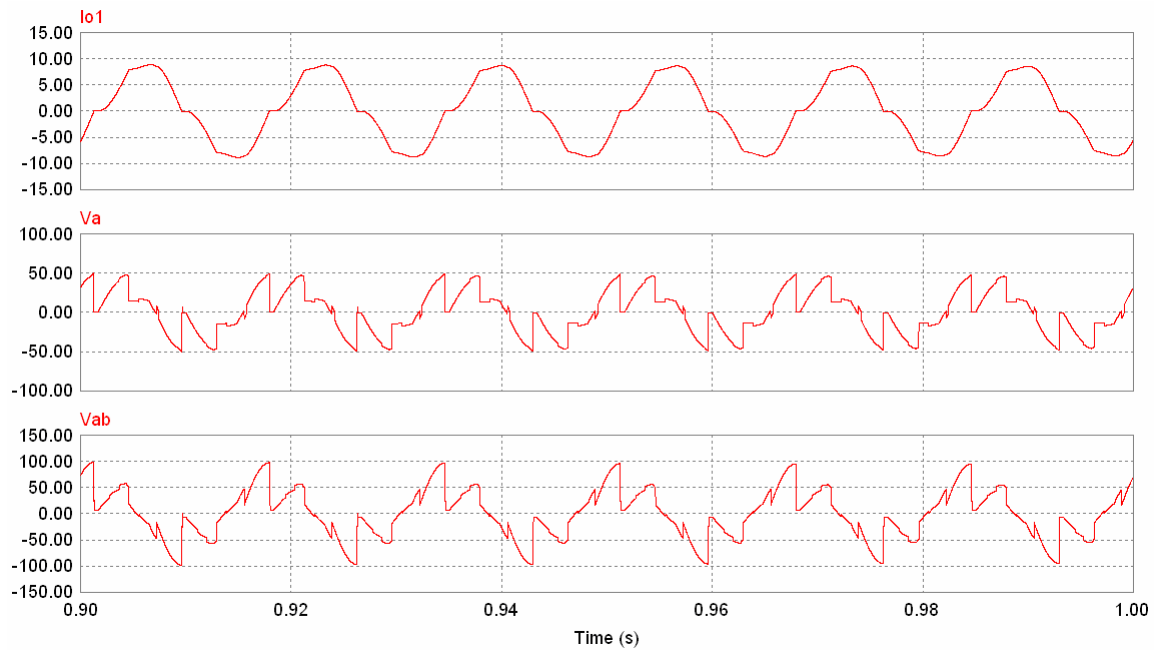
Fig. 52   Waveforms of the output current and voltages.

From top to bottom : (a) phase A current (b) phase A voltage (c) line-to-line voltage

During the current transfer interval, a large voltage spike is induced which will be added to the back-EMF and it is shown in Fig. 52. The response time of an auto-sequential current-fed inverter is much longer than the load commuted inverter because the capacitor banks charge linearly with the DC current and the linear charge period ends when the capacitor bank voltage equals the line voltage.

5.3.3.   Forced Commutated Inverter by a Line Capacitor

When the generator connected to a single phase inductive load, the inductive load will work at a lagging power factor. Therefore, an output capacitor is installed to convert the lagging power factor of the inductive load to the leading power factor of the inverter

terminal to turn off the thyristors. A schematic configuration of the LCI using an external capacitor and its vector diagram are shown in Fig. 53. The output load current Io in the inductive loads always lags the corresponding load voltage V_o with lagging angle θ depending on the inductive load characteristics. On the other hand, the output current Iinv must lead the load voltage for the thyristor commutation. The phase shift required from Io to Iinv is obtained by the output capacitor. The angle ϕ denotes the leading angle of the inverter terminal for safe commutation [52]. Furthermore, the output capacitor provides a smooth sinusoidal output current and voltage waveform for the 60Hz/120V single phase output.
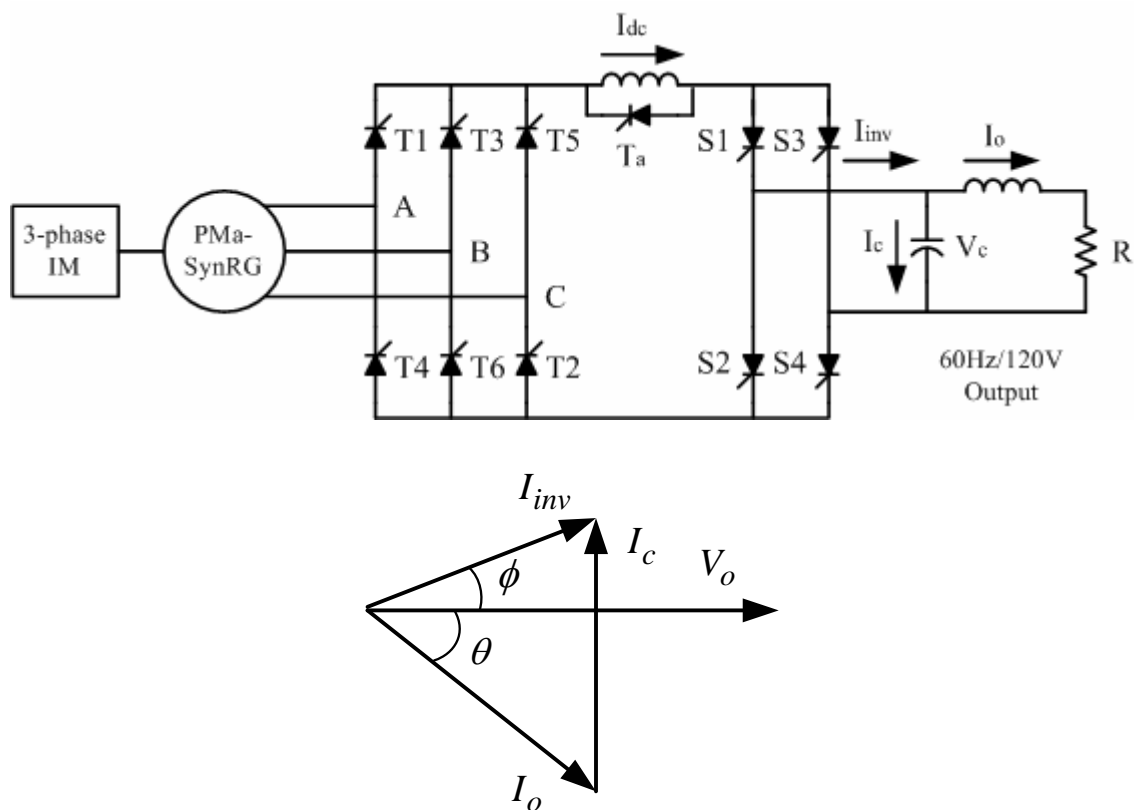
Fig. 53   The proposed LCI drive and forced commutated inverter vector diagram.

Using an output capacitor for the leading power factor allows commutation above the critical frequency of inductive load currents. However, in low frequency regions, an output capacitor cannot make a large enough phase shift because the capacitor current is too small due to high impedance of the capacitor. Since increasing the capacitance enough for the low frequency region could yield an unreasonably large capacitor, a forced commutation circuit is appended for low frequency operation. For the low frequency operation of a current-fed inverter, several forced commutation methods can be applied. The forced commutation control of a current-fed inverter using chopper commutation with an auxiliary thyrisotor (Ta) is introduced. The DC link current chopper commutation using an auxiliary thyristor can be applied to the generating operation for the single phase inverter. In this work, an output capacitor and forced commutation are considered for the overall frequency region of the inductive load. This scheme requires only one auxiliary thyristor to allow stable operation at standstill and low speed. The system is composed of a three-phase bridge converter, an auxiliary thyristor in DC link and a single-phase inverter. In this inverter, forced commutation devices such as capacitors and diodes can be dispensed with. In the present scheme, such chopping is combined with control of an auxiliary thyristor anti-parallel to the DC link inductor to improve starting commutation ability for PMa-SynRM at the starting motoring mode [53]. The DC link voltage is chopped by increasing the rectifier delay angle more than 90 degrees. A negative voltage is applied to the ON thyristors and the current decreases to zero to turn off the inverter thyristors. An auxiliary thyristor with a chopping operation can improve commutation ability because current flows through the

thyristor at the reverse voltage interval. The simulation result is described in Fig. 54 from PSIM.
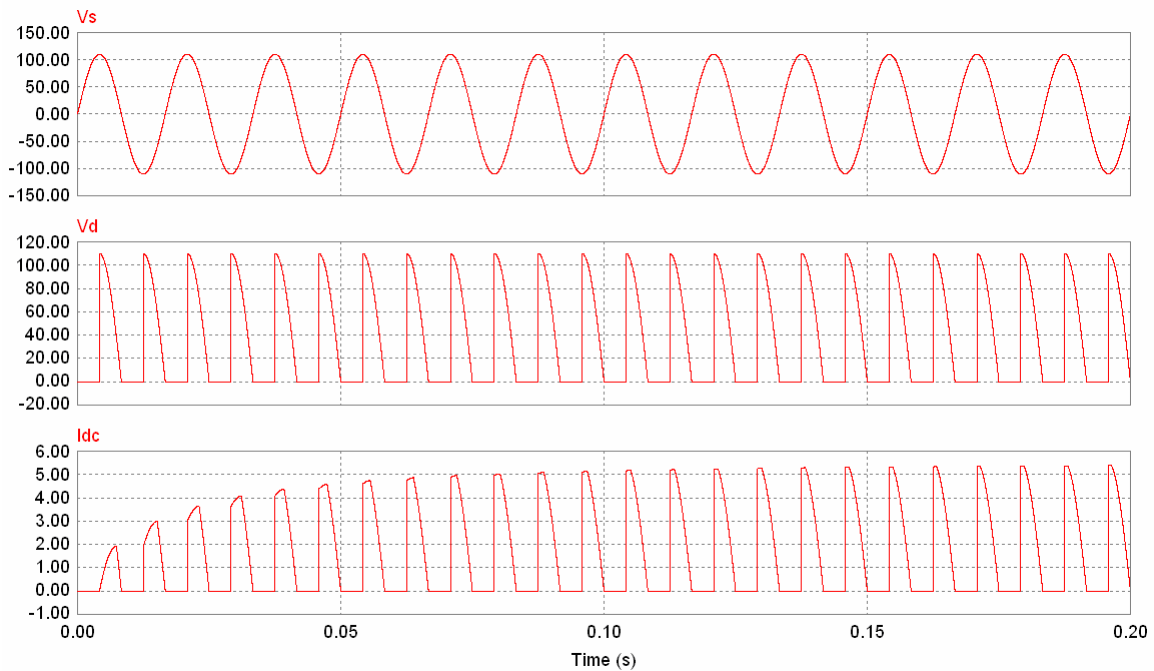
Fig. 54   DC link output voltage and current waveforms with the auxiliary thyristor.

From top to bottom : (a) single phase AC input voltage (b) DC link voltage

(c) DC link current

A thyristor is connected anti-parallel to the DC link inductance where a trigger signal arrives during the off time. Therefore, an auxiliary thyristor with a chopping operation can improve commutation ability. When the switching frequency of the rectifier is 60Hz, the DC link current is 5A and the turn off time of the thyristor is decreased. This is an ideal case for increasing the inverter switching frequency and operating it at a higher current.

CHAPTER VI

VOLTAGE BASED DIRECT POWER CONTROL FOR THE

CURRENT-FED DRIVE

6.1. Direct Power Control for the Current-fed Drive

The DC link voltage-based direct power control (V-DPC) is proposed in order to control the output power directly in the current-fed drive. In current-fed drives, voltage vectors are used for output power control and the DC link voltage can be used as the reference command for controlling the power. The goal of the direct power control is to maintain the output DC link voltage at the required output power operating point [54]. The V-DPC has advantages such as a simple algorithm for fixed switching frequency and good dynamic response for the current-fed drive. However, the DC link voltage feedback should be avoided at the moment of switching because the DC link voltage ripple causes a high number of errors from the DC link voltage feedback signal [55]-[59]. In this research, current-fed drive based on V-DPC is simulated which applied to the actual system. In the d and q-axis reference frame, the d and q-axis voltage vectors can be represented by the stator voltage magnitude and the torque angle. The d and q-axis reference voltages

$$V_d = V_s \cos \delta = -X_q I_q + E_i \qquad V_q = V_s \sin \delta = X_d I_d \qquad (6.1)$$

$$I_d = \frac{V_s \sin \delta}{X_d} \qquad I_q = \frac{E_i - V_s \cos \delta}{X_q} \qquad (6.2)$$

$$I_s \cos \theta = I_d \cos \delta + I_q \sin \delta \qquad (6.3)$$

where

δ : torque angle

θ : power factor angle

E_i : back-EMF

X_d, X_q : d and q-axis reactances

The output power equation is given by

$$
\begin{aligned}
P &= V_s I_s \cos\theta = V_s (I_d \cos\delta + I_q \sin\delta) \\
&= \frac{V_s^2 \sin\delta \cos\delta}{X_d} + \frac{E_i V_s \sin\delta - V_s^2 \sin\delta \cos\delta}{X_q} \\
&= \frac{E_i V_s \sin\delta}{X_q} + V_s^2 \sin\delta \cos\delta \left(\frac{1}{X_d} - \frac{1}{X_q} \right) \\
&= \frac{E_i V_s \sin\delta}{X_q} + \frac{V_s^2}{2} \sin 2\delta \left(\frac{X_q - X_d}{X_d X_q} \right)
\end{aligned}
\tag{6.4}
$$

From the output power equation, the torque angle at extracted power operating point can

be calculated for the maximum power per voltage (MPPV) using $\dfrac{dP}{dt} = 0$ [60]-[62].

$$
\frac{E_i V_s}{X_q} \cdot \frac{d}{dt} \sin\delta + \frac{V_s^2}{2} \left(\frac{X_q - X_d}{X_d X_q} \right) \cdot \frac{d}{dt} \sin 2\delta = 0
\tag{6.5}
$$

$$
\frac{E_i V_s}{X_q} \cos\delta + V_s^2 \left(\frac{X_q - X_d}{X_d X_q} \right) \cdot \left(2\cos^2\delta - 1 \right) = 0
\tag{6.6}
$$

The torque angle for the MPPV can be delivered as

$$
\cos\delta = \frac{-E_i X_d \pm \sqrt{E_i^2 X_d^2 + 8 \cdot V_s^2 (X_q - X_d)^2}}{4 \cdot V_s (X_q - X_d)}
\tag{6.7}
$$

$$\delta = \cos^{-1}\left(\frac{-E_i X_d \pm \sqrt{E_i^2 X_d^2 + 8 \cdot V_s^2 (X_q - X_d)^2}}{4 \cdot V_s (X_q - X_d)} \right) \tag{6.8}$$

+ : motoring, - : generating

Fig. 55 shows the proposed block diagram of power estimation based on the DC link voltage for a 3kW generator system and Fig. 56 describes power control block. The estimated line voltages and DC link voltage are delivered to the power controller block. The power command is transferred to the maximum power per voltage control block and the amplitude of the voltage and torque angle produce the d and q-axis voltage vectors. The voltage vectors are compared to measured voltage vectors and the DC link current command is decided by the d and q-axis current vectors using

$$I_{dc}^* = \sqrt{I_d^{*2} + I_q^{*2}} \tag{6.9}$$

For three phase rectifier control, the alpha controller produces the DC link current command which can be transferred to the alpha angle by a proper gain.

In the single-phase load commutated inverter with the series R-L load, line capacitance is used for the phase shift and the real and reactive components of the load current are given by:

$$I_P = I_L \cdot \cos\beta = \frac{V_L}{R} \quad I_Q = I_L \cdot \sin\beta = \frac{V_L}{X_c} \tag{6.10}$$

where

$$X_c = j\omega L \parallel \frac{1}{j\omega C} \tag{6.11}$$

through some algebraic manipulation,

$$I_L = \frac{2\sqrt{2} \cdot V_L{}^2}{\pi R V_d} \qquad V_L = \frac{\pi}{\sqrt{8}} V_d \frac{\sqrt{R^2 + X_c{}^2}}{X_c} \qquad (6.12)$$

From the above equation, we can calculate the commutation angle beta at a given

load voltage and current condition. The switching frequency of the single phase output is

fixed to 60Hz and the beta angle is given by $I_L{}^*$ with the proper gain.
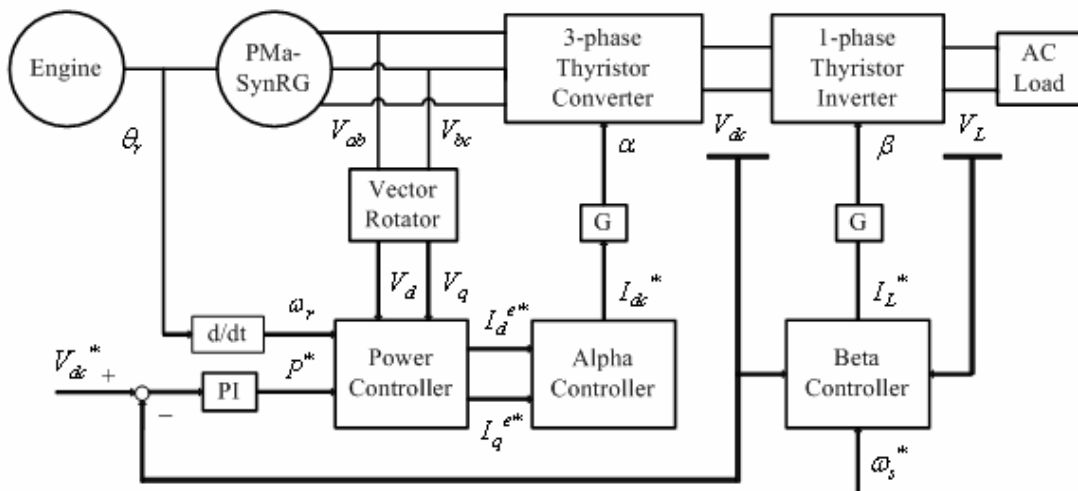
Fig. 55   Block diagram of the overall control system.
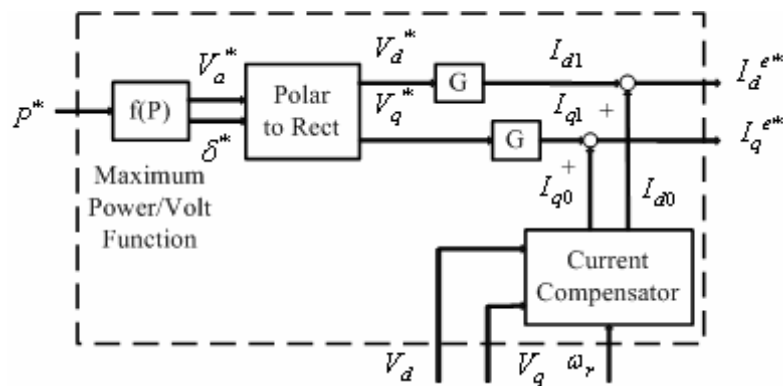
Fig. 56   Block diagram of power controller.

6.2. Simulation Results of the Direct Power Control System

For the verification of voltage oriented direct power control with current-fed drive, the three-phase rectifier with alpha controller and the single phase inverter with beta controller have been simulated using PSIM. The control system for 3kW output power is shown in Fig. 57. In this control system, the DC link voltage is detected for the out power command and it is delivered to commands of phase voltage and the torque angle delta by the PMa-SynRG power equations. From the measured three-phase line voltages, d and q-axis voltage vectors are compared by PI controllers. Two voltage vector commands are transferred to the DC link current command by the machine equations. The alpha angle is decided by the DC link current command with a PI controller.
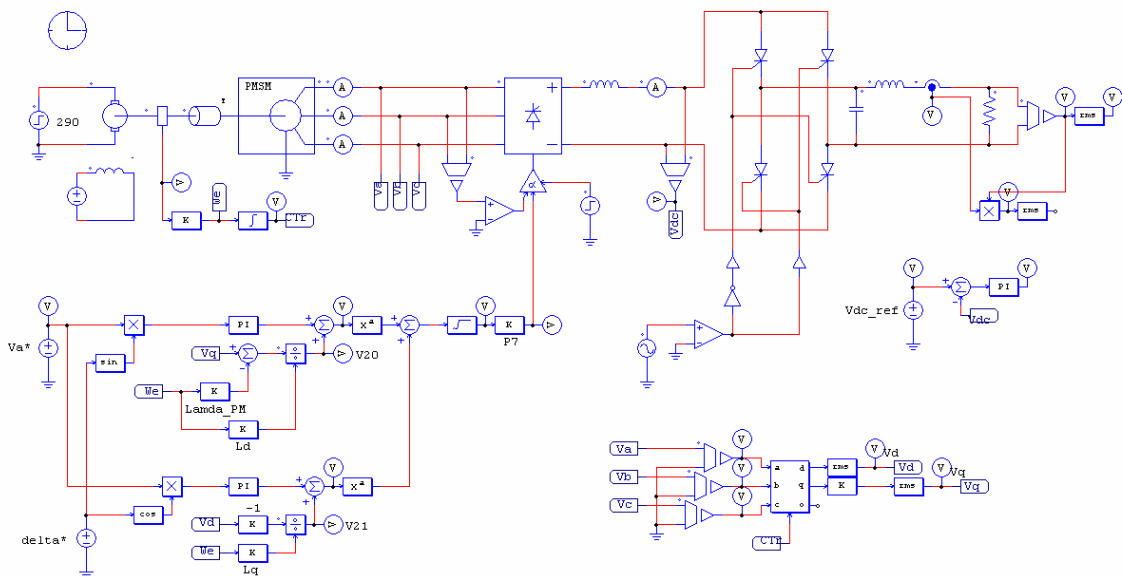
Fig. 57   Schematic of voltage based direct power control for current-fed drive.

Figs. 58 and 59 show simulation results of 3kW output power control for the current-fed drive. As speed reaches a steady state condition (3,600rpm), the DC link voltage reaches 120V by the alpha angle control of the three-phase rectifier. For 3kW output power, the amplitude of the voltage command is 75V and the torque angle command is 123^0.
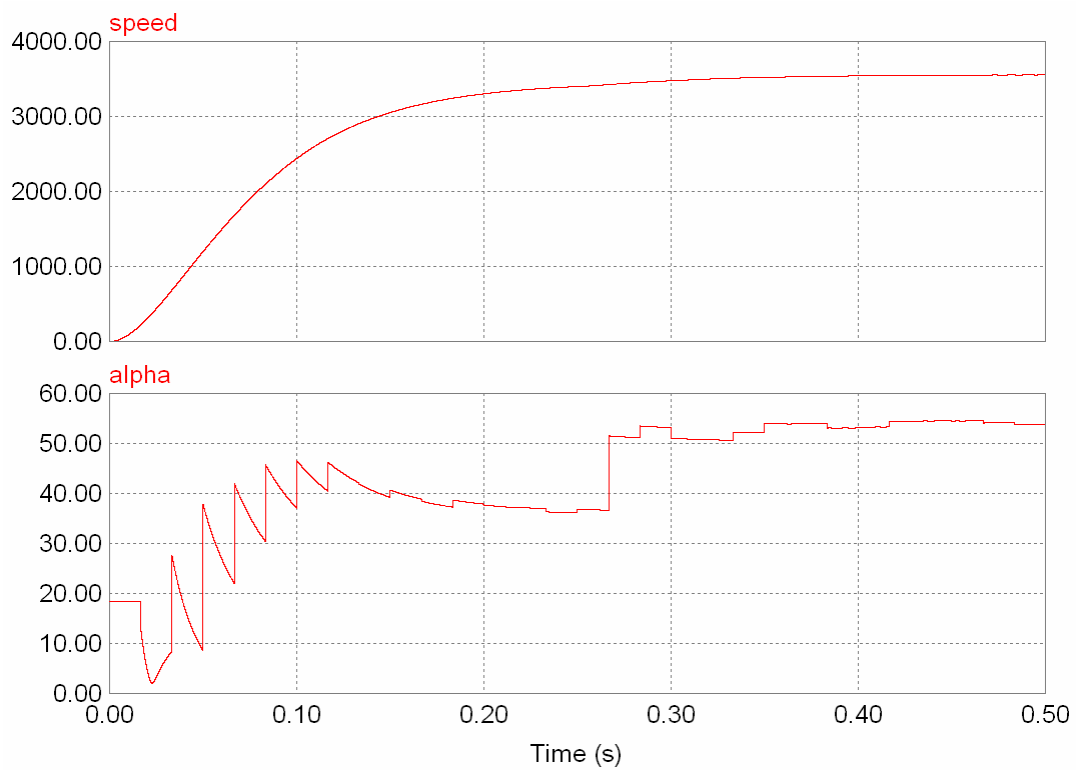
Fig. 58   Generator speed and alpha control angle for the three phase rectifier.
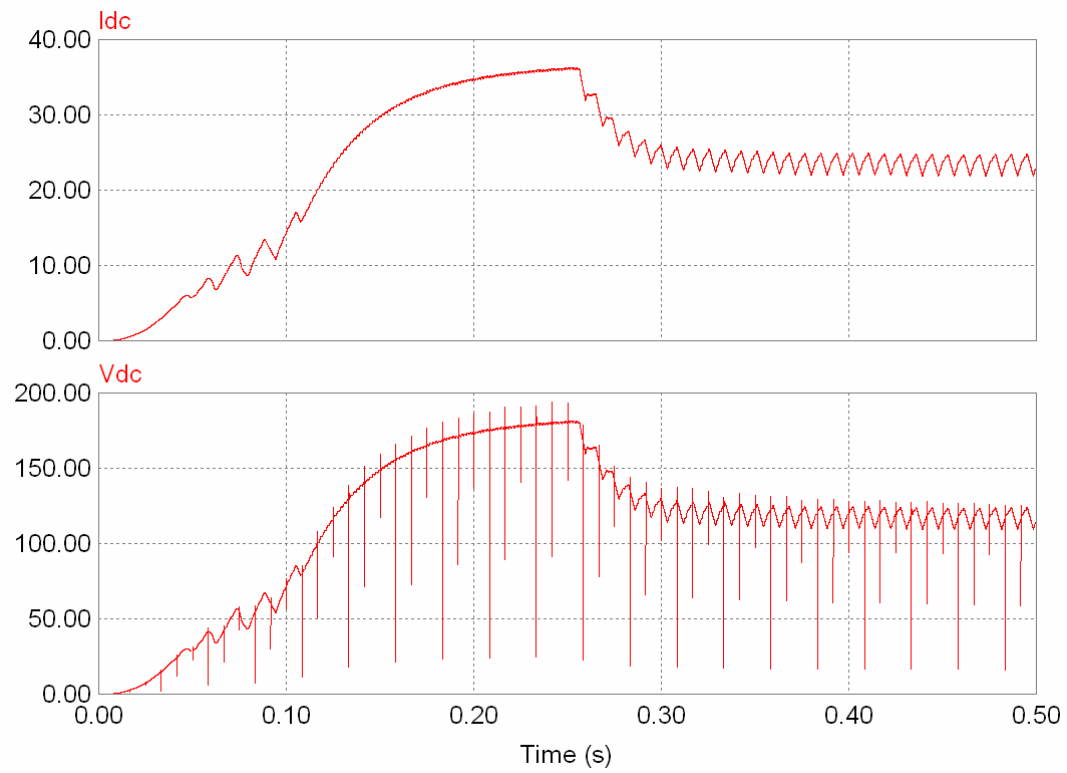
Fig. 59   DC link current and voltage waveforms.

From the amplitude of voltage command and torque angle, d and q-axis voltage vectors are decided for the 3kW output power. Simulations results are shown in Fig. 60.
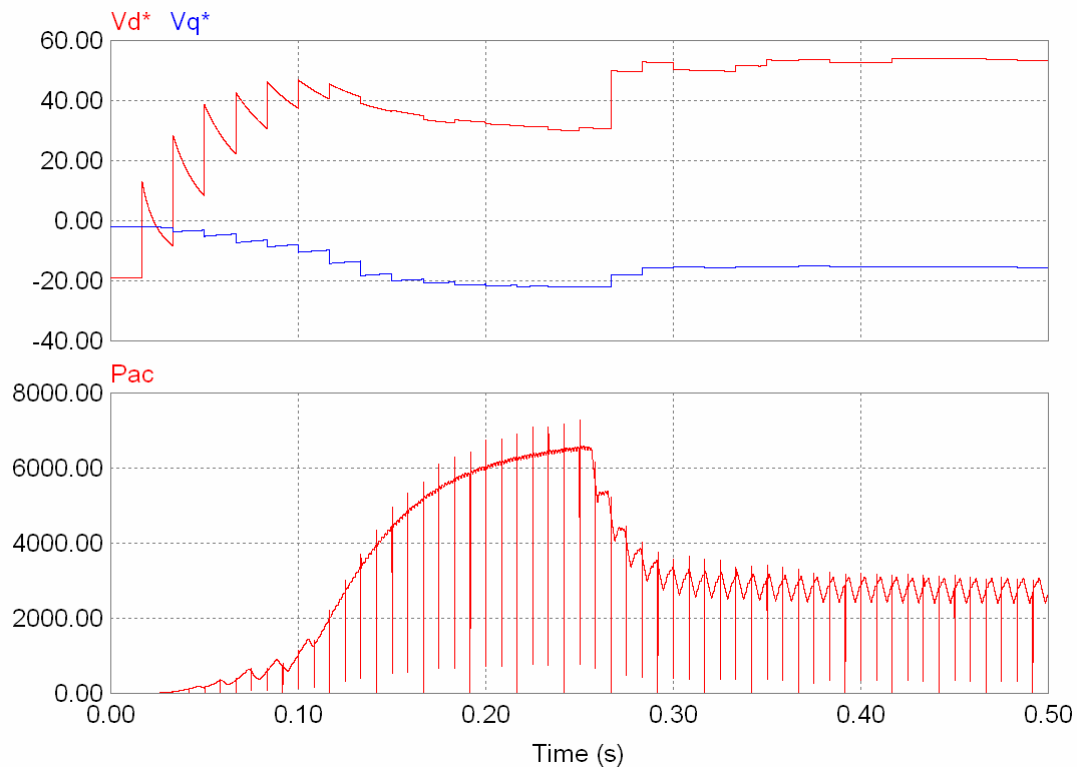
Fig. 60   d and q-axis voltage vectors and single phase output power.

Using the single-phase current-fed inverter and the accompanying low pass filter, the system can deliver the required sinusoidal 60Hz, 120V single-phase output. The simulation results are shown in Fig. 61. The waveform of the single phase output is not sinusoidal as much as a voltage-fed inverter because, in the current-fed, drive fast PWM switching for sinusoidal output is not used. Therefore, the THD value is much higher than the voltage-fed drive but the current-fed drive has lower switching losses and is more robust than the voltage-fed drive.
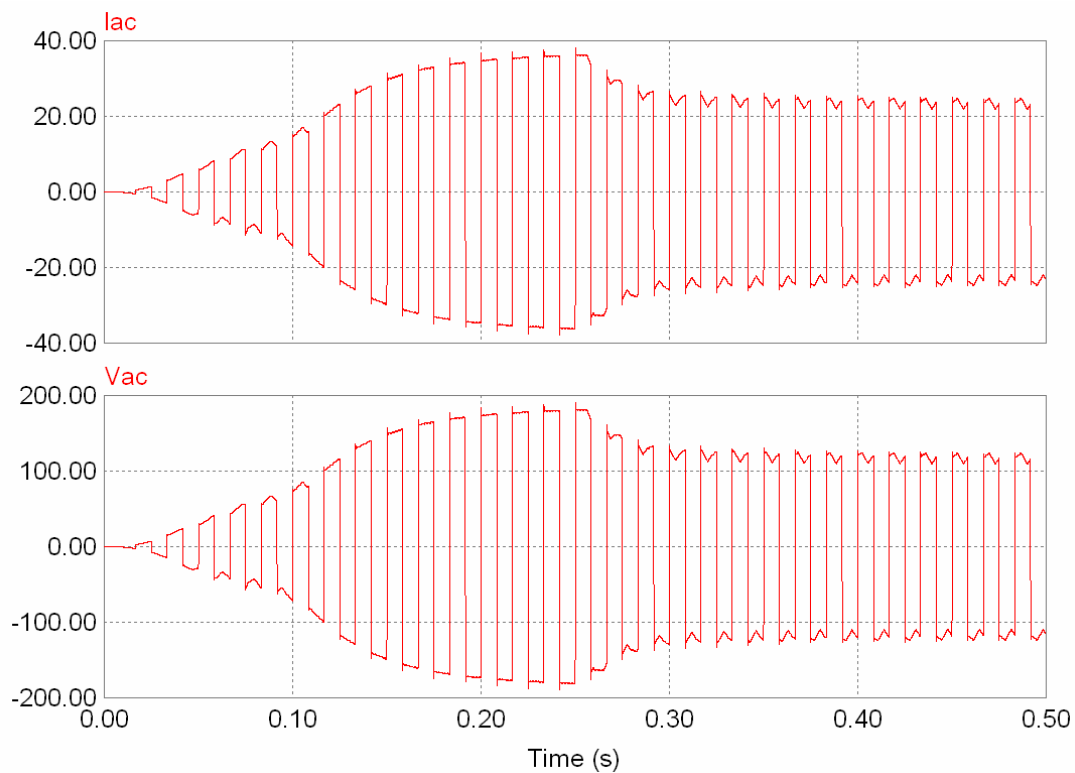
Fig. 61   Single phase AC output current and voltage waveforms.

6.3.   Experimental Results of the Direct Power Control System

Fig. 62 shows the block diagram for the current-fed drive and the 3kW PMa-SynRG test bed and Figs. 63, 64 are picture of the experimental setup. In the current-fed drive, four voltage sensors are used for voltage based direct power control. Three voltage sensors detect line-to-line voltages which are transferred to d, q axis voltage vectors for comparison to the output power command. The fourth sensor is the DC link voltage sensor which detects the DC link output voltage; this feedback signal is used for the output power command. These voltage sensor signals are connected to the interface board in order to realize the voltage based direct power control algorithm and sense the zero

crossing detection. In order to detect the starting point of the rectifier switching, the zero

crossing technique is applied to the current-fed drive.
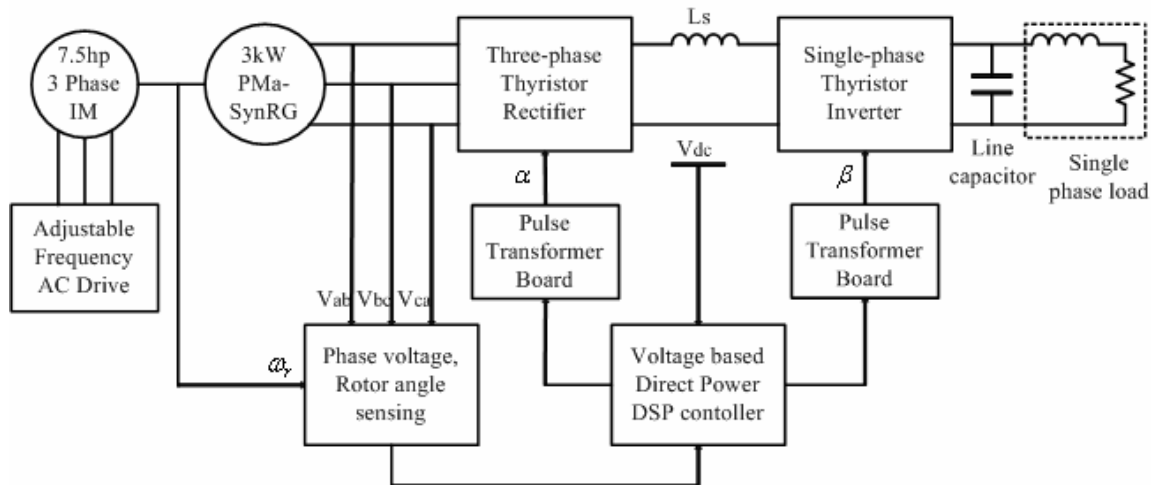
Fig. 62   Block diagram of the current-fed drive system.
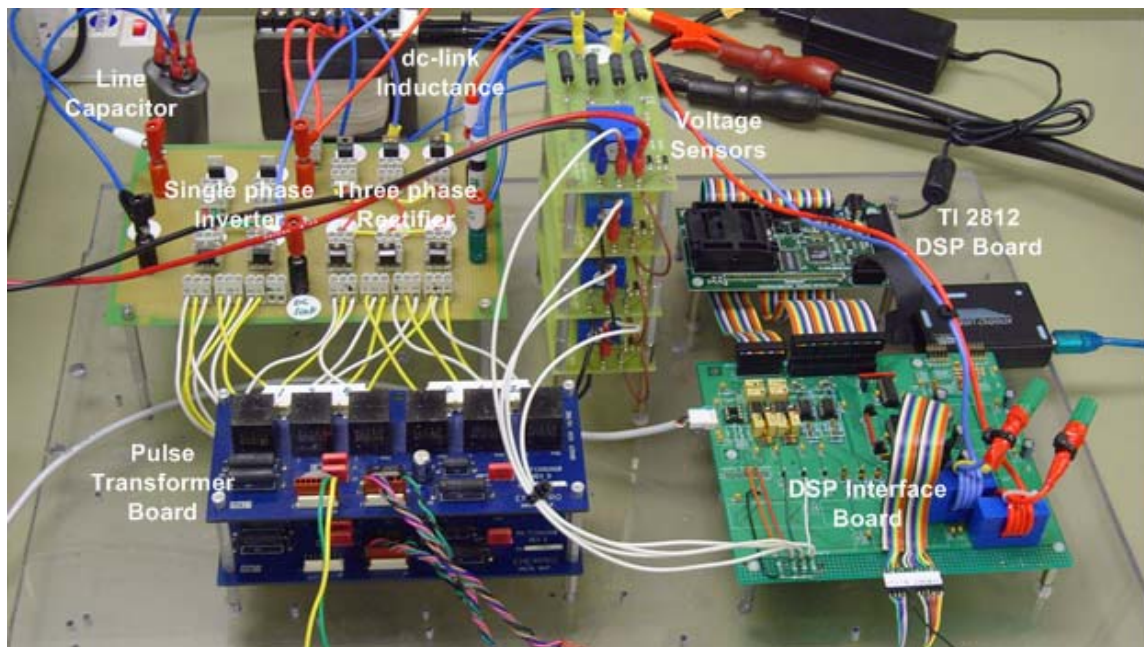
Fig. 63   Experimental setup for the current-fed drive.
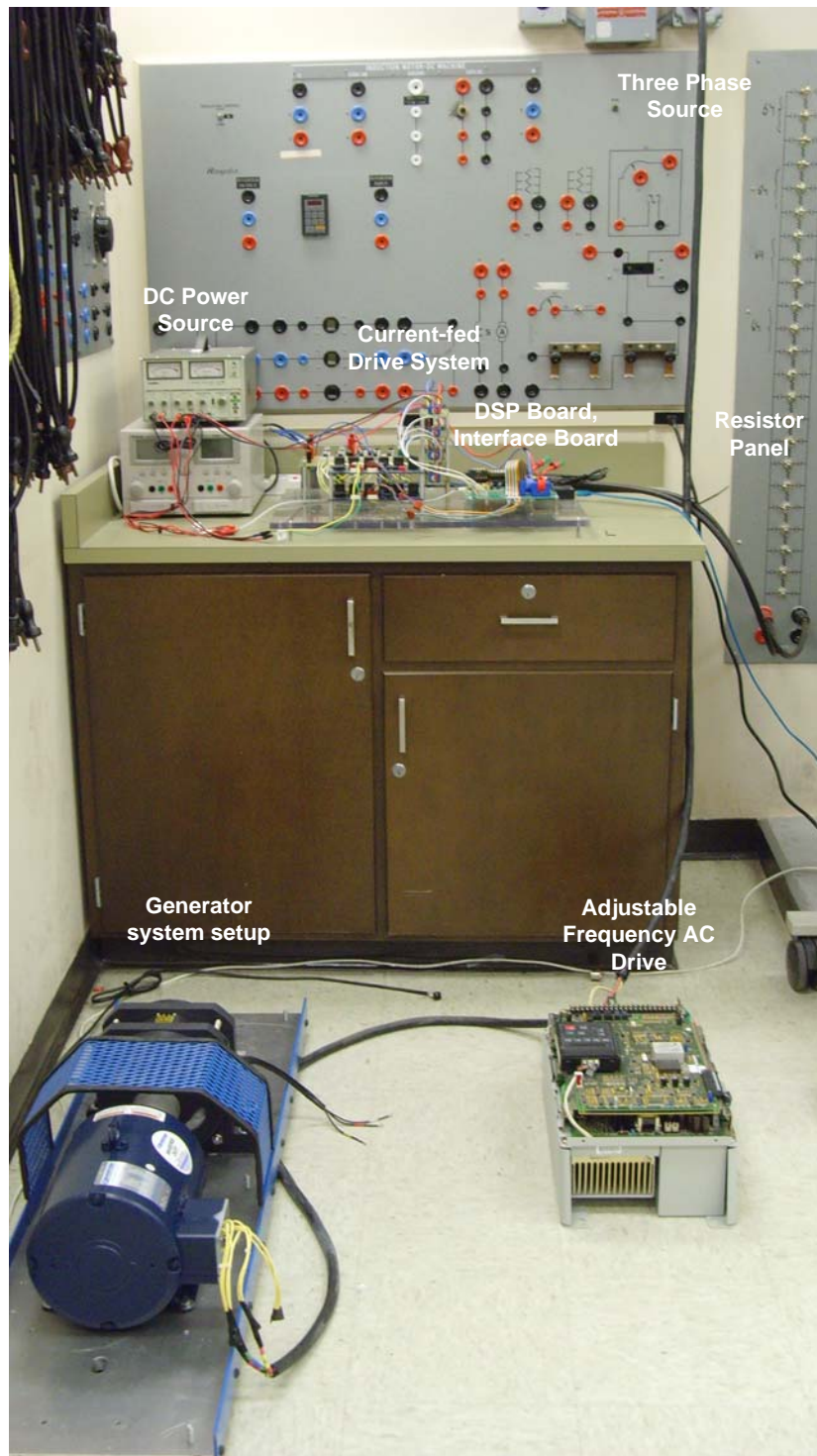
Fig. 64   Overall experimental setup.

The experimental setup was fabricated based on the block diagram of the current-fed drive. In order to realize the voltage-based direct power control, four voltage sensors are connected to the DSP interface board. The TI2812 DSP board produces gate signals to the three phase rectifier and the single phase inverter through the pulse transformer board which applies the turn on signal to thyristors and isolates the DSP board from thyristors for circuit protection.

In the DC link, a 58mH inductor is connected between the three phase rectifier and the single phase inverter in series and a 5uF line capacitor is used for the force commutation of the single phase inverter. A 10mH inductor and a 10 ohm resistor bank provided by a resistor panel are used for the single phase inductive load,.

6.3.1. Three-Phase Rectifier with Zero Alpha

From the 3kW PMa-SynRG, three phase voltages and currents are generated and the three phase input power converted to DC power by the three phase thyristor rectifier. The DC link inductance is connected between the three-phase thyristor rectifier and the single-phase inverter in order to reduce the DC link current ripple. In the experiment, the DC link inductance is 58mH and the internal resistance is $0.48\,\Omega$ to minimize the DC link voltage drop.

In the case of the alpha=0 control, the switching sequence of the three-phase rectifier starts at Vac zero. For the starting point of the switching sequence, the zero-crossing point of the phase AC line-to-line voltage is detected. From the zero-crossing point, thyristor T1 conducted during 60°.

Fig. 65 shows the experimental waveforms of the input phase voltage and the three-phase rectifier switching sequence. In the steady-state, the PMa-SynRG has eight poles and rotates at 3,600rpm. Therefore, the switching frequency of the three-phase rectifier is 240Hz.
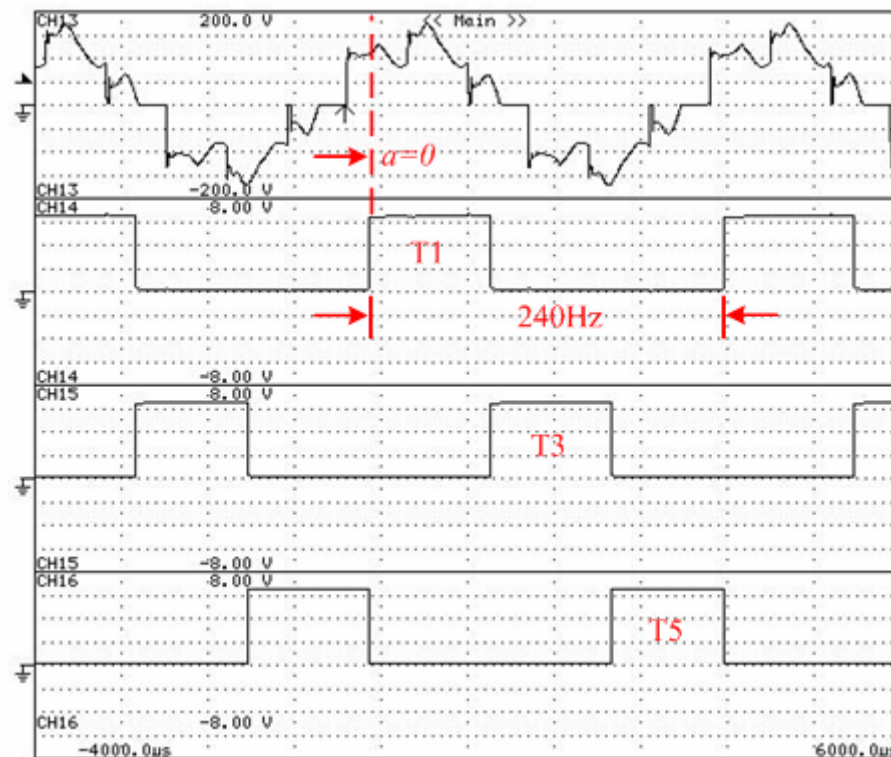
Fig. 65   Experimental waveforms of the input voltage and switching sequence.

From top to bottom : (a) line-to-line phase voltage Vab (50V/div) (b) switching signal

for T1(2V/div) (c) switching signal for T3 (2V/div) (d) switching signal for T5 (2V/div)

From the three-phase rectifier, the three-phase input power of the PMa-SynRG transferred to the DC link at alpha is zero. In this case the three-phase thyristor rectifier

operates as a diode rectifier and the DC link output voltage is 125V and the DC link current is 27A at load condition. Therefore, maximum DC link output power that can be achieved from the PMa-SynRG is 3,375W. Fig. 66 shows that the experimental waveforms of the DC link output voltage and current at alpha was zero.

Fig. 66   Experimental waveforms of the DC link voltage and current at zero alpha.

From top to bottom : (a) DC link voltage (50V/div) (b) DC link current (10V/div)

6.3.2.   Three-Phase Rectifier with Alpha Control

In order to control the output power, the three-phase thyristor rectifier can control the DC link output voltage and current with the control angle alpha. In this research, the

control angle alpha is decided by DC link voltage command feedback converted to the

output voltage command. Using direct power control blocks, PI controller can decide the

DC link current command. With the three-phase thyristor rectifier control angle alpha,

the DC link voltage is reduced from 125V to 120V for the single phase output voltage.

Fig. 67 shows the experimental results using control angle alpha with direct power

control.
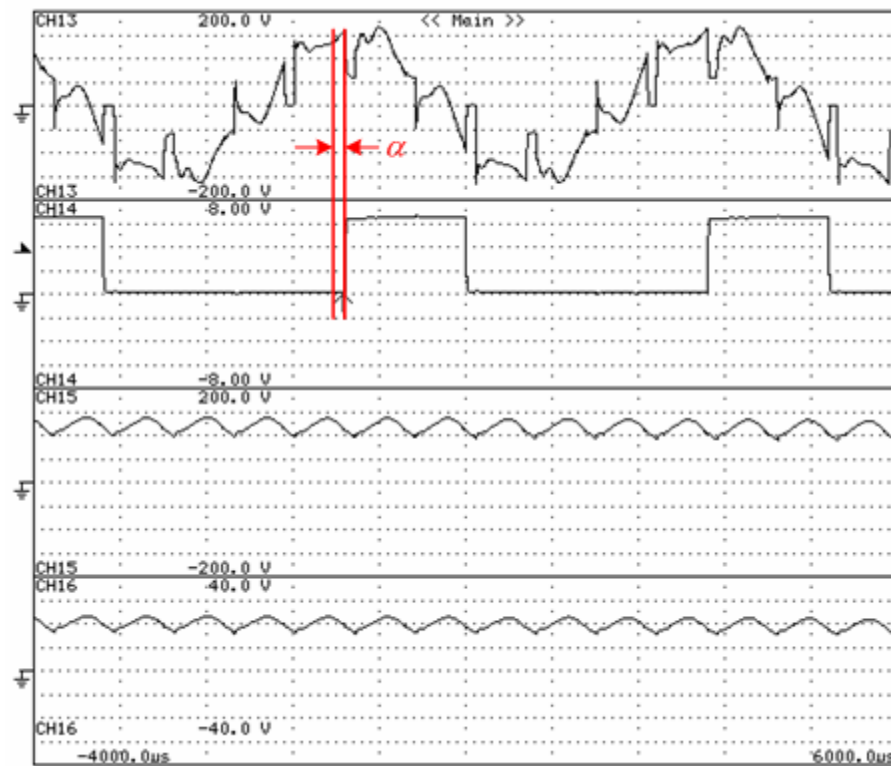
Fig. 67   Experimental waveforms of the DC link voltage and current with alpha control.

From top to bottom : (a) line-to-line phase voltage Vab (50V/div) (b) three-phase

rectifier gate signal (2V/div) (c) DC link voltage (50V/div) (d) DC link current

(10A/div)

As the control angle alpha is increased by the DC link power command, the DC link voltage is regulated to 120V and the DC link current decreases from 27A to 20A. Therefore, the DC link output power is decreased to 2,400W.

6.3.3. Single-Phase Forced-Commutated Inverter

The three-phase rectifier converts three-phase input power to DC power using the direct power control block. The produced DC link voltage and current needs to be inverted to the single phase output power. In order to supply 120V/60Hz output power, the single-phase thyristor based inverter is applied. Fig. 68 shows the switching sequence of the three-phase rectifier and single-phase inverter. The switching frequency of the single-phase inverter is 60Hz and the thyristor S1 is synchronized to the three-phase rectifier thyristor T1.

When the single-phase inverter operates, the DC link voltage has a big ripple because of the inverter switching. However, it does not affect the single phase output voltage and current because it changes to AC output. Fig. 69 shows the experimental waveforms that occur when the single-phase inverter operates at the three-phase rectifier control angle alpha zero. The single-phase AC output voltage has 125V peak and the current is 30A peak.
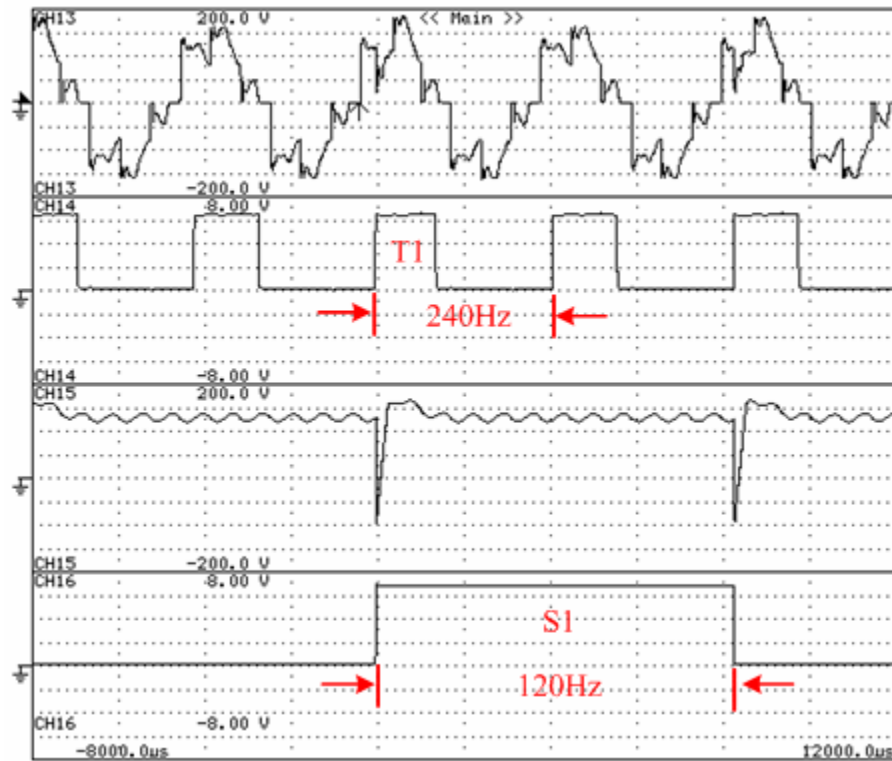
Fig. 68   Experimental waveforms of the phase voltage and gate signals.

From top to bottom : (a) line-to-line phase voltage Vab (50V/div) (b) three-phase

rectifier gate signal (2V/div) (c) DC link voltage (50V/div) (d) single-phase inverter gate

signal (2V/div)
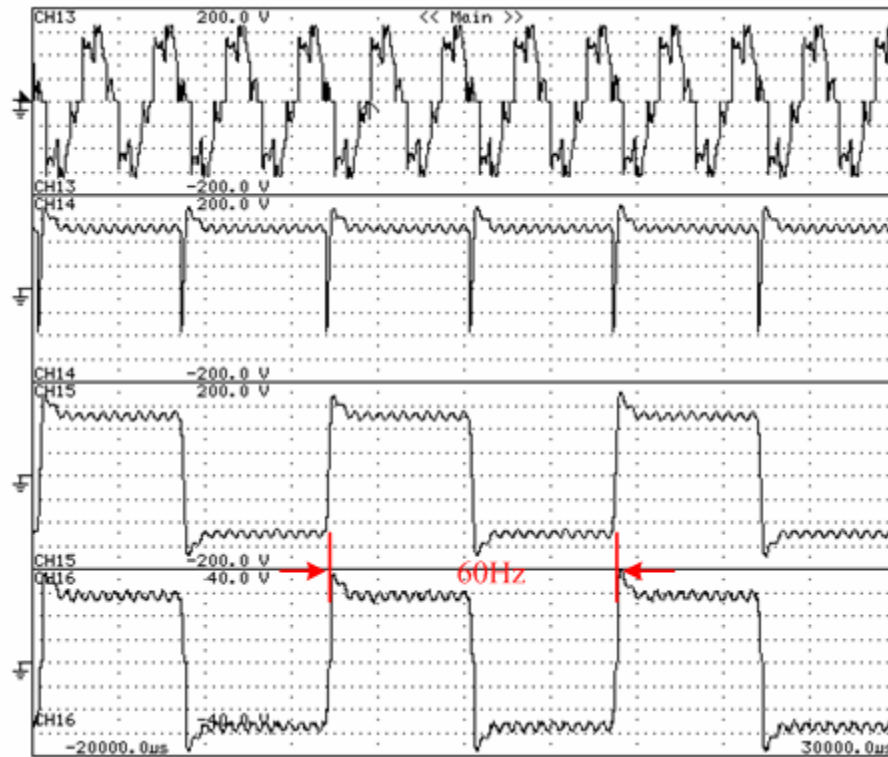
Fig. 69   Experimental waveforms of single-phase output with alpha control.

From top to bottom : (a) line-to-line phase voltage Vab (50V/div) (b) DC link voltage

(50V/div) (c) single-phase AC output voltage (50V/div) (d) single-phase AC output

current (10A/div)

In order to commutate thyristors in the single-phase inverter, a line capacitor is used in the single-phase load for the forced commutation. In the experiment, a 5uF line capacitor is applied for the leading power factor and a 45mH inductor is used to test the inductive load condition. Fig. 70 shows the experimental output currents of the inverter output current, load current and the current through line capacitor.
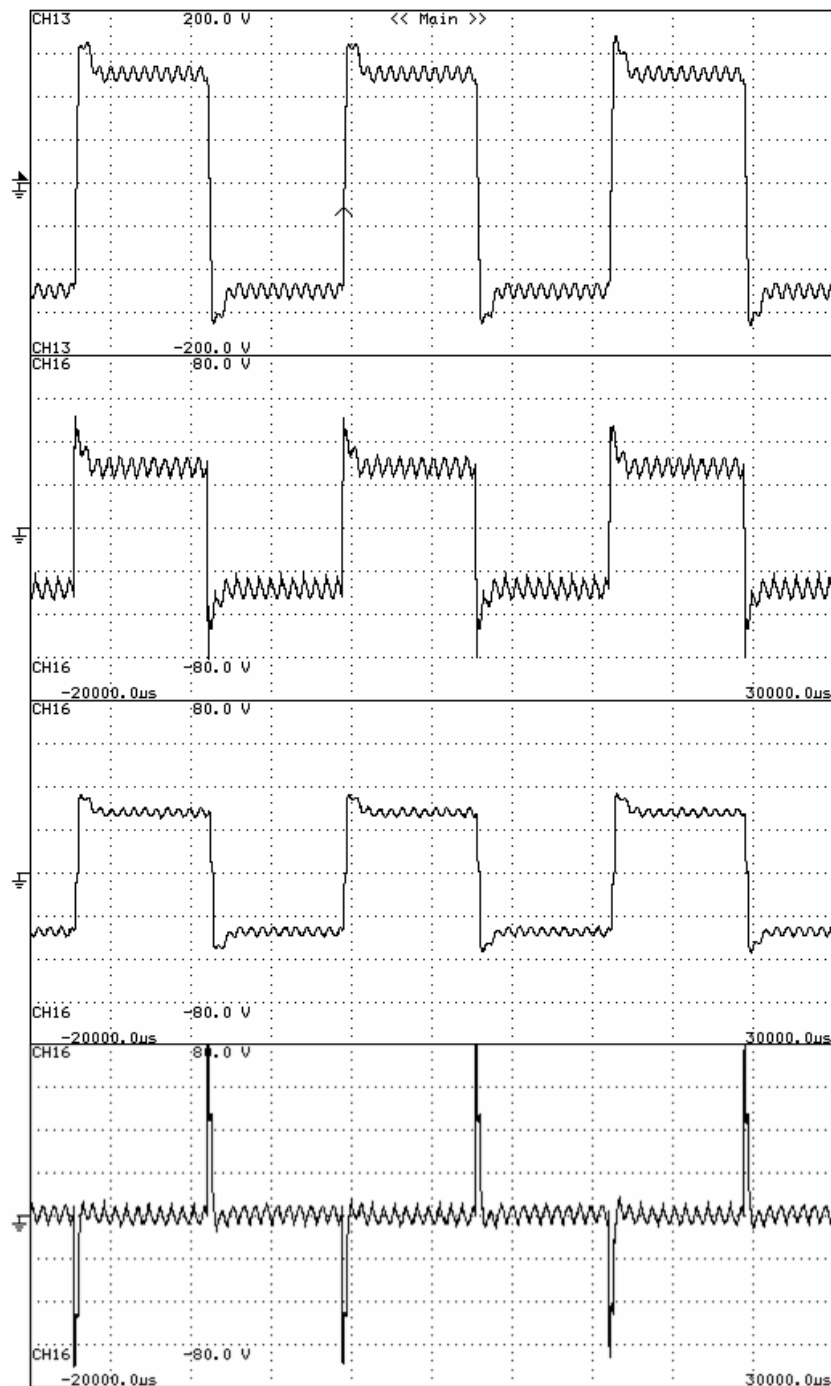
Fig. 70   Experimental waveforms of output currents.

From top to bottom : (a) single-phase output voltage (50V/div) (b) inverter output

current (20A/div) (c) load current (20A /div) (d) line capacitor current (20A /div)

6.3.4. Direct Power Control at Transient Condition

When the PMa-SynRG speeds up from zero to 3,600rpm, the switching frequency of the three-phase rectifier needs to be synchronized to generator speed and the PI controller gains of the direct power control block has to be recalculated during the transient condition. In this case, the direct power controller is not stable and the DC link output voltage and current has a big ripple. Fig. 71 shows the experimental result in the transient condition.
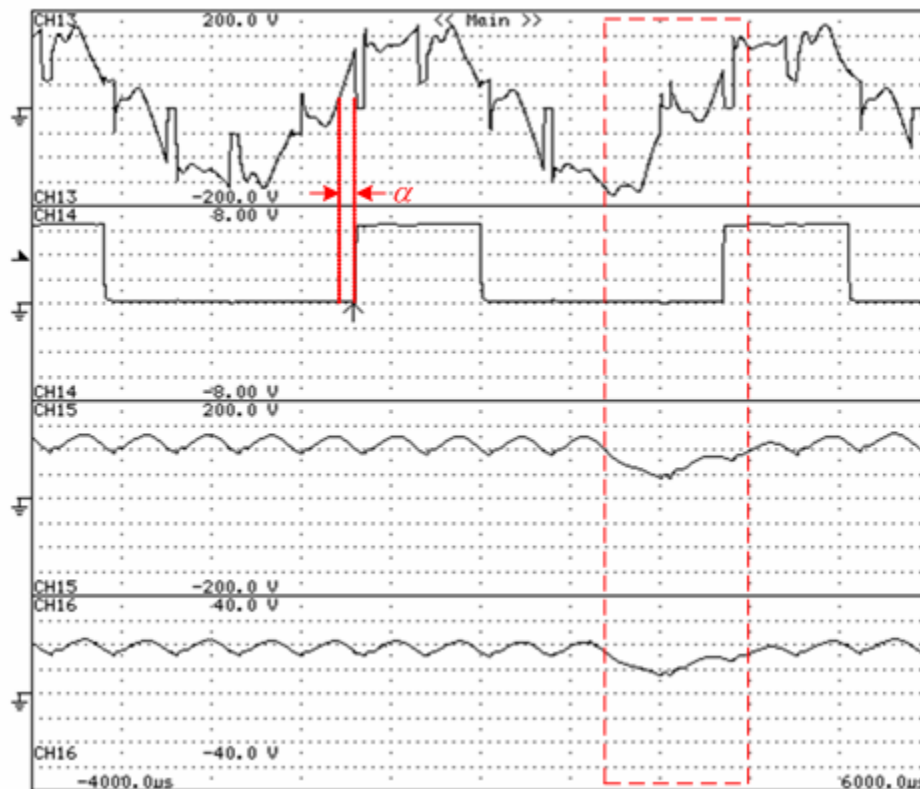
Fig. 71 Experimental waveforms of DC link output at transient condition.
From top to bottom : (a) line-to-line phase voltage Vac (50V/div) (b) three-phase rectifier gate signal (2V/div) (c) DC link voltage (50V/div) (d) DC link current (10A/div)

The ripple from the DC link voltage and current affects the single-phase AC output. Fig. 72 dictates the unstable output waveforms. For stable control in the transient condition, generator parameters and control gains need to be recalculated as real time with a more complex algorithm. Therefore, a constant control angle alpha for the three-phase rectifier is applied during the starting in this research.

Fig. 72   Experimental waveforms of single-phase output at transient condition.
From top to bottom : (a) DC link voltage (50V/div) (b) single-phase output voltage
(50V/div) (c) single-phase output current (10A/div)

6.3.5. Direct Power Control at Steady-State Condition

When the generator speed reaches 3,600rpm after 10 seconds, the direct power controller starts operating the three-phase rectifier. In the steady-state condition, the control angle alpha is decreased from the constant alpha in the transient condition, respectively. Figs. 73 and 74 show stable DC link output voltage and current and single-phase AC outputs.
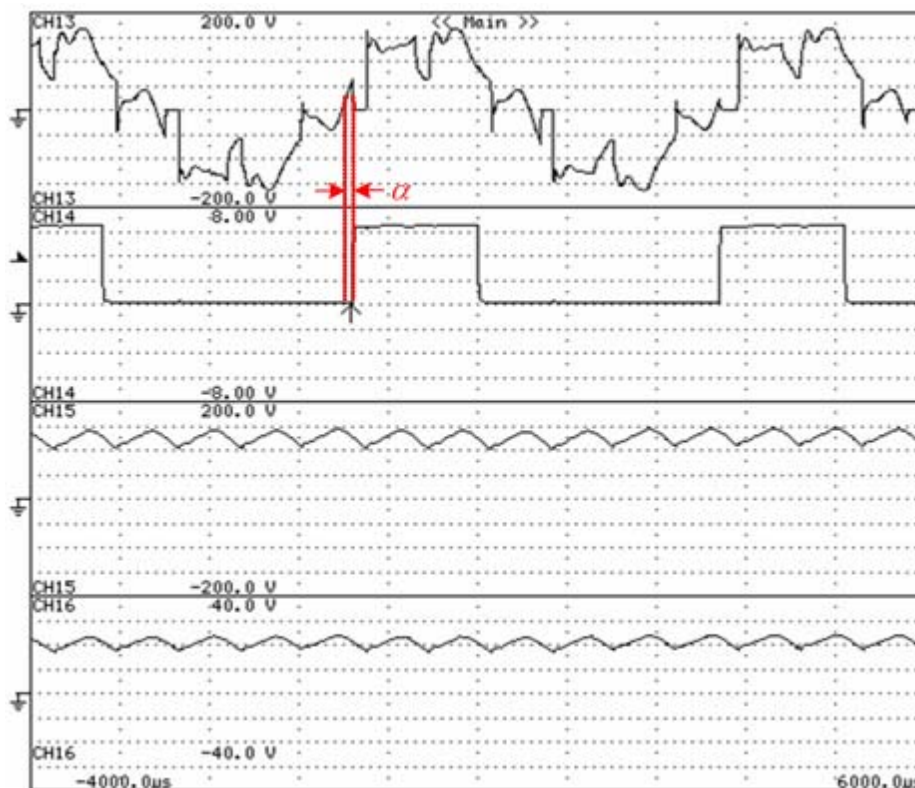
Fig. 73 Experimental waveforms of DC link output at steady-state condition.

From top to bottom : (a) line-to-line phase voltage Vac (50V/div) (b) three-phase

rectifier gate signal (2V/div) (c) DC link voltage (50V/div) (d) DC link current
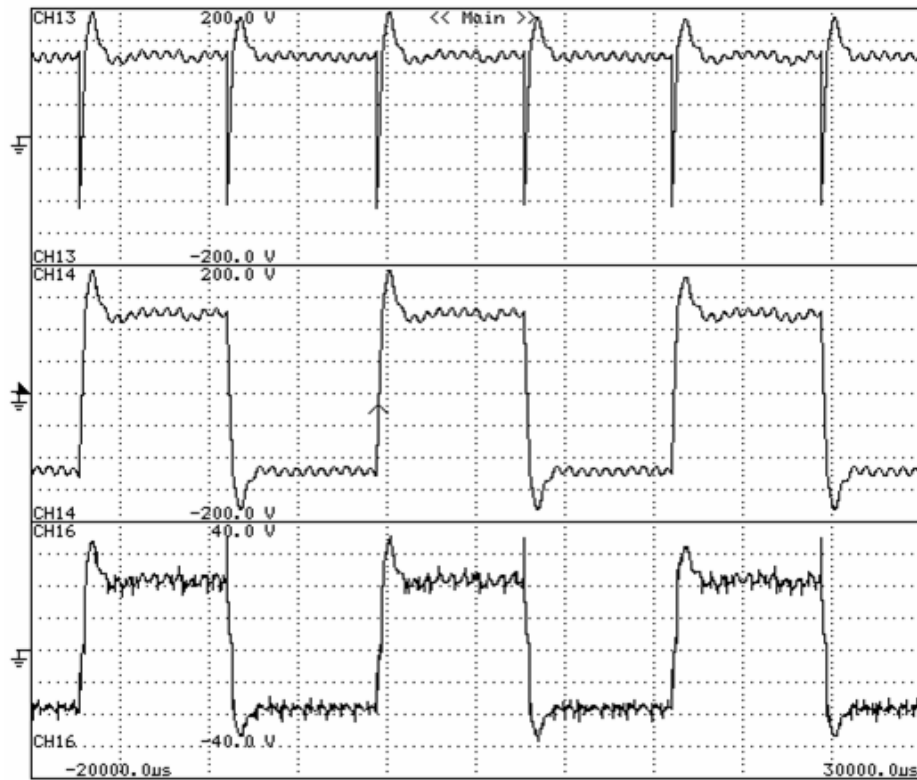
(10A/div)

Fig. 74   Experimental waveforms of single-phase output at steady-state condition.

From top to bottom : (a) DC link voltage (50V/div) (b) single-phase output voltage

(50V/div) (c) single-phase output current (10A/div)

CHAPTER VII

CONCLUSIONS AND FUTURE WORK

7.1. Conclusions

This dissertation has investigated the optimal design process of PMa-SynRG for different stator winding configurations and thyristor based current-fed drives for generator control. Based on the developed optimal design process, this work has designed a 3kW optimized PMa-SynRG and proposed a new converter topology and control algorithm to improve generator performance.

Various machine types for generator applications and converter topologies are presented in Chapter I. The most robust and low cost generator system by PMa-SynRG and thyristor based current fed drive is introduced. Advantages and drawbacks of each machine type and converter topologies have been reviewed. Dissertation outlines and research objectives are included.

Chapter II presents an analytical model using equivalent magnetic circuits for the PMa-SynRG. In order to develop the optimal design process, the lumped parameter model is applied. LPM provides a fast means for analyzing the electromagnetic characteristics of PMa-SynRG. Linear LPM and the nonlinear LPM are programmed using MATLAB so all the machine parameters are calculated very quickly. For the generator operating capability calculation, machine losses have been presented.

In order to find an optimized design for PMa-SynRG, an optimal design process using DES and FEA is developed in Chaper III. The proposed design process can deliver

an optimized design using LPM, DES backed by FEA after several iterations. The proposed concentrated winding PMa-SynRG can achieve better efficiency and lower cost than the distributed winding machine because copper and magnet volume can be reduced. With respect to output performance, the maximum generated power is designed to be equal for each winding configuration with wide CPSR. However, the output torque ripple and cogging torque are improved using multiple poles for the concentrated winding machine. Simulation results and comparisons of each optimal design results and winding configurations have been included.

The fabricated 3kW PMa-SynRG for portable military application has been presented in Chapter IV. In order to verify performance of the designed PMa-SynRG test setup, simulation and experimental results have been compared.

In Chapter V, a new converter topology for a current-fed drive has been proposed which utilizes a thyristor based three-phase rectifier to convert generator power to DC link power and a single-phase forced commutated inverter to supply single- phase inductive load with a line capacitor. The proposed topology is much simpler than other forced commutation methods such as an auto-sequential circuit. Thus, it reduces the cost of the power electronic hardware. The simulation results of each topology are compared.

A new control algorithm for current-fed drive has been developed in Chapter VI. A DC link voltage-based direct power control is proposed in order to control the output power directly in the current-fed drive,. The goal of the direct power control is to maintain the output DC link voltage at the required output power operating point. The direct power control has advantages such as a simple algorithm for fixed switching

frequency and good dynamic response for the current-fed drive. The simulation and experimental results have verified the developed control algorithm.

7.2. Future Work

Future investigation for the current-fed drive would continue to improve the single-phase voltage waveform. In phase II+, the output waveform from the current-fed drive has non-sinusoidal and it has low THD. To improve the output waveform, a new control topology would be developed for the single-phase inverter.

Based on the results of this research, the actual generator system using combustion engine as a prime mover could be continued. In the phase II+, the three-phase induction motor is applied instead of the engine and it runs with fixed speed. However, current and voltage-fed drives have been developed for the variable speed control. Therefore, constant power control for the high-speed range would be another research issue for the PMa-SynRG control system.

REFERENCES

[1]   J. Wai, and T. M. Jahns, "A new control technique for achieving wide constant power speed operation with an interior PM alternator machine," in *Conf. Rec. IEEE IAS Annu. Meeting*, vol. 2, pp. 807-814, Oct. 2001.

[2]   H. Murakami, Y. Honda, and H. Kiriyama, "The performance comparison of SPMSM, IPMSM and SynRM in use as air-conditioning compressor," in *Conf. Rec. IEEE IAS Annu. Meeting*, vol. 2, pp. 840-845, Oct. 1999.

[3]   H. Murakami, Y. Honda, H. Kiriyama, S. Morimoto, and Y. Takeda, "The performance comparison of SPMSM, IPMSM and SynRM in use as air-conditioning compressor," in *Conf. Rec. IEEE IAS Annu. Meeting*, vol. 2, pp. 840-845, Oct. 1999.

[4]   N. Bianchi, and S. Bolognani, "Interior PM synchronous motor for high performance applications," *Proc. PCC*, vol 1, pp. 148-153, Apr. 2002.

[5]   T. M. Jahns, "Uncontrolled generation of interior PM synchronous machines following high-speed inverter shutdown," in *Conf. Rec. IEEE IAS Annu. Meeting*, vol. 1, pp.395-404, 1998.

[6]   W. L. Soong, "Field-weakening performance of interior permanent magnet motors," *IEEE Trans. Ind. Appl.*, vol. 38, no. 5, pp. 1251-1258, Sept./Oct. 2002.

[7]   P. Niazi, "Permanent magnet assisted synchronous reluctance motor design and performance improvement," Ph.D. Dissertation, Texas A&M University, 2005.

[8]   S. Morimoto, M. Sanada, and Y. Takeda, "Performance of PM assisted synchronous reluctance motor for high efficiency and wide constant power operation," *IEEE Trans. Ind. Appl.*, vol. 37, no. 5, pp. 1234-1240, Sept./Oct. 2001.

[9]   P. Niazi, H. A. Toliyat, D-H. Cheong, and J-C. Kim, "A low-cost and efficient permanent magnet assisted synchronous reluctance motor drive," *IEEE Trans. Ind. Appl.*, vol. 43, no. 2, pp. 542-550, Mar./Apr. 2007.

[10] I. Boldea, L. Tutelea, and C. I. Pitic, "PM assisted reluctance synchronous motor/generator (PM-RSM) for mild hybrid vehicle: electromagnetic design," *IEEE Trans. Ind. App.*, vol. 40, no. 2, pp. 492-498, Mar./Apr. 2004.

[11] Y. Honda, T. Nakamura, T. Higaki, and Y. Takeda, "Motor design considerations and test results of an interior permanent magnet synchronous motor for electric vehicles," in *Conf. Rec. IEEE IAS Annu. Meeting*, vol. 1, pp. 75-82, Oct. 1997.

[12] T. Nakamura, S. Morimoto, M. Sanada, and Y. Takeda, "Optimum control of IPMSG for wind generation system," *Proc. PCC*, vol. 3, pp. 1435-1440, Apr. 2002.

[13] R. Q. Machado, J. A. Pomilio, and E. G. Marra "Electronically controlled bi-directional connection of induction generator with a single-phase grid," *Ind. Elec. Soc. IECON*, vol. 3, pp. 1982-1987, Nov./Dec. 2001.

[14] M. Chinchilla, S. Arnaltes, and J. C. Burgos, "Control of permanent-magnet generators applied to variable-speed wind-energy systems connected to the grid," *IEEE Trans. En. Conv.*, vol. 21, no. 1, pp. 130-135, Mar. 2006.

[15] M. S. Kwak, and S. K. Sul, "Control of an open-winding machine in a grid-connected distributed generator system," *IEEE Trans. Ind. Appl.*, vol. 44, no. 4, pp. 1259-1267, July/Aug. 2008.

[16] P. C. Krause, O. Wasynczuk, and S. D. Sudhoff, *Analysis of Electric Machinery and Drive Systems*. Piscataway, NJ: IEEE Press, 2002.

[17] H. L. Hess, D. M. Divan, and Y. Xue, "Modulation strategies for a new SCR-based induction motor drive system with a wide speed range," *IEEE Trans. Ind. Appl.*, vol. 30, no. 6, pp. 1648-1655, Nov./Dec. 1994.

[18] S. Nishikata, and T. Kataoka, "Dynamic control of a self-controlled synchronous motor drive system," *IEEE Trans. Ind. Appl.*, vol. 20, no. 3, pp. 568-604, May/June 1984.

[19] C. T. Rim, N. S. Choi, G. C. Cho, and G. H. Cho, "A complete DC and AC analysis of three-phase controlled-current PWM rectifier using circuit D-Q transformation," *IEEE Trans. Power Elec.*, vol. 9, no. 4, pp. 390-396, Mar. 2006.

[20]   J. R. Espinoza, and G. Joos, "A current-source-inverter-fed induction motor drive system with reduced losses," *IEEE Trans. Ind. Appl.*, vol. 34, no. 4, pp. 796-805, July/Aug. 1998.

[21]   R. Emery, and J. Eugene, "Harmonic losses in LCI-fed synchronous motors," *IEEE Trans. Ind. Appl.*, vol. 38, no. 4, pp. 948-954, July/Aug. 2002.

[22]   B. K. Bose, *Modern Power Electronics and AC Drives*, Upper Saddle River, NJ: Prentice Hall, 2002.

[23]   M. Mohan, T. M. Undeland, and W. P. Robbins, *Power Electronis: Converters, Applications, and Design*, Hoboken, NJ: John Wiley & Sons, 2002.

[24]   M. P. Kazmierkowski, R. Krishnan, and F. Blaabjerg, *Control in Power Electronics*, San Diego, CA: Academic Press, 2002.

[25]   E. C. Lovelace, T. M. Jahns, and J. H. Jeffrey "A saturating lumped-parameter model for an interior PM synchronous machine," *IEEE Trans. Ind. Appl.*, vol. 38, no. 3, pp. 645-650, May/June 2002.

[26]   E. C. Lovelace, "Optimization of a magnetically saturable interior PM synchronous machine drive," Ph.D. Dissertation, Massachusetts Institute of Technology, 2000.

[27]   E. C. Lovelace, T. M. Jahns, and J. Wai, "Design and experimental verification of a direct-drive interior PM synchronous machine using saturable lumped-parameter model," in *Conf. Rec. IEEE IAS Annu. Meeting*, vol. 4, pp. 2486 -2492, Dec. 2002.

[28]   J. H. Lee, J. C. Kim, and D. S. Hyun, "Effect analysis of magnet on Ld and Lq inductance of permanent magnet assisted synchronous reluctance motor using finite element method," *IEEE Trans. Magnetics*, vol. 35, no. 35, pp. 1199-1206, May 1999.

[29]   B. J. Chalmers, S. A. Hamed, and G. D. Baines, "Parameters and performance of a high-field performance permanent-magnet synchronous motor for variable-frequency operation," *Proc. IEE*, vol. 132, pt. B, pp. 117-124, 1985.

[30] A. Fratta, A. Vagati, and F. Villata, "Design criteria of an IPM machine suitable for field-weakening operation," in *Conf. Rec. IEEE ICEM,* vol. 1, pp 1059-1065.

[31] W. Soong, "Design and modeling of axially-laminated interior permanent magnet motor drives for field-weakening applications," Ph.D. Dissertation, University of Glasgow, 1993.

[32] E. C. Lovelace, and T. M. Jahns, "Impact of saturation and inverter cost on interior PM synchronous machine drive optimization," *IEEE Trans. Ind. Appl.*, vol. 36, no. 3, pp. 736-745, May/June 2000.

[33] B. A. Welchko, T. M. Jahns, and W. L. Soong, and J. M. Nagashima "IPM synchronous machine drive response to symmetrical and asymmetrical short circuit faults," *IEEE Trans. Ene. Conv.*, vol. 18, no. 2, pp. 291-298, June 2003.

[34] R. Storn, and K. Price, "Differential evolution – a simple and efficient adaptive scheme for global optimization over continuous spaces," *Tech. Report TR-95-012, ICSI*, Mar., 1995.

[35] J. Baek, "Shape optimization of AC servo motor using FEM and advanced evolution strategy," M.S. Thesis, Hong-Ik University, 1998.

[36] K. Deb, "Multi-objective optimization using evolutionary algorithms," West Sussex, Wiley, 2001.

[37] A. M. El-Refaie, and T. M. Jahns, "Optimal flux weakening in surface PM machines using concentrated windings," in *Conf. Rec. IEEE IAS Annu. Meeting*, vol. 2, pp. 1038-1047, Oct. 2004.

[38] J. Baek, M. M. Rahimian, and H. A. Toliyat, "Optimal design and comparison of stator winding configurations in permanent magnet assisted synchronous reluctance generator," in *Conf. Rec. IEEE IEMDC*, pp. 732-737, May 2009.

[39] T. J. E. Miller, *Brushless Permanent-Magnet and Reluctance Motor Drives*. Oxford: Clarendon Press, 1989.

[40] M. Yoneda, M. Shoji, Y. Kim, and H. Dohmeki, "Novel selection of the slot/pole ratio of the PMSM for auxiliary automobile," in *Conf. Rec. IEEE IAS Annu. Meeting*, vol. 1, pp. 8-13, Oct. 2006.

[41]   J. Cross, and P. Viarouge, "Synthesis of high performance PM motors with concentrated windings," *IEEE Trans. Ene. Conv.,* vol. 17, no. 2, June 2002.

[42]   W. Ouyang, D. Zarko, and T. A. Lipo, "Permanent magnet machine design practice and optimization," in *Conf. Rec. IEEE IAS Annu. Meeting*, vol. 4, pp. 1905-1911, Oct. 2006.

[43]   S. E. Sibandle, M. J. Kamper, R. Wang, and E. T. Rakgati, "Optimal design of a PM assisted rotor of a 110kW reluctance synchronous machine," *IEEE AFRICON*, vol. 2, pp. 793-797, Sept. 2004.

[44]   J. Baek, and P. S. Shin, "Shape optimization of a 400W AC servo motor using FEM with advanced evolution strategy," in *Conf. Rec. ISEM, IOS Press,* pp. 621-624, May 1998.

[45]   D. Zarko, "A systematic approach to optimized design of permanent magnet motors with reduced torque pulsations," Ph.D. Dissertation, University of Wisconsin-Madison, 2004.

[46]   H. Mok, S. K. Sul, and M. H. Park, "A load commutated inverter-fed induction motor drive system using a novel DC-side commutation circuit," *IEEE Trans. Ind. Appl.*, vol. 30, no. 3, pp. 736-745, May/June 1994.

[47]   Y. H. Chung, and G. H. Cho, " New current-source inverters with DC-side commutation and load-side energy recovery circuit," *IEEE Trans. Ind. Appl.*, vol. 27, no. 1, pp. 52-62, Jan./Feb. 1991.

[48]   B. Singh, K. B. Naik, and A. K. Goel, "Steady state of an inverter-fed induction motor employing natural commutation," *IEEE Trans. Power Elec.*, vol. 5, no. 1, pp.117-123, Jan. 1990.

[49]   H. A. Toliyat, N. Sultana, D. S. Shet, and J. C. Moreira, " Brushless permanent magnet (BMP) motor drive system using load-commutated inverter," *IEEE Trans. Power Elec.*, vol. 14, no. 5, pp. 831-837, Sep. 1999.

[50]   H. L. Hess, and D. M. Divan, "Extending the low frequency operation of load commutated inverters with torque control technique," in *Conf. Rec. IEEE IAS Annu. Meeting*, vol. 1, pp. 607-614, 1992.

[51]   S. Martinez, and F. Aldana, "Current-source double DC-side forced commutation inverter," *IEEE Trans. on Ind. Appl.*, vol. 14, no. 6, pp. 448-452, Nov./Dec. 1978.

[52]   G. H. Cho, and S. S. Park, "A new current source inverter with simultaneous recovery and commutation," *IEEE Trans. Ind. Appl.*, vol. 25, no. 1, pp. 162-171, Jan./Feb. 1989.

[53]   S. Kwak, "Design and analysis of modern three-phase AC/AC power converters for AC drives and utility interface," Ph.D. Dissertation, Texas A&M University, 2005.

[54]   D. Seyoum, and C. Grantham, "Terminal voltage control of a wind turbine driven isolated induction generator using stator oriented field control," in *Conf. Rec. IEEE APEC*, vol. 2, pp.846-852, Feb. 2003.

[55]   M. Malinowski, W. Kolomyjski, M.P. Kazmierkowski, and S. Stynski "Control of variable-speed type wind turbines using direct power control space vector modulated 3-level PWM converter," in *Conf. Rec. Ind. Tech. ICIT*, pp. 1516-1521, Dec. 2006.

[56]   J. Zhang, F. Rahman, and C. Grantham "A new scheme to direct torque control of interior permanent magnet synchronous machine drives for constant inverter switching and low torque ripple," in *Conf. Rec. PEMC*, vol. 3, pp. 1-5, Aug. 2006.

[57]   M. Malinowski, M. Jasinski, and M. P. Kazmierkowski, "Simple direct power control of three-phase PWM rectifier using space-vector modulation (DPC-SVM)," *IEEE Trans. Ind. Elec.*, vol. 51, no. 2, pp. 447-454, Apr. 1991.

[58]   J. Zhang, M. F. Rahman, and C. Grantham, "A new scheme to direct torque control of interior permanent magnet synchronous machine drives for constant inverter switching frequency and low torque ripple," in *Conf. Rec. CES/IEEE IPEMC*, vol. 3, pp. 1-5, Aug. 2006.

[59]   M. Malinowski, M. P. Kazmierkowski, and A. M. Trzynadlowski, "A comparative study of control techniques for PWM rectifiers in AC adjustable

speed drives," *IEEE Trans. Power Elec.*, vol. 18, no. 6, pp. 1390-1396, Nov. 2003.

[60] P. Niazi, H. A. Toliyat, and A. Goodarzi, "Robust maximum torque per amp (MTPA) control of PM assisted SynRM for tractions application," *IEEE Trans Power Elec.*, vol. 56, no. 4, pp. 1538-1545, July 2007.

[61] S. Morimoto, Y. Takeda, T. Hirasa, and K. Taniguchi, "Expansion of operating limit for permanent magnet motor by current vector control considering inverter capacity," *IEEE Trans. Ind. Appl.*, vol. 26, no. 5, pp. 866-871, Sep./Oct. 1990.

[62] S. Morimoto, H. Kato, M. Sanada, and Y. Takeda "Output maximization control for wind generation system with interior permanent magnet synchronous generator," in *Conf. Rec. IEEE IAS Annu. Meeting*, vol. 1, pp. 503-510, Oct. 2006.

APPENDIX A

VOLTAGE BASED DIRECT POWER CONTROL FOR THE CURRENT-FED DRIVE

PERFORMANCE DATA [rms]:

Rating [W] =	-3300	Speed [RPM] =	3600
Armature Cur Den =	6.15913e+006	Current =	15.1515
Id =	-13.6153	Iq =	-6.64782
Vd =	65.2763	Vq =	31.7768
Terminal Voltage =	72.6	Field Voltage =	85.3803
B RMS Air Gap =	0.387677	B RMS Teeth =	0.623455
B RMS Back Iron =	0.895591	B RMS Rotor =	0.645464
Core Loss =	27.6225	Armature Loss =	60.2704
Total Loss =	91.0991	Harmonic Loss =	3.20619
S.C. Current =	-21.921	Coercive Force =	1.19976
Shear [psi] =	1.13816	delta [deg] =	64.043
psi [deg] =	-180.067	gamma [deg] =	-116.025
Efficiency =	0.973136	Power Factor =	-0.999999

STATOR SPECS:

Slots/pole/phase(ma) =	0.5	Pole Pairs(p) =	4
Phases =	3	lots(ns) =	12
N_Coil_Slot	2	nc/npar =	24
Series Turns(na) =	96	# Slots Shorted =	0
Tooth Width =	0.0171067	Opening Width =	0.0063586
Slot Bottom Width =	0.0282696	Slot Top Width =	0.0134499
Opening Height =	0.001	Slot Depression =	0.0031793
Base Current =	12.3001	ia =	0.615913
Ia =	15.1515	length of series wire =	19.1601
area of wires =	2.46001e-006	Resistance of wire =	0.175025
Slot Height =	0.0283034	Back Iron Depth =	0.00833775
raths =	2.10435	lams =	0.440165
lamus =	0.220082		

ROTOR SPECS:

Rotor A.G. Radius =	0.0544795	Air Gap =	0.0007
Bridge Width =	0.001	Inner Radius =	0.0359044
Sm. Magnet Depth =	0.0032587	Lg. Magnet Depth =	0.0037477
Sm Mag Span [deg] =	12.8917	Lg Mag Span [deg] =	33.2464
Rotor Core Depth 1 =	3.41093	Rotor Core Depth 2 =	4.57878
Rotor Core Depth 3 =	3.57905	L_Magnet Span Length =	6.04192

INDUCTANCES [Henries]:

d-Axis =	0.00258248	q-Axis =	0.0066514
d-Magnetizing =	0.00170845	q-Magnetizing =	0.00594499
d-Thru Over q-Mag =	0.223779	d-Thru =	0.00133036

d-Circ Over q-Mag =	0.0635979	d-Circ. =	0.000378089
End Turn Leakage =	7.43597e-005	Slot Leakage =	0.000440542
5th Belt Leakage =	0.000237799	7th Belt Leakage =	0.000121326
Forward Zig-Zag =	0	Backward Zig-Zag =	0

FIELD SPECS:

Magnet Remanence =	1.2	Fund Field =	0.498537
Air-Gap Field 1 =	0	Air-Gap Field 2 =	0.729376
Max Core Density =	0.895591	PM Flux Linkage =	0.0566195

MACHINE SPECS:

Diameter =	0.19	Length of series wire =	19.1601
Active Length =	0.06142	Iron Mass =	7.14666
Saliency Ratio =	2.57559	Active Rotor Vol. =	0.000572699
Copper Mass =	1.26696	Magnet Mass =	0.535102
Total Mass =	8.94872	Reflected Moment =	0.00513873
Max RMS Ph. Curr. =	15.1515	Converter Cost =	428.347
Machine Cost =	78.3327	Total Cost =	506.68

APPENDIX B

DSP PROGRAM OF THE DIRECT POWER CONTROL FOR THE CURRENT-FED DRIVE SYSTEM

```
// Include header files used in the main function
#include "target.h"
#include "DSP281x_Device.h"
#include "IQmathLib.h"
#include "FCM.h"
#include "parameter.h"
#include "build.h"
#include <math.h>

#define ADC_usDELAY2 20L
#define CPU_CLOCK_SPEED     6.6667L   // for a 150MHz CPU clock speed
#define ADC_usDELAY 5000L
#define DELAY_US(A)  DSP28x_usDelay(((((long double) A * 1000.0L) / (long
double)CPU_CLOCK_SPEED) - 9.0L) / 5.0L)
#define BOUND_THETA(x,y)  ( ( x >= y ) ? ( x-y ) : ( x < 0 ) ? ( x + y ) : ( x ) )

#define sqrt8_by_PI             0.900316

extern void DSP28x_usDelay(unsigned long Count);
interrupt void MainISR(void);
interrupt void ADC_Offset(void);
interrupt void QepISR(void);

// Global variables used in this system
// BASE_FREQ = 240Hz, Refer to parameter.h
float32 SpeedRef = 0.20;          // Speed reference (pu)
float32 SpeedRef_Rect = 1.0;            // Speed reference for Rectifier (pu), 1,0 means 240Hz
float32 SpeedRef_Inveter = 0.25;        // Speed reference for Inverter (pu), 0.25 means 60Hz
float32 alpha=0.143;                    // Delay angle for Rec., 0.5 = 180 [deg]
float32 beta=0.0;                       // Delay angle for Inv.  1.0 = 360 [deg]
long IQ_alpha=0, IQ_beta=0;
Uint16 U_High,V_High, W_High, U_Low, V_Low, W_Low;

float32 T = 0.001/ISR_FREQUENCY;   // Samping period (sec), see parameter.h
Uint32 VirtualTimer = 0;
Uint16 ILoopFlag = FALSE;
Uint16 SpeedLoopFlag = FALSE;
int16 DFuncDesired = 0x1A00;      // Desired duty cycle (Q15)
_iq CurrentSet = _IQ(0.0031);
Uint16 IsrTicker = 0;
Uint16 BackTicker = 0;
unsigned SW_ON, SW_OFF, sector=0,sector_conv=0,ZC_Enable=0;
```

```
long dummy=0,rg2Out_old=0;
long Deg_0, Deg_30, Deg_60, Deg_120, Deg_180, Deg_240, Deg_300, Deg_360;
long var1=0, var2=0, var3=0, var4=0, var5=0, var6=0;
int16 DlogCh1 = 0;
int16 DlogCh2 = 0;
int16 DlogCh3 = 0;
int16 DlogCh4 = 0;
volatile Uint16 EnableFlag = FALSE;

// clarke instantiation
CLARKE clarke1_fdb = CLARKE_DEFAULTS;
PARK park1_fdb = PARK_DEFAULTS;
IPARK ipark1 = IPARK_DEFAULTS;
// Instance PID regulator to regulate the DC-bus current and speed
PIDREG3 pid1_idc = PIDREG3_DEFAULTS;
PIDREG3 pid1_spd = PIDREG3_DEFAULTS;
PIDREG3 pid1_vdc = PIDREG3_DEFAULTS;

// Instance a PWM driver instance
PWMGEN pwm1 = PWMGEN_DEFAULTS;

// Create an instance of the ADC driver
ILEG2DCBUSMEAS ilg2_vac1 = ILEG2DCBUSMEAS_DEFAULTS;

// Create an Zero Cross Trigger driver for Motor Back emf.
ZCT zc1 = ZCT_DEFAULTS;

// Instance a ramp controller to smoothly ramp the frequency
RMPCNTL rc1 = RMPCNTL_DEFAULTS;

// Instance a ramp generator to simulate an Anglele
RAMPGEN rg1 = RAMPGEN_DEFAULTS;

// Instance a ramp controller to smoothly ramp the frequency
RMPCNTL rc2 = RMPCNTL_DEFAULTS;

// Instance a ramp generator to simulate an Anglele
RAMPGEN rg2 = RAMPGEN_DEFAULTS;

// Instance a RAMP2 Module
RMP2 rmp2 = RMP2_DEFAULTS;

// Instance a MOD6 Module
MOD6CNT mod1 = MOD6CNT_DEFAULTS;

// Instance a SPEED_PR Module
//SPEED_MEAS_CAP speed1 = SPEED_MEAS_CAP_DEFAULTS;
```

```c
// Instance a QEP interface driver
QEP qep1 = QEP_DEFAULTS;
// Instance a speed calculator based on QEP
SPEED_MEAS_QEP speed1 = SPEED_MEAS_QEP_DEFAULTS;

// Create an instance of DATALOG Module
DLOG_4CH dlog = DLOG_4CH_DEFAULTS;
Uint16 AdcInt = 0;
Uint16 trigReset = 1;
_iq TRIG_POINT = _IQ(0.0);
_iq IQ_alpha_offset = _IQ(0.1);

// MPC parameters
_iq E_pm_Xq = _IQ(0.997);            // (72.4 / 72.6) * 1
_iq E_pm_Xq_sqr = _IQ(0.994);
_iq Xq_Xd = _IQ(2.342);                      // (1 - (3.014/7.27)) * 4
_iq Xq_Xd_sqr = _IQ(2.742);      // (Xq - Xd)^2 * 8
_iq _G = _IQ(1);

// Vd, Vq
float32 VdcRef = 0.866;
_iq VdRef, VqRef, IdRef, IqRef, Idfdb, Iqfdb, Vs, mpv_angle, Idc_cmd;

// alpha gain
_iq GainAlfa = _IQ(0.0275);

// average varaiables
_iq vd_avg[5] = {0,0,0,0,0};
_iq vq_avg[5] = {0,0,0,0,0};
_iq vdc_avg[5] = {0,0,0,0,0};
_iq vac_avg[5] = {0,0,0,0,0};
_iq VdcOffset = _IQ(0.0);
_iq test_beta;

// single phase inverter variables
_iq dcVolt, loadVolt, TotalLoad, ActiveLoad, ReactiveLoad = _IQ(0.5);
Uint16 dc_sample = 25;
Uint2 dpcDelayTimer = 0;
Uint32 DPC_DELAY_TIME = 400000;
void main(void)
{
        InitSysCtrl();

    EALLOW;
    SysCtrlRegs.HISPCP.all = 0x0000;
    EDIS;
        DINT;
        IER = 0x0000;
```

```
        IFR = 0x0000;
        InitPieCtrl();
        InitPieVectTable();

/*   EvaRegs.GPTCONA.all = 0;
  EvaRegs.T2PR = SYSTEM_FREQUENCY*1000000*T;
  EvaRegs.T2CNT = 0x0000;
  EvaRegs.T2CMPR = 0x0000;
  while (EnableFlag==FALSE)
  {
   BackTicker++;
  }
EvaRegs.EVAIMRB.bit.T2PINT = 1;
  EvaRegs.EVAIFRB.bit.T2PINT = 1;
  EvaRegs.T2CON.all = 0x9040;
        EALLOW;
        PieVectTable.T2PINT = &ADC_Offset;
        EDIS;
*/
EvaRegs.GPTCONA.all = 0;
  EvaRegs.T1PR = SYSTEM_FREQUENCY*1000000*T;
  EvaRegs.T1CNT = 0x0000;
  EvaRegs.T1CMPR = 0x0000;
  while (EnableFlag==FALSE)
  {
   BackTicker++;
  }
  EvaRegs.EVAIMRA.bit.T1PINT = 1;
  EvaRegs.EVAIFRA.bit.T1PINT = 1;
  EvaRegs.T1CON.all = 0x9040;
        EALLOW;
        PieVectTable.T1PINT = &ADC_Offset;
        PieVectTable.CAPINT3 = &QepISR;
        EDIS;
  PieCtrlRegs.PIEIER2.all = M_INT4;
  PieCtrlRegs.PIEIER3.all = M_INT7;
        //IER |= M_INT3;
        IER |= (M_INT2 | M_INT3);

// Initialize RAMPGEN module
  rg1.StepAngleMax = _IQ(BASE_FREQ*T);

// Initialize RAMPGEN module
  rg2.StepAngleMax = _IQ(BASE_FREQ*T);

// Initialize PWM module
  pwm1.PeriodMax = (SYSTEM_FREQUENCY/PWM_FREQUENCY)*1000;  // Asymmetric
PWM
```

```
   pwm1.DutyFunc = DFuncDesired;                    // DutyFunc = Q15
   pwm1.init(&pwm1);
// Initialize DATALOG module
   dlog.iptr1 = &DlogCh1;
   dlog.iptr2 = &DlogCh2;
   dlog.iptr3 = &DlogCh3;
   dlog.iptr4 = &DlogCh4;
   dlog.trig_value = 0x01;
   dlog.size = 0x400;
   dlog.prescalar = 1;
   dlog.init(&dlog);

// Initialize ADC module
   ilg2_vac1.init(&ilg2_vac1);

/* Initialize the SPEED_PR module (150 MHz, N = 1 event period/rev)
        speed1.InputSelect = 0;
        speed1.BaseRpm = 120*(BASE_FREQ/P);
        speed1.SpeedScaler = (Uint32)(ISR_FREQUENCY/(1*BASE_FREQ*0.001));
*/

// Initialize QEP module
   qep1.LineEncoder = 1024; //1000;
   qep1.MechScaler = _IQ30(0.25/qep1.LineEncoder);
   qep1.PolePairs = 4; //P/2;

//   qep1.CalibratedAngle = -2365;
        qep1.CalibratedAngle = -1250;
   qep1.init(&qep1);

// Initialize the Speed module for QEP based speed calculation
   speed1.K1 = _IQ21(1/(BASE_FREQ*T));
   speed1.K2 = _IQ(1/(1+T*2*PI*30));  // Low-pass cut-off frequency
   speed1.K3 = _IQ(1)-speed1.K2;
   speed1.BaseRpm = 120*(BASE_FREQ/P);

// Initialize RMPCNTL module for Rectifier
   rc1.RampDelayMax = 0.1;
   rc1.RampLowLimit = _IQ(0);
   rc1.RampHighLimit = _IQ(1);

// Initialize RMPCNTL module for Inverter
   rc2.RampDelayMax = 2;
   rc2.RampLowLimit = _IQ(0);
   rc2.RampHighLimit = _IQ(1);

// Initialize the PID_REG3 module for dc-bus current
   pid1_idc.Kp = _IQ(1);
```

```
        pid1_idc.Ki = _IQ(T/0.003);
        pid1_idc.Kd = _IQ(0/T);
        pid1_idc.Kc = _IQ(0.2);
   pid1_idc.OutMax = _IQ(0.99);
   pid1_idc.OutMin = _IQ(0);

// Initialize the PID_REG3 module for speed
   pid1_spd.Kp = _IQ(1);
        pid1_spd.Ki = _IQ(T/0.1);
        pid1_spd.Kd = _IQ(0/T);
   pid1_spd.Kc = _IQ(0.2);
   pid1_spd.OutMax = _IQ(0.99);
   pid1_spd.OutMin = _IQ(0);

// Initialize the PID_REG3 module for VDC
        pid1_vdc.Kp = _IQ(1);
//      pid1_vdc.Ki = _IQ(0.001);
        pid1_vdc.Ki = _IQ(0.01);
        pid1_vdc.Kd = _IQ(0);
        pid1_vdc.Kc = _IQ(0.1);
        pid1_vdc.OutMax = _IQ(0.99);
        pid1_vdc.OutMin = _IQ(0);
   SW_OFF = 0, SW_ON = pwm1.PeriodMax;
        Deg_0 = _IQ(0);          // 1/12 = 0.083333333
        Deg_30 = _IQ(0.083333333);    // 1/12 = 0.083333333
        Deg_60 = _IQ(0.16666667);     // 1/6 = 0.1666666667
        Deg_120 = _IQ(0.33333333);    // 2/6 = 0.3333333333
        Deg_180 = _IQ(0.5);                 // 3/6 = 0.5
        Deg_240 = _IQ(0.66666666);    // 4/6 = 0.6666666666
        Deg_300 = _IQ(0.83333333);    // 5/6 = 0.8333333333
        Deg_360 = _IQ(1);                   // 6/6 = 1
        U_High = 0x0003;
        V_High = 0x0030;
        W_High = 0x0300;
        U_Low = 0x000C;
        V_Low = 0x00C0;
        W_Low = 0x0C00;
   EvaRegs.ACTRA.all=U_High+V_High+W_High;
        EINT;
        ERTM;
        for(;;) BackTicker++;

}
interrupt void ADC_Offset(void)
{
        int16 DatQ15;
   int32 Tmp;
        extern void DSP28x_usDelay(unsigned long Count);
```

```
        AdcRegs.ADCTRL2.all |= 0x2000;//Software trigger . Start SEQ1
        DELAY_US(ADC_usDELAY2);
        IsrTicker=IsrTicker+1;
        //Currents use PU unit and Q15 format.
        //Current limitation of BLDC motor used this experiment is 10Adc.
        //So, 1PU is 10A and If we change this into Q15 then it is 32767.

DatQ15 = AdcRegs.ADCRESULT0^0x8000;      // Convert raw result to Q15 (bipolar signal)
   Tmp = (int32)ilg2_vac1.ImeasAGain*(int32)DatQ15; // Tmp = gain*dat => Q28 = Q13*Q15
   ilg2_vac1.ImeasA = (int16)(Tmp>>13);             // Convert Q28 to Q15
   ilg2_vac1.ImeasA += ilg2_vac1.ImeasAOffset;      // Add offset
   ilg2_vac1.ImeasA *= -1;                           // Positive direction, current flows to
motor
   DatQ15 = AdcRegs.ADCRESULT1^0x8000;
   Tmp = (int32)ilg2_vac1.ImeasBGain*(int32)DatQ15;
   ilg2_vac1.ImeasB = (int16)(Tmp>>13);
   ilg2_vac1.ImeasB += ilg2_vac1.ImeasBOffset;
   ilg2_vac1.ImeasB *= -1;
   DatQ15 = AdcRegs.ADCRESULT2^0x8000;
   Tmp = (int32)ilg2_vac1.VaMeasGain*(int32)DatQ15;
   ilg2_vac1.VaMeas = (int16)(Tmp>>13);
   ilg2_vac1.VaMeas += ilg2_vac1.VaMeasOffset;

//   ilg2_vac1.VaMeas *= -1;
   DatQ15 = AdcRegs.ADCRESULT3^0x8000;
   Tmp = (int32)ilg2_vac1.VbMeasGain*(int32)DatQ15;
   ilg2_vac1.VbMeas = (int16)(Tmp>>13);
   ilg2_vac1.VbMeas += ilg2_vac1.VbMeasOffset;

//   ilg2_vac1.VbMeas *= -1;
   DatQ15 = AdcRegs.ADCRESULT4^0x8000;
   Tmp = (int32)ilg2_vac1.VcMeasGain*(int32)DatQ15;
   ilg2_vac1.VcMeas = (int16)(Tmp>>13);
   ilg2_vac1.VcMeas += ilg2_vac1.VcMeasOffset;

//   ilg2_vac1.VcMeas *= -1;
   DatQ15 = AdcRegs.ADCRESULT5^0x8000;
   Tmp = (int32)ilg2_vac1.VdcMeasGain*(int32)DatQ15;
   ilg2_vac1.VdcMeas = (int16)(Tmp>>13);
   ilg2_vac1.VdcMeas += ilg2_vac1.VdcMeasOffset;

//   AdcRegs.ADCTRL2.all |= 0x4040;

/*       DatQ15 = (AdcRegs.ADCRESULT5>>1)&0x7FFF;   // Convert raw result to Q15
(unipolar signal)
        Tmp = (int32)ilg2_vac1.VdcMeasGain*(int32)DatQ15; // Tmp = gain*dat => Q28 =
Q13*Q15
        if (Tmp > 0x0FFFFFFF)              // Limit Tmp to 1.0 in Q28
```

```
            Tmp = 0x0FFFFFFF;
            ilg2_vac1.VdcMeas = (int16)(Tmp>>13);         // Convert Q28 to Q15
            ilg2_vac1.VdcMeas += ilg2_vac1.VdcMeasOffset;       // Add offset
            ilg2_vac1.VdcMeas *= -1;
*/
            // reset the sequence
            AdcRegs.ADCTRL2.all |= 0x4040;
            if (IsrTicker>=7201){
                    var1 += ilg2_vac1.ImeasA;  //+-1.0 max, min
                    var2 += ilg2_vac1.ImeasB;      //Q15 format
                    var3 += ilg2_vac1.VaMeas;      //Q15 format
                    var4 += ilg2_vac1.VbMeas;      //Q15 format
                    var5 += ilg2_vac1.VcMeas;      //Q15 format
                    var6 += ilg2_vac1.VdcMeas;     //Q15 format
            }
      if(IsrTicker==8200){
          EALLOW;
          IsrTicker=0;
          ilg2_vac1.ImeasAOffset=(long)var1/(long)1000;
          ilg2_vac1.ImeasBOffset=(long)var2/(long)1000;
          ilg2_vac1.VaMeasOffset=(long)var3/(long)1000;
          ilg2_vac1.VbMeasOffset=(long)var4/(long)1000;
          ilg2_vac1.VcMeasOffset=(long)var5/(long)1000;
          ilg2_vac1.VdcMeasOffset=(long)var6/(long)1000;
                    //PieVectTable.T1UFINT = &EvaTimer1;
                    PieVectTable.T1PINT = &MainISR;
                    EDIS;
      }
            EvaRegs.EVAIMRA.bit.T1PINT = 1;
      EvaRegs.EVAIFRA.all = BIT7;
            PieCtrlRegs.PIEACK.all |= PIEACK_GROUP2;
}

// To check out system parameters such as ISR, sys_freq and so on
// Refer to parameter.h
interrupt void MainISR(void)
{
        _iq temp;

// Verifying the ISR
    IsrTicker++;
        if(AdcInt == 0)
                AdcInt = 1;
        else
                AdcInt = 0;

// -------------------------------------------------------------------------------
//    Call the Ramp control & generator calculation function for three-phase Rect.
```

```
//   SpeedRef_Rect=1 means 240Hz,  SpeedRef_Rect=0.5 means 60Hz
// -------------------------------------------------------------------------
/*   rc1.TargetValue = _IQ(SpeedRef_Rect);
   rc1.calc(&rc1);
   rg1.Freq = rc1.SetpointValue;//16777152;
   rg1.calc(&rg1);
*/


// -------------------------------------------------------------------------
//   Call the Ramp control & generator calculation function for single-phase Inv.
//   SpeedRef_Inverter=1 means 240Hz, SpeedRef_Inverter=0.25 means 60Hz
// -------------------------------------------------------------------------
   rc2.TargetValue = _IQ(SpeedRef_Inveter);// SpeedRef_Inveter=0.25, 60Hz/240Hz = 0.25
   rc2.calc(&rc2);
   rg2.Freq = rc2.SetpointValue;//_IQ(SpeedRef_Inveter);
        rg2.calc(&rg2);
/*        dummy=_IQabs(rg2.Out-rg2Out_old);
        if(dummy >= _IQ(0.9)) {
                IsrTicker=0;
        }*/


// -------------------------------------------------------------------------
//   Call the ILEG2_VAC read function.
// -------------------------------------------------------------------------
   ilg2_vac1.read(&ilg2_vac1);

// CLARKE module - Vabc -> Valpha, Vbeta
        clarke1_fdb.As = _IQ15toIQ((int32)ilg2_vac1.VaMeas);
        clarke1_fdb.Bs = _IQ15toIQ((int32)ilg2_vac1.VbMeas);
        clarke1_fdb.calc(&clarke1_fdb);

// PARK module - Valpha, Vbeta -> Vd, Vq
        park1_fdb.Alpha = clarke1_fdb.Alpha;
        park1_fdb.Beta = clarke1_fdb.Beta;
        park1_fdb.Angle = speed1.ElecTheta - _IQ(1);
        park1_fdb.Angle = -(park1_fdb.Angle);
        if(park1_fdb.Angle >= _IQ(1)) park1_fdb.Angle -= _IQ(1);

//        park1_fdb.Angle = rg1.Out;
        park1_fdb.calc(&park1_fdb);

// Average Vd & Vq
   vd_avg[0] = park1_fdb.Ds;
   park1_fdb.Ds = vd_avg[0]+vd_avg[1]+vd_avg[2]+vd_avg[3]+vd_avg[4];
   park1_fdb.Ds = _IQmpy(park1_fdb.Ds, _IQ(0.2));
   vd_avg[4] = vd_avg[3];
   vd_avg[3] = vd_avg[2];
   vd_avg[2] = vd_avg[1];
```

```
    vd_avg[1] = vd_avg[0];
    vq_avg[0] = park1_fdb.Qs;
    park1_fdb.Qs = vq_avg[0]+vq_avg[1]+vq_avg[2]+vq_avg[3]+vq_avg[4];
    park1_fdb.Qs = _IQmpy(park1_fdb.Qs, _IQ(0.2));
    vq_avg[4] = vq_avg[3];
    vq_avg[3] = vq_avg[2];
    vq_avg[2] = vq_avg[1];
    vq_avg[1] = vq_avg[0];

// DC link regulation
        //pid1_vdc.Fdb = _IQ15toIQ((int32)ilg2_vac1.VdcMeas);
    // filter DC Link voltage

/*  if(dc_sample == 25)
    {
            pid1_vdc_raw = _IQ15toIQ((int32)ilg2_vac1.VdcMeas);
            dc_sample = 0;
    }
    else
            dc_sample++;
            vdc_avg[0] = pid1_vdc_raw;
            pid1_vdc.Fdb = vdc_avg[0]+vdc_avg[1]+vdc_avg[2]+vdc_avg[3]+vdc_avg[4];
            pid1_vdc.Fdb = _IQmpy(pid1_vdc.Fdb, _IQ(0.2));
            vdc_avg[4] = vdc_avg[3];
            vdc_avg[3] = vdc_avg[2];
            vdc_avg[2] = vdc_avg[1];
            vdc_avg[1] = vdc_avg[0];
*/
            pid1_vdc.Ref = _IQ(VdcRef);
            pid1_vdc.Fdb = _IQ15toIQ((int32)ilg2_vac1.VdcMeas) - VdcOffset;
            pid1_vdc.calc(&pid1_vdc);
            Vs = pid1_vdc.Out;

//          Vs = _IQ(0.5);
//          pid1_vdc.Out; convert to Va* and delta!
// MPC -> angle
            temp = _IQmpy(Vs, Vs);
            temp = _IQmpy(temp, Xq_Xd_sqr);
      temp =  temp + E_pm_Xq_sqr;
            temp = _IQsqrt(temp);
            temp = E_pm_Xq - temp;
            mpv_angle = _IQmpy(Vs, Xq_Xd);
            mpv_angle = _IQdiv(temp, mpv_angle);
            //mpv_angle = _IQdiv(_IQ(1), _IQcos(mpv_angle));

// Vd & Vq Cmd >>> Vq = Va* cos(delta) >>> Vd = Va* sin(delta)
            VqRef = _IQmpy(Vs, mpv_angle);
            temp  = _IQmpy(Vs, Vs) - _IQmpy(VqRef, VqRef);
```

```
        VdRef = _IQsqrt(temp);
        IdRef = _IQmpy(VdRef, _G);
        IqRef = _IQmpy(VqRef, _G);

// Iq = -vd/(we Lq) >>> Id = (-vq+E)/weLd //
        Iqfdb = -park1_fdb.Ds;
        Idfdb = _IQdiv((_IQ(0.997245) + park1_fdb.Qs), _IQ(0.41458));
        ipark1.Ds = IdRef + Idfdb;
        ipark1.Qs  = IqRef + Iqfdb;
//        ipark1.Angle = park1_fdb.Angle;
//        ipark1.calc(&ipark1);
        ipark1.Ds = _IQmpy(ipark1.Ds, ipark1.Ds);
        ipark1.Qs = _IQmpy(ipark1.Qs, ipark1.Qs);
        Idc_cmd = _IQsqrt(ipark1.Ds+ipark1.Qs);
        Idc_cmd = _IQmpy(Idc_cmd, GainAlfa);


// -------------------------------------------------------------------------------
        /*if((speed1.ElecTheta >= _IQ(0.001)) && (trigReset == 1))
        {
                zc1.ZeroCrossTrig = 0x0007FFF;
                trigReset = 0;
        }
        else
        {       zc1.ZeroCrossTrig = 0x0;
                if(speed1.ElecTheta < _IQ(0.001))trigReset = 1;
        }*/

// -------------------------------------------------------------------------------
//   Call the Zero Crossing Trigger read function for Motor Back-EMF
// -------------------------------------------------------------------------------
//        zc1.IN_A=ilg2_vac1.VabMeas;
        zc1.IN_A = _IQ15toIQ((int32)ilg2_vac1.VaMeas);
        if(ZC_Enable ==1){
//                zc1.calc(&zc1); // Start Zero crossing
                //rg1.calc(&rg1); // Start theta calculation for Converter

                // -------------------------------------------------------------------------------
                //   Call the QEP calculation function
                // -------------------------------------------------------------------------------
                        qep1.calc(&qep1);
                // -------------------------------------------------------------------------------
                //   Connect inputs of the SPEED_FR module and call the speed calculation function
                // -------------------------------------------------------------------------------
                        speed1.ElecTheta = _IQ15toIQ((int32)qep1.ElecTheta);
                        speed1.DirectionQep = (int32)(qep1.DirectionQep);
                        speed1.calc(&speed1);
                        //rg1.Out = speed1.ElecTheta;
                        rg1.Out = park1_fdb.Angle;
```

```
                                rg1.Out = rg1.Out + TRIG_POINT;
                                if(rg1.Out >= _IQ(1)) rg1.Out -= _IQ(1);
                                if(rg1.Out < _IQ(0.1))zc1.ZeroCrossTrig = 0x0007FFF;
                                else zc1.ZeroCrossTrig = 0x0;
                    }
            else {
                    rg1.Out = 0;
                    rg1.Angle=0;
                    }
            /*if(zc1.ZeroCrossTrig == 0x0007FFF){
                    rg2.Out = Deg_30;
                    rg2.Angle = Deg_30;
                    zc1.ZeroCros_Count++;
                    }*/

// single phase voltage control
            dcVolt = pid1_vdc.Fdb;
            temp = _IQ15toIQ((int32)ilg2_vac1.VcMeas);
            if(temp > _IQ(0))
            {
               vac_avg[0]  = temp;
                    loadVolt = vac_avg[0]+vac_avg[1]+vac_avg[2]+vac_avg[3]+vac_avg[4];
                    loadVolt = _IQmpy(loadVolt, _IQ(0.2));
                    vac_avg[4] = vac_avg[3];
                    vac_avg[3] = vac_avg[2];
                    vac_avg[2] = vac_avg[1];
                    vac_avg[1] = vac_avg[0];
            }
            temp = _IQdiv(loadVolt, dcVolt);
            TotalLoad = _IQmpy(temp, _IQsqrt(8));//_IQ(sqrt8_by_PI));
            TotalLoad = _IQmpy(temp, ReactiveLoad);
            // Real Load Component
            ActiveLoad = _IQmpy(TotalLoad, TotalLoad);
            ActiveLoad -= _IQmpy(ReactiveLoad, ReactiveLoad);
            ActiveLoad = _IQsqrt(ActiveLoad);
            // Load Current Calculation
//          temp = _IQmpy(temp, loadVolt);
//          temp = _IQmpy(temp, _IQ(sqrt8_by_PI));
//          iL_cmd = _IQdiv(temp, ActiveLoad);


// ----------------------------------------------------------------------------------------------------
//   Determine Sector depending on theta_generation(rg2.Out)
//   beta is the delay angle for single phase Inverter,
//   beta cannot be over  _IQ(0.5), which is 180 [deg].
//   Now, SpeedRef_Inverter=0.25 means 60Hz, beta=0.0
//   For Inverter.
// ----------------------------------------------------------------------------------------------------
```

```
        test_beta = _IQatan2PU(ActiveLoad, ReactiveLoad);
        IQ_beta = _IQ(beta);
//      IQ_beta = _IQmpy(test_beta, _IQ(0.1));
        if(IQ_beta >= Deg_360) IQ_beta=Deg_360;
        var3= BOUND_THETA(rg2.Out-IQ_beta,Deg_360);

/*      if(var3 < Deg_180 && rg2.Out < Deg_180)                    sector=1;          //
0+beta <= theta < 180
        //else if(rg2.Out > Deg_360)              sector=0;                                  // theta > 360,
Unexpected value                  else if(var3 >= Deg_180 && rg2.Out >= Deg_180)
        sector=2;          // 180+beta <= theta <= 360
        //else    sector=0;
                                        // Unexpected value
*/
        if(Deg_0 <= rg2.Out && rg2.Out < Deg_180){
                if(Deg_0 <= var3 && var3 < Deg_180)  sector=1;
                }
        else if(Deg_180 <= rg2.Out && rg2.Out < Deg_360){
                if(Deg_180 <= var3 && var3 < Deg_360)          sector=2;
                }

// -----------------------------------------------------------------------------------------------------
//   Switching pattern generation for Single-phase Inverter using sector information
//        Rotation Direction ==> CCW,
//   Do not consider CW direction.
//   For Inverter.
// -----------------------------------------------------------------------------------------------------
        if(sector == 1)   {EvbRegs.ACTRB.all = U_High + V_Low;}     // Uph = High, Vph =
Low
        else if(sector == 2)        {EvbRegs.ACTRB.all = U_Low  + V_High;}    // Vph = High,
Uph = Low
        else               {EvbRegs.ACTRB.all = U_High + V_High;}     // Uph = High, Vph =
High


// -----------------------------------------------------------------------------------------------------
//   Switching pattern generation for Three-phase SCR Converter.
//        Alpha is the delay angle for Three-phase converter.
//   alpha cannot be over _IQ(1/6), which is 60[deg].
//   Eab is used for Zero Crossing signal
//   For SCR Converter
// -----------------------------------------------------------------------------------------------------
        if(dpcDelayTimer >= DPC_DELAY_TIME)      { IQ_alpha = Idc_cmd +
        IQ_alpha_offset;          }
        else{ IQ_alpha = _IQ(alpha); dpcDelayTimer++;}
        if(IQ_alpha >= Deg_60) IQ_alpha =  Deg_60;
        var4= BOUND_THETA(rg1.Out-IQ_alpha,Deg_360);
        if(Deg_0 <= rg1.Out && rg1.Out < Deg_60){
                if(Deg_0 <= var4 && var4 < Deg_60)    sector_conv=1;
```

```
                //else sector_conv=0;
                }
        else if(Deg_60 <= rg1.Out && rg1.Out < Deg_120){
                if(Deg_60 <= var4 && var4 < Deg_120)        sector_conv=2;
                //else sector_conv=0;
                }
        else if(Deg_120 <= rg1.Out && rg1.Out < Deg_180){
                if(Deg_120 <= var4 && var4 < Deg_180)       sector_conv=3;
                //else sector_conv=0;
                }
        else if(Deg_180 <= rg1.Out && rg1.Out < Deg_240){
                if(Deg_180 <= var4 && var4 < Deg_240)       sector_conv=4;
                //else sector_conv=0;
                }
        else if(Deg_240 <= rg1.Out && rg1.Out < Deg_300){
                if(Deg_240 <= var4 && var4 < Deg_300)       sector_conv=5;
                //else sector_conv=0;
                }
        else if(Deg_300 <= rg1.Out && rg1.Out < Deg_360){
                if(Deg_300 <= var4 && var4 < Deg_360)       sector_conv=6;
                //else sector_conv=0;
                }
        else
        {sector_conv=0;}
        if (sector_conv == 1)    {EvaRegs.ACTRA.all = U_High + V_Low;}
        else if(sector_conv == 2)        {EvaRegs.ACTRA.all = U_High + W_Low;}
        else if(sector_conv == 3)        {EvaRegs.ACTRA.all = V_High + W_Low;}
        else if(sector_conv == 4)        {EvaRegs.ACTRA.all = V_High + U_Low;}
        else if(sector_conv == 5)        {EvaRegs.ACTRA.all = W_High + U_Low;}
        else if(sector_conv == 6)        {EvaRegs.ACTRA.all = W_High + V_Low;}
        else                     {EvaRegs.ACTRA.all = U_High + V_High +
W_High;}

/*
        if(sector_conv == 1)            {EvbRegs.CMPR5=SW_OFF;
        EvbRegs.CMPR6=SW_ON;} // W_High, V_Low
        else if(sector_conv == 2)       {EvbRegs.CMPR4=SW_ON;
        EvbRegs.CMPR5=SW_OFF;} // U_High, V_Low
        else if(sector_conv == 3)       {EvbRegs.CMPR4=SW_ON;
        EvbRegs.CMPR6=SW_OFF;} // U_High, W_Low
        else if(sector_conv == 4)       {EvbRegs.CMPR5=SW_ON;
        EvbRegs.CMPR6=SW_OFF;} // V_High, W_Low
        else if(sector_conv == 5)       {EvbRegs.CMPR4=SW_OFF;
        EvbRegs.CMPR5=SW_ON;} // V_High, U_Low
        else if(sector_conv == 6)       {EvbRegs.CMPR4=SW_OFF;
        EvbRegs.CMPR6=SW_ON;} // W_High, U_Low          else
        {EvbRegs.CMPR4=SW_ON;    EvbRegs.CMPR5=SW_ON;
        EvbRegs.CMPR6=SW_ON;}
```

```
*/

// --------------------------------------------------------------------------------------------------
//    Connect inputs of the DATALOG module
// --------------------------------------------------------------------------------------------------

   DlogCh1 = (int16)ilg2_vac1.VaMeas;
   //DlogCh2 = (int16)zc1.ZeroCrossTrig;
        DlogCh2 = (int16)ilg2_vac1.VbMeas;
//        Vab_temp = _IQ15toIQ((int32)ilg2_vac1.VabMeas);

   //DlogCh3 = (int16)_IQtoIQ15(zc1.IN_A);
        //DlogCh3 = (int16)zc1.ZeroCrossTrig;
   //DlogCh4 = (int16)_IQtoIQ15(park1_fdb.Angle);
//        DlogCh3 = (int16)_IQtoIQ15(loadVolt);
//        DlogCh4 = (int16)_IQtoIQ15(var4);
        //DlogCh4 = (int16)ilg2_vac1.VdcMeas;
   //DlogCh3 = (int16)_IQtoIQ15(Idfdb);
        //DlogCh4 = (int16)_IQtoIQ15(Iqfdb);
   //DlogCh3 = (int16)_IQtoIQ15(rg1.Out);// rg1.Out is theta for Converter
//   DlogCh4 = (int16)_IQtoIQ15(dcVolt);// rg2.Out is theta for Inverter
        DlogCh3 = (int16)_IQtoIQ15(rg1.Out);
        DlogCh4 = (int16)_IQtoIQ15(var4);

// ------------------------------------------------------------------------------
//    Increase virtual timer and force 15 bit wrap around
// ------------------------------------------------------------------------------
        VirtualTimer++;
        VirtualTimer &= 0x00007FFF;
//        rg2Out_old = rg2.Out;
// ------------------------------------------------------------------------------
//    Call the DATALOG update function.
// ------------------------------------------------------------------------------
   dlog.update(&dlog);
        EvaRegs.EVAIMRA.bit.T1PINT = 1;
   EvaRegs.EVAIFRA.all = BIT7;
        PieCtrlRegs.PIEACK.all |= PIEACK_GROUP2;
}
interrupt void QepISR(void)
{

// ------------------------------------------------------------------------------
//    Call the QEP_DRV isr function.
// ------------------------------------------------------------------------------
   qep1.isr(&qep1);
// Enable more interrupts from this timer
        EvaRegs.EVAIMRC.bit.CAP3INT = 1;
        // Note: To be safe, use a mask value to write to the entire
```

```
            // EVAIFRC register.  Writing to one bit will cause a read-modify-write
            // operation that may have the result of writing 1's to clear
            // bits other then those intended.
       EvaRegs.EVAIFRC.all = BIT2;
            // Acknowledge interrupt to recieve more interrupts from PIE group 3
            PieCtrlRegs.PIEACK.all |= PIEACK_GROUP3;
}
// ----------------------------------------------------------------------------
// No more.
// ----------------------------------------------------------------------------
```

VITA

Jeihoon Baek received a B.S. degree in 1996 and an M.S. degree in 1998, both in electrical engineering from Hongik University, Korea. In 2006, he received an M.S. degree from the University of Wisconsin-Madison. From 2006 to 2009, he was with the Advanced Electric Machines and Power Electronics Laboratory, Texas A&M University, as a research assistant. His research interests include electric machine design, power converters for adjustable speed drives, and DSP-based power electronics applications. He can be reached through Dr. Hamid A. Toliyat, Department of Electrical and Computer Engineering, Texas A&M University, College Station, Texas 77843-3128.